

Interface Defects and Advanced Engineering of Silicon Heterojunction Solar Cells

Vasudevan, Ravi

DOI

[10.4233/uuid:a8fd4a11-f0b1-4373-817f-f07a27235bde](https://doi.org/10.4233/uuid:a8fd4a11-f0b1-4373-817f-f07a27235bde)

Publication date

2016

Document Version

Final published version

Citation (APA)

Vasudevan, R. (2016). *Interface Defects and Advanced Engineering of Silicon Heterojunction Solar Cells*. [Dissertation (TU Delft), Delft University of Technology]. <https://doi.org/10.4233/uuid:a8fd4a11-f0b1-4373-817f-f07a27235bde>

Important note

To cite this publication, please use the final published version (if applicable).
Please check the document version above.

Copyright

Other than for strictly personal use, it is not permitted to download, forward or distribute the text or part of it, without the consent of the author(s) and/or copyright holder(s), unless the work is under an open content license such as Creative Commons.

Takedown policy

Please contact us and provide details if you believe this document breaches copyrights.
We will remove access to the work immediately and investigate your claim.

Interface Defects and Advanced Engineering of Silicon Heterojunction Solar Cells

RAVI VASUDEVAN

Interface Defects and Advanced Engineering of Silicon Heterojunction Solar Cells

Proefschrift

ter verkrijging van de graad van doctor aan de
Technische Universiteit Delft, op gezag van de
Rector Magnificus prof. ir. K. C. A. M. Luyben,
voorzitter van het College voor Promoties,
in het openbaar te verdedigen op
23 September 2016 om 10:00 uur

door

Ravi VASUDEVAN

Master of Science, Delft University of Technology
geboren te Worcester, Massachusetts, The United States of America

This dissertation has been approved by the promotors:

Prof. dr. M. Zeman

Prof. dr. A. H. M. Smets

Composition of the doctoral committee:

Rector Magnificus

chairperson

Prof. dr. M. Zeman

Technische Universiteit Delft

Prof. dr. A. H. M. Smets

Technische Universiteit Delft

Independent members:

Dr. S. De Wolf

École Polytechnique Fédérale de Lausanne

Dr. T. Matsui

National Institute of Advanced Industrial

Science and Technology

Dr. D. Muñoz

National Institute for Solar Energy

Prof. dr. R. E. I. Schropp

Technische Universiteit Eindhoven

Prof. dr. A. W. Weeber

Technische Universiteit Delft and ECN

Reserve Member:

Prof. dr. P. Palensky

Technische Universiteit Delft

This work was carried out within the FLASH project of STW.

Typset using L^AT_EX. Template by Dr. Klaus Jäger.

Dutch summary and proposition translation by Dr. Rudi Santbergen.

Cover design by Ingeborg Kuijlaars.

Printed by CPI-Koninklijke Wöhrmann - Zutphen.

ISBN: 978-94-6328-086-0

Copyright © 2016 R. Vasudevan

All rights reserved. No part of this publication may be reproduced, stored in a retrieval system, or transmitted in any form or by any means without the prior written permission of the copyright owner.

A digital copy of this thesis is available at <http://repository.tudelft.nl>

Contents

1	Introduction	1
1.1	Solar Energy and Photovoltaics	1
1.2	Silicon Based Solar Cells	4
1.3	Defects in Silicon	5
1.4	Novel Application of SHJ Solar Cells: Solar Based Water-Splitting .	11
1.5	Goals and Outline of Thesis	11
2	Methodology	13
2.1	Sample Preparation	13
2.2	Characterization	16
2.3	Optical Simulation	23
3	Temperature Effects on the a-Si:H/c-Si Interface Model using the Amphoteric Nature of Dangling Bonds	25
3.1	Introduction	26
3.2	Lifetime Models Used in This Work	26
3.3	Temperature Dependencies	29
3.4	Experimental Results	32
3.5	Conclusions	37
4	Light-Induced Effects on a-Si:H/c-Si Passivation	39
4.1	Introduction	40
4.2	Experimental Details	41
4.3	Results and Discussion	44
4.4	Conclusions	52
5	The Effect of Doped Layers on the Light-Induced Effects of a-Si:H/c-Si Passivation	55
5.1	Introduction	56
5.2	Experimental Details	57
5.3	Results and Discussion	58
5.4	Analysis	61
5.5	Conclusions	66

6	The Feasibility of FTPS on Crystalline Silicon Solar Cells	69
6.1	Introduction	70
6.2	Experimental Details	70
6.3	Evidence of Shallow Traps in Poly-Si Films	72
6.4	Interface Defects of SHJ Solar Cells	77
6.5	Conclusions	80
7	A Tandem nc-Si:H/Silicon Heterojunction Solar Cell Designed for Water Splitting	83
7.1	Introduction	84
7.2	Experimental Details	87
7.3	Results	88
7.4	Integration Simulation	95
7.5	Conclusions	96
8	Conclusions	97
8.1	What is the nature of the metastable properties of a-Si:H passivation of c-Si?	97
8.2	Can FTPS be used to better understand the a-Si:H/c-Si interface?	99
8.3	How can novel applications of SHJ solar cells be best used to aid in water splitting applications?	100
8.4	Recommendations for Further Exploration	100
	Bibliography	103
	Acknowledgements	111
	Summary	115
	Samenvatting	117
	List of Publications	119
	Curriculum Vitae	123

1

Introduction

The Silicon Heterojunction (SHJ) solar cell is, at the time of this thesis publication, the world record holding photovoltaic (PV) technology based on silicon materials. The SHJ solar cells is based on a crystalline silicon (c-Si) absorber layer and uses hydrogenated amorphous silicon (a-Si:H) for surface passivation and charge carrier separation. This thesis specifically deals with the interface between c-Si and a-Si:H as this interface is of utmost importance in the conversion efficiency of SHJ solar cells. In this introduction, the fundamental principles behind the photovoltaic effect and the economic and technical aspects of PV today and in the future. This is followed by a more detailed discussion of silicon based solar cells and, specifically, SHJ solar cells. Then some sections giving the specific background pertaining to this thesis, specifically silicon defects and solar based water splitting are discussed. Finally, an outline of the rest of the chapters in this thesis is presented.

1.1 Solar Energy and Photovoltaics

The sun is the most abundant resource of energy on planet Earth. Through solar irradiation, the planet receives 174000 TWh of energy per year at its outer atmosphere. With some losses in the atmosphere, cloud cover and some other effects, the solar budget is estimated to be on average, 188 Wm^{-2} . [1] Over the entire land area of 149 million km^2 , this means that the land on the Earth receives an average of 2801 TW or 2.45×10^8 TWh per year. In 2012 the total energy production of humans for electricity was 2.27×10^4 TWh. [2] So it is clear to see that the

amount of energy that land receives per year severely dwarfs that of how much humans require even if significant growth is predicted. However, how that solar energy is converted into usable energy is very important.

Most of the energy used by humans is already produced by the sun. Fossil fuels, which are the primary sources of usable energy used by humans in 2016, come from the stored energy of life millions of years ago whether it be animal or plant. Animals typically obtain energy by consuming plants or other animals and plants obtain energy through photosynthesis, so fossil fuels are essentially a very inefficient way of converting solar energy into usable energy. Though this technique has worked for humanity throughout the industrial and into the information age, it is widely unsustainable in any sense of the word. Firstly, it is unsustainable because the resource is finite. Though estimates are shifting, there will surely come a time when these resources come to an end. Wind energy is also produced by the sun as temperature differences that cause the pressure differences in the air that eventually cause wind are solar based. Geothermal, hydroelectric and nuclear energies are some energy sources at the disposal of man that are not solar based, but these account for a very small percentage of the total energy production by humans.

Solar cells directly convert solar energy to electricity. The fundamental principles behind solar cells is the PV effect, which is presented in the following section followed by the current status of PV technology.

1.1.1 The Photovoltaic Effect

The photovoltaic effect, as its name implies, is a way to utilize light to generate a voltage. One can also describe it as converting the energy from photons of light into usable energy in the form of electricity. As electricity is the flow of electrons through a circuit, the main processes necessary are to excite electrons to a higher energy state and then send them through an external circuit. The resultant electrical energy can then be used directly or stored for later use. Before the electrons can be sent through an external circuit, three separate steps must happen in the solar cell:

1. The generation of electron-hole pairs
2. The separation of charge carriers
3. The collection of charge carriers

These steps are outlined in Figure 1.1. The generation of electron-hole pairs occurs when a photon of sufficient energy is absorbed by a semiconductor material and excites an electron from the valence band (represented as the energy level E_V in Figure 1.1a) where electrons are localized in bound states the conduction band (represented by the energy level E_C in Figure 1.1) where electrons are mobile and able flow through a material. This process leaves a positively charged “hole” in

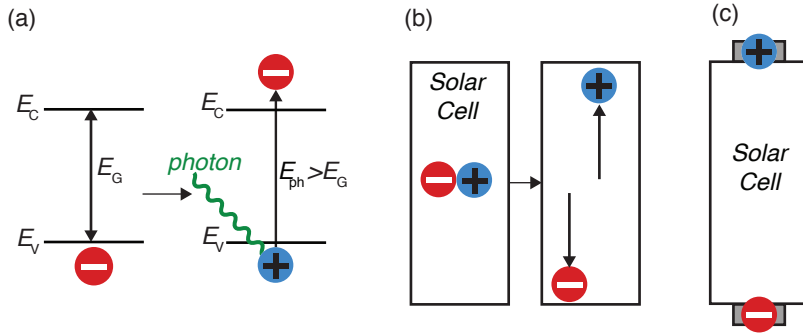


Figure 1.1: Illustration of the three steps of the photovoltaic effect. (a) Generation of electron hole pairs. Note that this is only a change of energy not a change of physical position as this is a band diagram. (b) Separation of charge carriers. The mechanism of separation can differ based on the technology, but the result is bringing holes in the valence band to one side of the solar cell and excited electrons to the other side. (c) Collection of charge carriers. In this step, carriers are collected at electrodes forming a potential between the two electrodes thus providing a voltage necessary to produce electricity when connected to an external circuit.

the valence band and the electron and hole form a so called electron-hole pair. Once this pair is generated, these two charge carriers must be separated. In the case of SHJ solar cells, one part of the solar cell favorably accepts electrons while rejecting holes and another part of the cell does the opposite. As charge carriers diffuse throughout the bulk material, eventually charge carriers move through these barriers and can be collected at electrodes. After these three steps, the electrons can flow through an external circuit generating electricity.

1.1.2 Current Status of Photovoltaics

In 2013, 139 TWh of electricity were generated with PV. This is up from 20 TWh in 2009. [3] It is predicted that 275 TWh of solar electricity will be generated in 2016. [4] This is still $< 1\%$ of total electricity generation. However, PV is becoming more viable as prices for PV system components drop as the technology becomes more mature. PV is projected to be 16% of power generation by 2050. [3]

There are a variety of PV technologies based on different absorber layer materials. These materials can range from so-called III-V materials, which produce very high efficiency solar cells to thin-film materials that can produce lower efficiency solar cells while keeping the cost of the solar cell lower. Though many different technologies have niche applications such as space, consumer products and small scale applications, the vast majority of power production using PV is done with solar cells using silicon based absorber layers. [5]

1.2 Silicon Based Solar Cells

Silicon is the basis for the vast majority of solar cells. Silicon has many favorable qualities as a solar cell material. Silicon is an abundant material on Earth and it has a bandgap which is close to ideal as a single junction absorber material for the solar spectrum. [6] Furthermore, silicon processing technology is very mature and have been massively scaled-up. Solar cells based on silicon materials have become the most favorable solar cell technology. Among all PV technologies, silicon based technologies had a market share of 94 % in 2014. [5]

Silicon PV can be broken down into different subcategories. Primarily, these are solar cells based on thin-film silicon absorber layers and wafer based silicon absorber layers. Thin-film silicon uses advanced thin-film processing techniques such as plasma enhanced chemical vapor deposition (PECVD) and sputtering. [7] This technology does show promise as a niche technology for applications that require flexible solar cells. In the past it seemed that thin-film silicon had promise to compete directly with c-Si. However, as of the writing of this thesis, it is struggling to compete on a commercial level with wafer based technologies and has a total marketshare of around 4 %. [5]

Silicon wafer based technologies start with producing high quality doped crystalline based silicon (c-Si). This can be done in a way that produces a monocrystalline wafer by using the so-called Czochralski (CZ) or Float Zone (FZ) methods. [8] These methods are expensive, but produce very high quality crystalline silicon with a single crystal orientation. FZ wafers are generally only used in research as FZ processing is cost prohibitive and even companies that produce the highest efficiency commercial solar cells use CZ wafers. [9, 10] Cheaper methods produce multicrystalline silicon wafers. Here, as the name implies, there is not a single crystal but multiple crystal grains. Multicrystalline silicon has grain boundaries which result in multiple crystal orientations and additional defects, particularly dislocations, which reduce the quality of the wafer for use as an absorber material in a solar cell. Multicrystalline silicon based solar cells have a marketshare of around 55.2 % while monocrystalline silicon based solar cells have a market share of around 35.5 %. [5] Though multicrystalline solar cells are less efficient than monocrystalline solar cells, their significantly lower production cost result in a lower levelized cost of electricity (LCOE). Though this is currently the case, monocrystalline silicon technologies are on the rise and the production of high quality monocrystalline wafers are decreasing and some predict that they will play a much bigger role in the future technological PV landscape. [11, 12] This thesis deals with a monocrystalline silicon technology.

Silicon wafer based solar cells can be further categorized into homojunction and heterojunction technologies. The difference between these two technologies has to do with the emitter (side of cell where minority charge carriers are collected) and back surface field (BSF) (side of cell where majority charge carriers are collected). In the case of homojunctions, emitters and BSFs of the solar cells have the same bandgap as the bulk absorber material. These are usually formed

using diffusion, implantation and alloying techniques. There are a large number of different technologies and methods to accomplish this. The emitter and BSF on a heterojunction solar cell, on the other hand, have a larger bandgap than the c-Si absorber material.

1.2.1 The Silicon Heterojunction Solar Cell

The technology dealt with in this thesis is known as the silicon heterojunction (SHJ) solar cell. This technology was pioneered by Sanyo (now Panasonic) who now holds the record for silicon based solar cells with an efficiency of 25.6 % under standard test conditions. The technology uses CZ or FZ based monocrystalline wafers. [10] Layers of thin-film silicon are deposited on the wafers to produce the emitter and BSF. This thin-film silicon is called hydrogenated amorphous silicon (a-Si:H) and is the same material that is the backbone for many thin-film silicon based technologies. a-Si:H has a bandgap of around 1.8 eV in contrast to the 1.1 eV bandgap of c-Si thus causing the heterojunction between the two materials. There were many stages in development of a-Si:H passivated cells from the first cell called the “Honeymoon” structure in 1983. [13]

The breakthrough needed to achieve high efficiencies using SHJ solar cells was the discovery that inserting a thin layer of intrinsic a-Si:H in between the wafer and the doped layers drastically improves surface passivation and allows for higher open circuit voltages (V_{OC}) and better current collection. [14] A schematic and band diagram of a typical SHJ solar cell are given in Figure 1.2. As this passivation quality of a-Si:H is of key importance to SHJ solar cell functionality, this thesis investigates the properties of this passivation. One key aspect of this passivation is reducing the defect density at the a-Si:H/c-Si interface.

1.3 Defects in Silicon

Defects are an important physical area of understanding for silicon-based solar cell technologies. Much of the work in this thesis seeks to better understand the complex nature of defects in SHJ solar cells. This section aims to inform the reader of what is meant by defects in the different contexts used in this thesis. Defects of both c-Si and a-Si:H are described and this is followed by a discussion of what is meant by metastability of these defects and how this influences SHJ solar cells.

1.3.1 c-Si Defects

c-Si has a long range structure and order that is meant to be a distinct crystal lattice. Defects, in terms of c-Si, typically refer to a break in this structure. There are various categories of defects, which can include

1. Foreign interstitial defects - impurities such as oxygen or metals

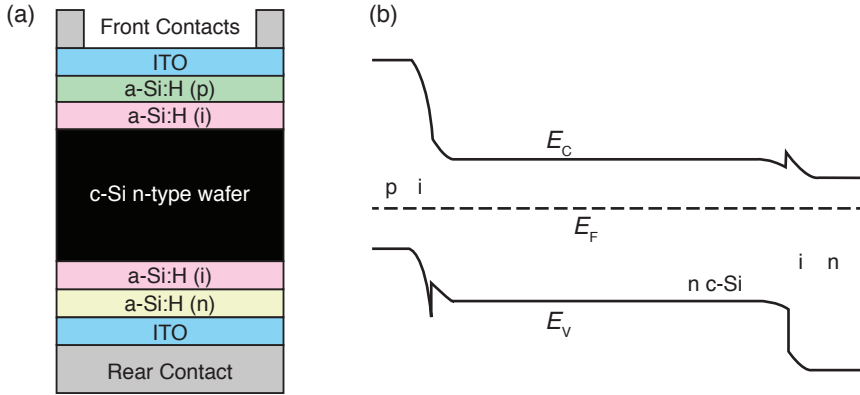


Figure 1.2: Schematic and band diagram of a SHJ solar cell. (a) Schematic of all the layers involved in the solar cell. (b) Band diagram of the silicon based elements in a SHJ solar cell. Neither are drawn to scale.

2. Substitutional defects - dopant atoms such as phosphorus or boron
3. Vacancies - Missing Si atoms in the lattice
4. Self interstitial defects - extra Si atoms in the lattice

These defects have been illustrated by Schroder in Figure 1.3a. [15] Further types of defects can also include dislocations and other perturbations of the crystalline lattice. These defects also have well documented electrical characteristics. Adding different defects to a crystal lattice allows for other allowed electronic states within the forbidden gap between the conduction and valence bands and act as recombination centers. For c-Si, specifically, these have been studied and assigned energy positions by Watkins. [16, 17] This is shown in Figure 1.3b These electronic states serve as recombination centers and adversely affect the performance of c-Si solar cells.

The c-Si used in the study of this thesis is FZ c-Si. The bulk crystal of FZ c-Si has a very low defect density. Therefore, for bulk recombination processes, defects are not of great consideration. [18] However, at the surface of the wafer, the crystal lattice terminates, which leaves some silicon atoms with less than the normal four bonded neighboring atoms. This results in surface dangling bond defects which causes excessive recombination at the surface. [19] Extra care must be taken with all c-Si solar cells to ensure that these surface defects are properly passivated to reduce recombination to ensure good electrical performance of the solar cell.

Passivation can be achieved through two distinct mechanisms. These are, namely, chemical passivation and field effect passivation. Chemical passivation is achieved

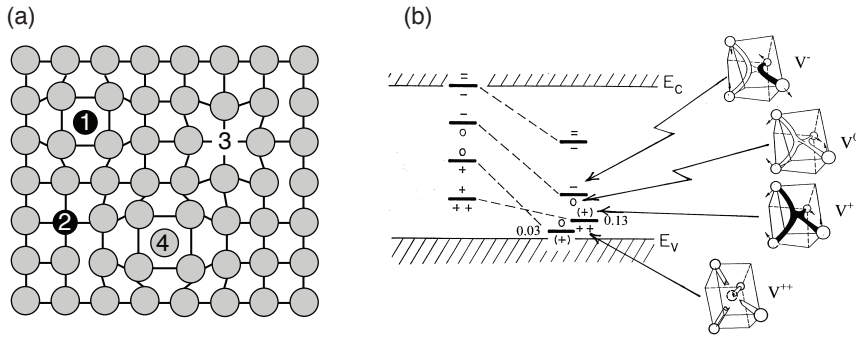


Figure 1.3: Description of the defects in c-Si. (a) Illustration of spatial representation of c-Si defects. (1) Foreign interstitials, (2) foreign substitution, (3) vacancy, (4) self interstitial. [15] (b) Energetic positions of defects in c-Si. [17]

through bonding the surface dangling bonds with other elements. One way of achieving this is through dipping a c-Si wafer in hydrofluoric acid (HF) which will strip away the native oxide that forms at the surface and leave the wafer with surface atoms bonded by hydrogen atoms, though this technique, by itself, is not fully stable. [20] Field effect passivation uses an electric field to repel either electrons or holes from the surface. Since recombination through defect states requires both electrons and holes, reducing the density of one of the charge carriers at the surface reduces the possibility of recombination.

There are many different passivation techniques used for c-Si in PV applications. These range from cleaning procedures or thermal treatments that result in passivating oxides, to adding dielectric layers such as silicon nitride or aluminum oxide, or a combination of oxides and dielectrics. [21, 22] However, a major drawback of using some of these layers are that they are insulators and therefore either need to be pierced through by metal, be thin enough for tunneling or require additional processing steps to assure that electrical contact is possible. Though these techniques work, and can result in many successful solar cell technologies, they do exhibit these drawbacks and many require very high processing temperatures that can be costly and potentially reduce the quality of the silicon wafer. [19]

SHJ solar cells use passivation by a-Si:H. This method of c-Si passivation was first accomplished in the 1970's. [23, 24] The first photovoltaic application was in 1983. [13] The hydrogen in a-Si:H as well as the disordered nature of the material results in a structure with a much smaller dangling bond (DB) density per unit area as a bare silicon wafer through hydrogenation of the surface defects. [25] The larger bandgap of a-Si:H also adds a barrier for minority charge carriers resulting in field-effect passivation. [26] Though both of these mechanisms exist, chemical passivation has been shown to be the primary factor in the excellent passivation

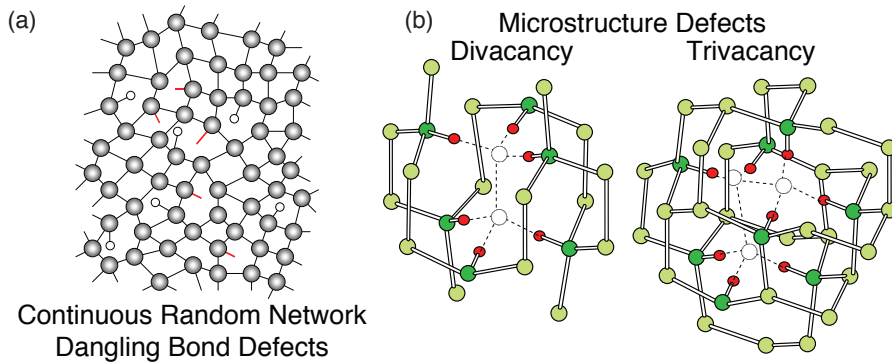


Figure 1.4: Two models of defects in a-Si:H. (a) Continuous random network model where densities of dangling bonds is the defect of interest. (b) Divacancies and trivacancies showing how the microstructure surrounding also plays a role. [30]

quality of a-Si:H. [19]

1.3.2 a-Si:H Defects

Defining defects in a-Si:H is more complicated than in c-Si. This is due to the fact that a-Si:H is, by nature, disordered so there is not a crystalline matrix that can be characterized as structured or defective. However, in a-Si:H, unpaired dangling bonds can exist. [27] These are defined as silicon atoms with less than four neighboring bonded atoms resulting in an unbound valence electron. Dangling bonds can exist in densities of $10^{16} - 10^{19} \text{ cm}^{-3}$ in a-Si:H. [28] These dangling bonds act as recombination centers for charge carriers and reducing their density is of great importance when using a-Si:H as a material for photovoltaic applications.

When discussing a-Si:H, the sheer volume of dangling bonds is not the only property of interest. The microstructure of the material also has bearing on its ability to perform well as an absorber layer for photovoltaic applications. This can be done by treating dangling bonds not only as individual entities but viewing their surroundings as vacancies or voids. [29, 30] Figure 1.4 shows how these defect terms are defined. Voids represent holes in the material and are up to nanometers in scale.

1.3.3 Light-Induced Degradation

Both c-Si and a-Si:H are susceptible to light induced degradation (LID). This means that through light exposure, certain defect densities in c-Si or a-Si:H will increase to a certain point. In c-Si, LID is linked to boron-oxygen interstitial defects in p-type c-Si. [31] This has been known to reduce efficiencies of p-type c-Si

solar cells by as much as 10 % of their initial efficiency. [31] However, SHJ solar cells predominantly use n-type c-Si. Furthermore, FZ wafers have very low oxygen content so even those that use p-type materials will have such a low density of oxygen defects that this is negligible. However, if CZ, p-type wafers are used, then LID due to boron-oxygen interstitials must be considered.

a-Si:H is very susceptible to LID. This was discovered first by Staebler and Wronski in 1977 and is therefore called the Staebler-Wronski Effect (SWE). [32] This work showed that upon illumination both the dark and photoconductivity reduced. This has been shown to be the result of dangling bond density increasing in a-Si:H. These effects are shown in Figure 1.5a. As a result the quality of a-Si:H solar cells drops significantly from the as deposited values. This is usually linked to a reduction of fill factor in solar cells. [33] An example experiment of an a-Si:H solar cell is shown in Figure 1.5b. Solar cells made from thicker a-Si:H absorber layers degrade more upon light exposure. [34] Mitigation of this effect has shown to be challenging, but methods that are commonly used are to dilute the layer with hydrogen, reduce the layer thickness and to use triode mesh deposition techniques. [35, 36] This effect has been defined as metastable as a-Si:H quality can be partially recovered through annealing. This has been observed in both defect densities of a-Si:H films and quality of a-Si:H solar cells. [37]

There are various measurement techniques to study defects in a-Si:H. Electron Paramagnetic spin Resonance (EPR) is a way to measure unpaired electrons to determine dangling bond density in the material. [38] Fourier Transform Infrared Spectroscopy (FTIR) allows for gathering information about silicon-hydrogen bonds from which microstructure information can be obtained. [29, 35] Finally Fourier Transform Photocurrent Spectroscopy (FTPS) can be used to gather information about absorption at very low levels and studying this absorption can reveal information about electronic states in the bandgap. [39] FTPS can be used for measuring a-Si:H film properties and also for measuring full thin film solar cell devices. [40] This thesis also investigates whether this technique is valid for studying interface defects in SHJ solar cells.

1.3.4 Metastability of the a-Si:H/c-Si Interface

As a-Si:H plays an important role in SHJ solar cells, work has been done to study whether the metastable properties of a-Si:H defects affect SHJ solar cells. At the functional device level, the current consensus is that SHJ solar cells are not susceptible to LID. [14, 41] This is mainly due to the thickness of the a-Si:H layers. As they are on the order of 5-10 nm, the changes are not great enough to affect the electrical or optical performance of the entire SHJ solar cell. [41] However, when one looks deeper into the minority carrier lifetime of c-Si samples passivated by a-Si:H, changes due to both light soaking and annealing are observed.

De Wolf et al. has shown changes in minority carrier lifetime in SHJ samples through light soaking. [42, 43] This change in minority carrier lifetime has been linked strictly to an increase of dangling bond density using a model on the am-

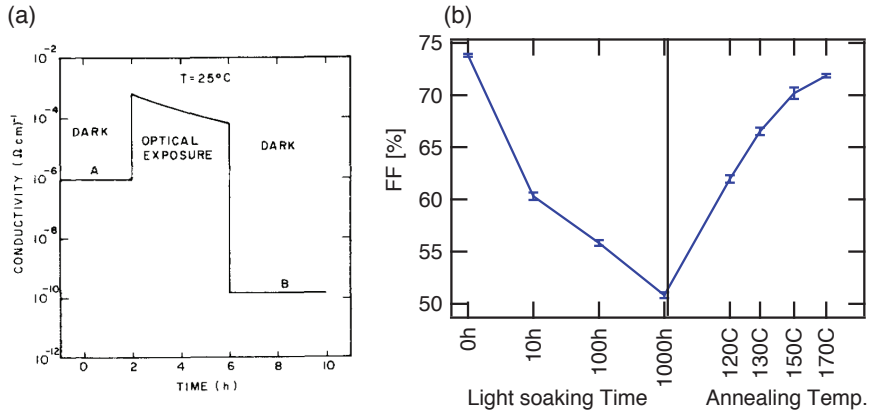


Figure 1.5: Staebler-Wronski effect represented by: (a) Reduction of photoconductivity and dark conductivity of a-Si:H due to light soaking. [32] (b) Degradation of the fill factor of an a-Si:H solar cell due to light soaking followed by a partial recovery upon thermal annealing.

photonic nature of dangling bonds in SHJs. [44] Another finding of De Wolf was that c-Si wafers passivated with a-Si:H that have $\langle 111 \rangle$ orientation do not exhibit light induced changes whereas wafers with $\langle 100 \rangle$ wafers do. [43] This is shown in Figure 1.6a. The degradation of lifetime has been shown to be partially reversible through annealing. [45] Furthermore the process of annealing induced lifetime improvements has been studied using ex-situ annealing measurements. [42, 46, 47] These works demonstrate that the minority carrier lifetime of an c-Si wafer passivated with a-Si:H follows a stretched exponential increase upon annealing. This is shown in Figure 1.6b.

Other work has shown that there can also be light induced increases in lifetime. [48] In this work doped layers are also applied which reduce the as-deposited lifetime of the samples. However, upon light exposure, their lifetime increases. This enhancement of lifetime is explained by enhanced field effects provided by the doped layers causing hydrogen to move towards the heterointerface, thus increasing the chemical passivation.

While these metastability effects do not inherently affect the quality of full SHJ devices, the physics at hand are very interesting. Studying these light and annealing induced effects on the minority carrier lifetime of SHJ structures further can help to understand physical properties of the a-Si:H/c-Si interface. Furthermore, these studies also aid in better understanding the nature of the SWE in a-Si:H as this method is a sensitive way to detect subtle changes in interface dangling bond densities.

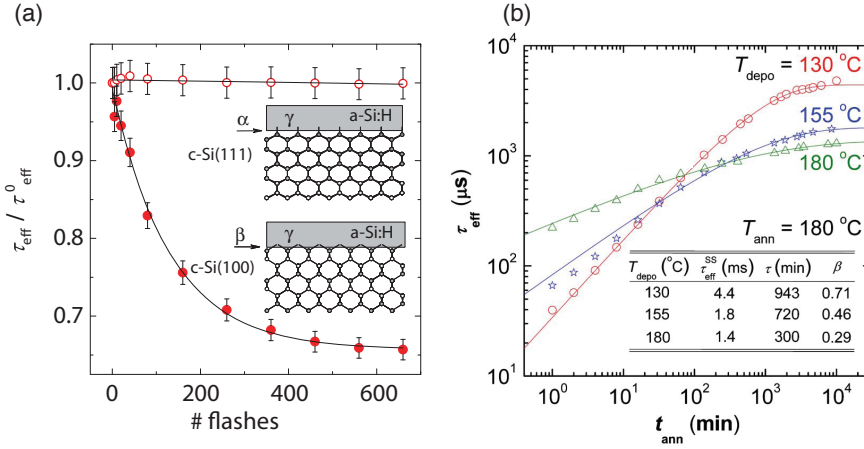


Figure 1.6: Work of De Wolf et al. on SHJ interface metastability. (a) The effective lifetime (τ_{eff}) of n-type $\langle 100 \rangle$ passivated wafers degrading with light soaking while $\langle 111 \rangle$ wafers do not exhibit this behavior. [43] (b) τ_{eff} increasing due to annealing at different rates depending on annealing temperature. [42]

1.4 Novel Application of SHJ Solar Cells: Solar Based Water-Splitting

One important challenge in using solar energy as a major source for electricity is storage. Daily and seasonal fluctuations in solar energy do not match up with electricity demand therefore storage solutions are of utmost importance in an electricity system dependent on solar energy. Though batteries are primarily used in small scale home systems now, other solutions are being investigated as batteries have a low mass and volumetric energy density. One possibility is to use hydrogen storage. In this case electrolysis is performed splitting water into hydrogen and oxygen. [49] There is a growing field of work attempting to accomplish this using a photoactive electrode and this is referred to as photo-electrochemical (PEC) water splitting. [50] There is a growing level of interest in silicon based solar cell technologies for use in PEC applications. [51] Part of this thesis examines how SHJ technology can be used in such applications.

1.5 Goals and Outline of Thesis

The goals of this thesis are to answer the following research questions:

1. What is the nature of the metastable properties of a-Si:H passivation of c-Si?
 - a) How is the a-Si:H/c-Si interface affected by annealing?

- b) How is the a-Si:H/c-Si interface affected by light soaking?
 - c) How does adding doped layers affect these metastable properties?
2. Can Fourier Transform of Photocurrent Spectroscopy (FTPS) be used to better understand the a-Si:H/c-Si interface?
 3. How can novel applications using SHJ solar cells be used to aid in water-splitting applications?

This thesis is structured in eight distinct chapters. Chapter 1 (this chapter) serves as an introduction to the thesis. This is followed by Chapter 2 which gives the methodology used in the different experiments presented in this work. These two chapters are then followed by the bulk work of the thesis.

Chapter 3 explains how to apply current models on lifetimes to properly execute in-situ annealing experiments on the a-Si:H/c-Si interface. Chapter 4 then examines the light induced effects on the a-Si:H/c-Si interface. In Chapter 5, doped layers are added to the a-Si:H/c-Si samples to examine their effects on the light induced kinetics of the passivation quality.

Chapter 6 then examines the feasibility of using FTPS to study defects in SHJ solar cells. This chapter also includes some work done on poly-Si solar cells on glass as it was discovered that FTPS is not suitable for interface defect study. This is followed by Chapter 7, which deviates from the fundamental questions and moves to applications of a novel SHJ/thin-film silicon hybrid cell for water-splitting.

Finally, Chapter 8 outlines the main results of this work. This chapter summarizes the insights found throughout the thesis that help to answer the research questions. This chapter also gives recommendations for further exploration and future work in this field of study.

2

Methodology

This chapter describes the experimental techniques used in this thesis. The purpose of this chapter is to allow readers of this thesis the ability to fully replicate and challenge the conclusions drawn here. Section 2.1 focusses on the sample preparation techniques detailing the substrates used and thin film processing used throughout this thesis. Section 2.2 focusses on the characterization tools used from film characterization to full device characterization. Finally, Section 2.3 describes the simulation tools used in this work.

2.1 Sample Preparation

Silicon heterojunction (SHJ) samples were prepared from pre-fabricated wafers by TOPSIL. These crystalline silicon (c-Si) wafers were prepared by a float-zone (FZ) procedure. The c-Si wafers had a resistivity of 2-5 Ωcm and were doped with phosphorous (n-type) or boron (p-type). Crystal orientations of $\langle 100 \rangle$ and $\langle 111 \rangle$ were used. These wafers were approximately 280 μm thick and 4.0 inches in diameter.

Preparation of full SHJ devices from wafers requires six major steps (see Figure 1.2 for full schematic of finished SHJ device):

1. Wafer cleaning
2. Plasma enhanced chemical vapor deposition (PECVD) of intrinsic hydrogenated amorphous silicon (a-Si:H) layers
3. PECVD of doped a-Si:H layers for the emitter and back surface field (BSF)

4. Sputtering of indium doped tin oxide (ITO) layers
5. Evaporation of full metal contact at the rear
6. Evaporation of grid metal contact at the front

The majority of the samples prepared for investigation in this thesis were not full SHJ devices but wafers passivated with intrinsic a-Si:H. Because no ITO or metallization are required for these samples, steps 4, 5 and 6 were not carried out. However, in the Chapter 7 full devices were prepared including single junction SHJ devices and SHJ devices in tandem with thin-film nanocrystalline silicon (nc-Si:H). These steps are all briefly explained here.

2.1.1 Wafer Cleaning

An as purchased silicon wafer has to be cleaned before a-Si:H deposition to remove organic contaminants and strip away the native oxide that occurs after air exposure. There are various techniques available to perform this cleaning. So-called dry cleaning techniques such as plasma processing are available, but they result in damage to the wafer surface due to ion-bombardment. Therefore, for typical SHJ preparation, wet cleaning methods are used. [19, 52, 53] There are many wet cleaning procedures used to clean wafers. [54] The method chosen for this thesis was developed by Dr. Dong Zhang. [55] This method has been compared to other standard cleaning methods such as Piranha and RCA. [56]

The first step is to dip the wafer in 99 % HNO_3 for 10 minutes at room temperature to remove organic contaminants. This is followed by a dip of 10 minutes in fuming 69.5 % HNO_3 for 10 minutes to remove metallic contaminants. Both of the HNO_3 steps result in an oxide at the surfaces of the wafer in addition to the native oxide that is formed by the wafer in air.

The final step before a-Si:H deposition is to strip this oxide away. This is done by a dip in a 0.5 % HF solution. In different experiments throughout this thesis, the HF time was varied to study effects on the lifetime kinetics. However, in general, the HF dip should be long enough to completely strip away the oxide. A typical way to observe if the oxide has been removed is to look at the hydrophobicity of the wafer. If water still sticks to the wafer after the HF dip, then there is still oxide present, while a totally stripped wafer will be completely hydrophobic. [57, 58] However, leaving the wafer in HF for prolonged periods of time after the oxide layer has been completely stripped can cause an undesirable microroughness that can negatively influence the electrical properties of the final SHJ solar cell. [55] Therefore it is best to optimize the HF dip time by monitoring the effective minority carrier lifetime (see Section 2.2.1). After the HF dip, the wafer is dipped in deionized water and then transferred to the a-Si:H deposition equipment.

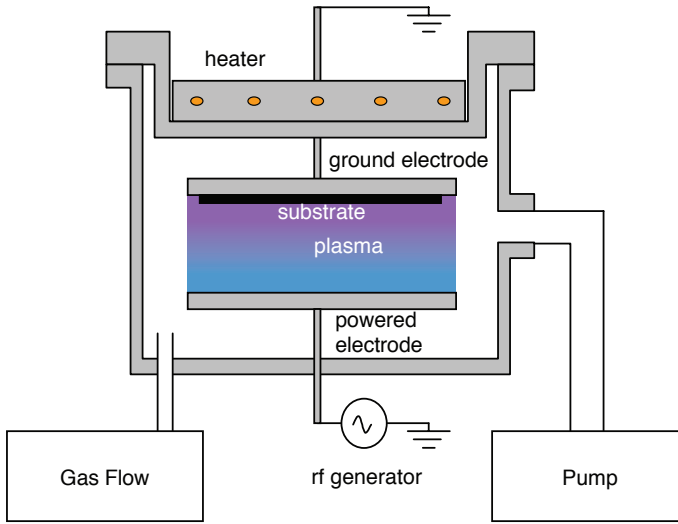


Figure 2.1: Schematic of a PECVD reaction chamber.

2.1.2 Plasma Enhanced Chemical Vapor Deposition

After wafer cleaning, the next step is to deposit thin-film, a-Si:H layers. In this thesis, a-Si:H was deposited using plasma enhanced chemical vapor deposition (PECVD). A cleaned wafer is moved into a chamber and connected to a grounded electrode. Parallel to this grounded electrode is a powered electrode. Precursor gasses are pumped into the chamber and then an AC voltage at a frequency of 13.56 MHz (RF) is applied across the two electrodes. See Figure 2.1. A spark then ignites the gasses into a plasma in the chamber, which results in dissociated precursor gasses. This plasma is then made up of a complex mixture of ions, radicals, atoms and electrons. The dissociated elements undergo a reaction with the surface of the c-Si wafer that starts the growth of a thin film of a-Si:H.

The PECVD deposition machine used in this thesis has 4 chamber system. Each chamber was responsible for a specific thin film layer. There were separate chambers for the p-layers, n-layers and i-layers as well as one chamber for experimental layers. For all cases, Silane (SiH_4) was used as a precursor gas for the silicon and hydrogen in the a-Si:H. In some cases, the gas was diluted with more hydrogen gas (H_2). Diborane (B_2H_6) was used for boron (p-type) doping and phosphine (P_2H_4) was used for phosphorus (n-type) doping. Varying the flow rate of these gasses will have an effect on the growth rate and chemical composition of the final films deposited on the c-Si wafer.

Aside from the flow rate of the precursor gasses, other important parameters

include the power density, pressure and electrode distance. These parameters should all be optimized depending on the desired properties of the final thin films produced.

Finally, the frequency of the applied voltage can be varied. In this thesis, radio frequency (RF) PECVD is used at a frequency of 13.56 MHz. However, other groups have seen promising thin film silicon results using very high frequency (VHF) voltages. [59]

2.1.3 Sputtering

Sputtering is used in order to deposit the transparent conductive oxides (TCO). Sputtering differs from PECVD in that it is a physical, not chemical, deposition method. Here the substrate is placed above a target of the desired material. Then an inert gas, argon, is pumped through the chamber. As the plasma is ignited, argon atoms bombard the target surface and this dislodges molecules from the target which diffuse towards the substrate.

In the work here, the desired material is indium doped tin oxide (ITO - $\text{InO}_2:\text{SnO}_3$ at a ratio of 9:1).

2.1.4 Metal Evaporation

The final step to create a SHJ solar cell is the metallization. Metallization can be done with various techniques such as plating, screen printing and others. The technique used in this thesis is physical vapor deposition by evaporation. A three layer stack of metal is used here: Ag (100 nm), Cr (30 nm), Al (1.9 μm).

The evaporation of Ag is accomplished through thermal evaporation as it has a relatively low melting point of 960 °C. Al also has a low melting point, but because of its ability to alloy with the tungsten in the crucible, thermal evaporation is not a suitable method. For Al and Cr, e-beam evaporation is used. In this case, an electron beam is directed towards the crucible containing the metal and the energy from the e-beam is enough to cause the metal to evaporate. The wafer is placed above the metal targets and metal is evaporated through a mask in order to achieve the desirable metal pattern.

2.2 Characterization

Sample characterization was done through a number of methods throughout the work in this thesis. This ranges from measuring the effective carrier lifetime (τ_{eff}) using photoconductance decay on passivated wafers and cell precursors, to measuring JV measurements to characterize full solar cell devices. All the characterization tools are explained in this section.

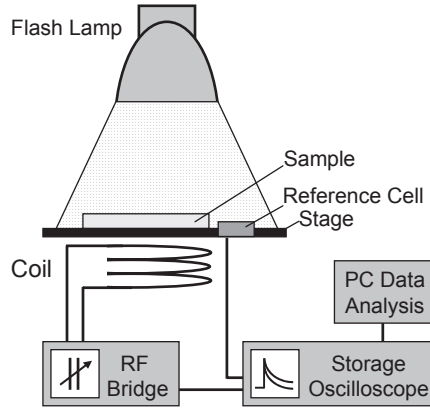


Figure 2.2: Schematic of a PCD measurement setup. [60]

2.2.1 Photoconductance Decay

The bulk of this work in this thesis is done through transient photoconductance decay (PCD). The main purpose of a PCD measurement is to get the effective carrier lifetime (τ_{eff}) of a given sample. In this case, the samples are passivated FZ, c-Si wafers or cell precursors that are not yet metalized. Figure 2.2 shows a schematic of the setup. The principle behind the setup is to illuminate the sample on a stage, thus exciting electrons in the bulk of the sample. Underneath the sample there is a coil which is inductively couples the sample to an RF bridge. The coil can sense the permeability of the sample and through that the conductance of the sample can be calculated. As the excited charge carriers decay, the induced photoconductance decays along with the density of carriers in the sample. Therefore the photoconductance is linked to the excess charge carrier density (Δn). The following explanation is extracted from Rein's book: "Lifetime Spectroscopy: A Method for Defect Characterization in Silicon for Photovoltaic Applications." [60]

Calculating τ_{eff} starts with the continuity equation below that explains how Δn changes with time during a decay of Δn :

$$\frac{\delta \Delta n}{\delta t} = G(t) - U(t) \quad (2.1)$$

Where G is the generation rate and U is the recombination rate. U is defined as:

$$U = \frac{\Delta n}{\tau_{\text{eff}}} \quad (2.2)$$

Therefore τ_{eff} can be written, in a general form, as:

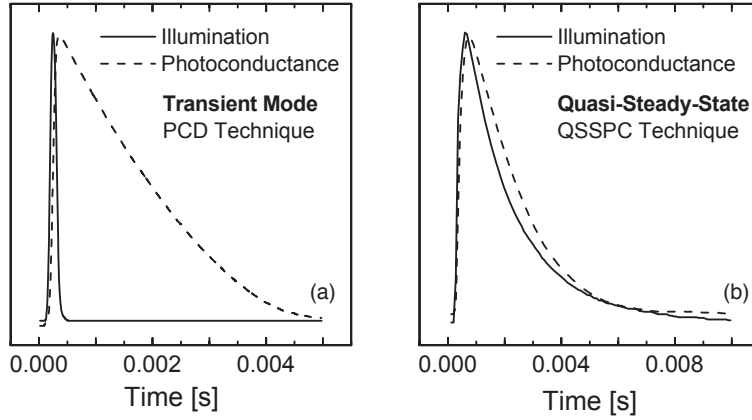


Figure 2.3: (a) Example of a PCD measurement that would use the transient method to calculate lifetime from the photoconductance curve. (b) Example of a PCD measurement that would use the QSS method to calculate the photoconductance curve. [60]

$$\tau_{\text{eff}} = \frac{\Delta n}{G - \frac{\delta \Delta n}{\delta t}} \quad (2.3)$$

This general case is useful for calculating the τ_{eff} , but it can be simplified in two general cases. The first is the quasi-steady-state (QSS) case. In QSS, $G \gg \frac{\delta \Delta n}{\delta t}$. This occurs when τ_{eff} is much lower than the decay time of the illumination source (See Figure 2.3b). For the WCT-100 setup used here, this means that τ_{eff} should be lower than 100 μs . In this case, τ_{eff} can be rewritten as:

$$\tau_{\text{eff}} = \frac{\Delta n}{G} \quad (2.4)$$

The other case is the transient case. Here it is assumed that τ_{eff} is much greater than than the decay time of the illumination source (See Figure 2.3a). Here there is no generation during the Δn decay so τ_{eff} can be rewritten as:

$$\tau_{\text{eff}} = \frac{\Delta n}{-\frac{\delta \Delta n}{\delta t}} \quad (2.5)$$

For the work done in this thesis, the τ_{eff} values are all above the 100 μs cutoff. Therefore, all the measurements done in this thesis were done using the transient simplification.

The relationship between τ_{eff} and Δn has been demonstrated. However, what is directly measured in a PCD measurement is the photoconductance of the sample ($\sigma(t)$). $\sigma(t)$ is linked to the photoconductance through:

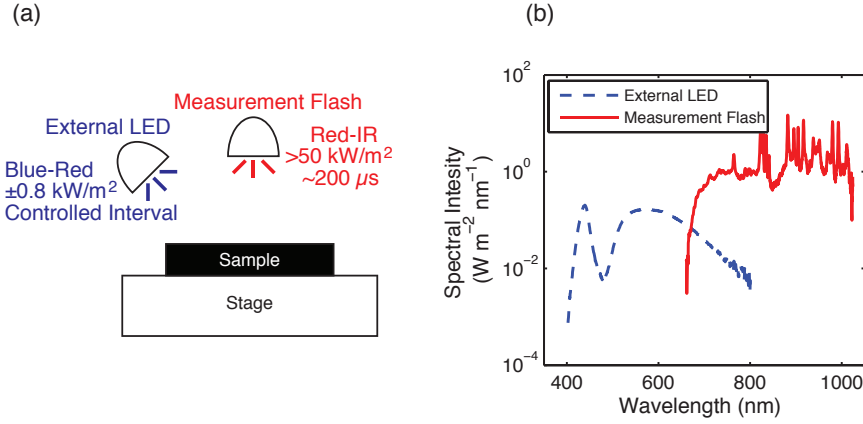


Figure 2.4: (a) Schematic of Sinton WCT-120 with additional light soaking LED. (b) Spectra of measurement flash of WCT-120 and external light soaking LED.

$$\Delta n(t) = \frac{\Delta \sigma(t)}{q (\mu_n + \mu_p) W} \quad (2.6)$$

Where W is the thickness of the wafer, q is the elementary charge of an electron and μ_n and μ_p are the electron and hole mobilities. Of note, the mobilities are also dependent on Δn , so an iterative calculation process must be used. Using all the equations presented in this section, a measured $\sigma(t)$ curve can be used to calculate back τ_{eff} as a function of Δn . Especially in Chapters 3, 4 and 5, this is used to extract information about the SHJ heterointerface.

Two setups are used here for this measurement. The first is a Sinton WCT-120 and the Sinton WCT-120-TS. The only difference between the two is that the Sinton WCT-120-TS has a temperature stage that can raise the stage temperature up to 200°C , while the Sinton WCT-120 keeps the stage at 30°C . Additionally, external light soaking was applied to the WCT0-120 setup. This setup, as well as the spectrum of both the measurement flash and the external light soaking LED is given in Figure 2.4

2.2.2 Spectroscopic Ellipsometry

The samples used in this thesis use thin films such as a-Si:H and ITO. Before utilizing these films in full solar cell devices or as passivation layers, the films need to be analyzed to obtain deposition rates and optical characteristics such as the complex refractive index ($n + ik$). This is accomplished in this thesis through spectroscopic ellipsometry (SE).

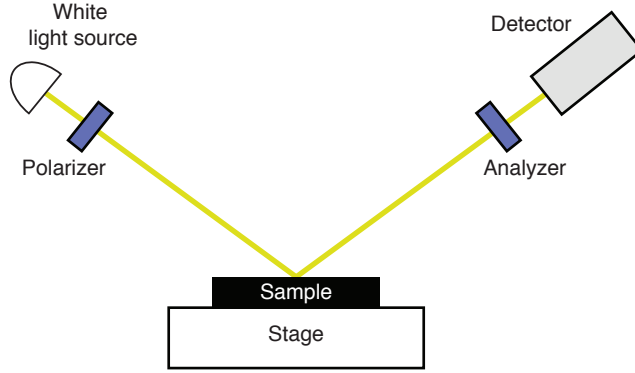


Figure 2.5: Schematic of spectroscopic ellipsometry setup.

To perform an SE measurement a thin film must be deposited on a substrate and then it is placed on a setup as shown in Figure 2.5. SE is based on the measurement of the change of polarization of light due to the reflection at an optical sample. Light is shone through a polarizer and both s and p polarized light are shone at different incident angles. The resultant light goes through an analyzer and then reaches a detector. The result is a wavelength dependent, complex value of the reflection from p polarized light (r_p) and s polarized light (r_s). This results in a complex ratio defined as ρ :

$$\rho = \frac{r_p}{r_s} \quad (2.7)$$

ρ is wavelength dependent and can be expressed as a complex number using the parameters Ψ and Δ :

$$\rho = \tan(\Psi)e^{i\Delta} \quad (2.8)$$

The wavelength dependent values of Ψ and Δ can then be fitted to optical models describing the film and substrate depending on the thickness and the n and k parameters of the different materials. In this way, the thickness, n and k values can be extracted from the SE measurement and used for other optical simulations. Further information like the bandgap among others can also be ascertained from this measurement.

In this thesis, a Cody-Lorentz model was used to approximate a-Si:H layers. This model was then used to fit the SE data measured to extract thickness and bandgap of the layers from the SE measurements.

2.2.3 Solar Cell Characterization

Once a solar cell is fabricated, the way to test its efficiency is to use a so called, illuminated JV measurement. This measures current density (J) versus applied voltage (V) under illumination. This work uses a AAA class, WACOM solar simulator to illuminate the solar cells with an AM 1.5 spectrum. From this measurement the open circuit voltage (V_{OC}) and short circuit current density (J_{SC}) can be obtained. Furthermore, the power at maximum power-point (P_{MPP}) can be measured giving the fill factor (FF).

Though the J_{SC} can be measured using the JV measurement, it can be more accurately determined through an external quantum efficiency (EQE) measurement. Rather than shining a full spectrum of light on the solar cell, the EQE setup uses a monochromator to shine individual wavelengths of monochromatic light on the sample. The current from that sample is measured and as the monochromatic light source is of a known intensity, the ratio of incident photons to collected electrons can be easily calculated. Integrating this over the spectrum with the AM 1.5 spectrum gives the J_{SC} . This J_{SC} is different from the one calculated by a JV measurement as shading losses are ignored. The EQE measurement also gives information about which wavelengths are being utilized better by the solar cell, thereby allowing for better understanding of where different current losses originate from.

2.2.4 Fourier Transform Photocurrent Spectroscopy

One technique that has been used to study defects in a-Si:H extensively is Fourier Transform Photocurrent Spectroscopy (FTPS). An exploration on the feasibility of the use of FTPS on SHJ interface defects is given in Chapter 6.

The technique uses a Michelson interferometer to shine light on a given sample. Figure 2.6 shows this. A light source hits a beam splitter that sends a portion of the light to a fixed mirror and a moving mirror which scans over various distances. At each given moving mirror distance, the photocurrent of the sample is measured under illumination of the source light. This illumination is composed of both the reflection from the translating mirror and the fixed mirror. The result is a moving mirror dependent current graph known as an interferogram.

Because of the difference in path length of (OF - OM in Figure 2.6), different wavelengths will have different interference patterns based on what fraction of their wavelength is represented by that difference. Therefore, using a Fourier transform, one can take the interferogram and obtain a wavelength dependent photocurrent. This has advantages over other photocurrent techniques in that the scan can be faster, and more accurate in terms of both resolution and signal to noise ratio. [39]

There are two main modes that can be used to utilize FTPS for photovoltaic applications. The first mode is to deposit a single thin film layer with contacts and apply a large voltage across the sample to measure the photoresponse. This

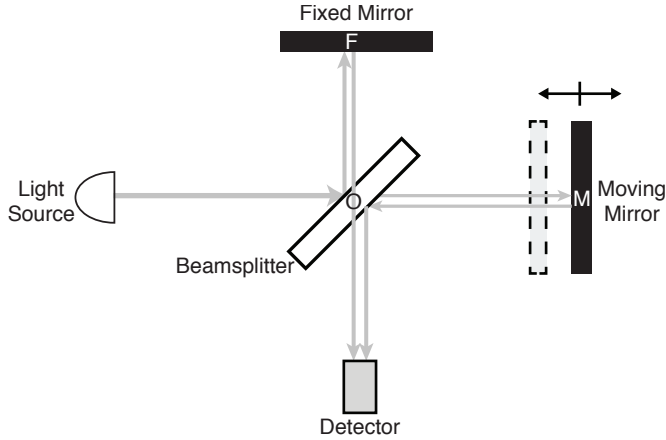


Figure 2.6: Michelson interferometer. [61]

has been done by many research groups to obtain information about sub-band gap absorption which can be linked to defects in various photovoltaic materials. [62, 63] However, another method is to use a full solar cell device and measure what is equivalent to a sub-band gap EQE of the solar cell. Here, no external field is required and the observed solar cell photocurrent can be linked to defects in the absorber material. [40] This, so-called FTPS-EQE measurement is used here to study various solar cell technologies, including SHJ solar cells.

2.2.5 Fourier Transform Infrared Spectroscopy

Fourier transform infrared spectroscopy (FTIR) is used to study the microstructure of a-Si:H. The fundamental principle behind this technique is to use the same interferometer as in an FTPS measurement, but to measure the transmission rather than the photocurrent. [64] Different vibrational modes in the FTIR signal have been linked to different contributions of different bonds. Of note in this thesis are the modes of the silicon-hydrogen bond. There is a wagging mode of this bond at a wavenumber of approximately 630 cm^{-1} and stretching modes around 2000 cm^{-1} . [29] Analyzing the wagging mode is a good method to approximate the hydrogen content of the a-Si:H. The stretching mode can be approximated by a contribution of a high stretching mode and low stretching mode which are linked to different microstructures in the a-Si:H. This process is described further in Chapter 4.

2.3 Optical Simulation

Optical simulation uses the optical parameters of thin films, wafers and other substrates to determine the wavelength dependent transmission, reflection and absorption of stacks of different materials. In order to simulate this, the thickness and complex refractive index ($n + ik$) of all different layers must be known. Using this knowledge Fresnel equations are solved to determine the reflection between layers at different wavelengths and the absorption coefficients are calculated from the k values to determine how much light is absorbed in each layer. [65]

These simulation techniques have many applications including determining parasitic and reflection losses in the device. In this thesis, however, the optical simulations are primarily used to determine optimal thicknesses for current matching in Chapter 7. Here the total absorption can be linked to a current in the active layers of the two junctions in the tandem cell and thicknesses can be varied until both cells achieve equivalent current.

3

Temperature Effects on the a-Si:H/c-Si Interface Model using the Amphoteric Nature of Dangling Bonds

This chapter has been submitted to AIP Advances for publication

Abstract

This work proposes a model to simulate the carrier injection dependent lifetime of crystalline silicon passivated with hydrogenated amorphous silicon at elevated temperatures. Two existing models to respectively calculate the bulk lifetime and surface recombination velocity are used though these models are currently only presented in literature at room temperature. The temperature dependent model is described here in detail. Experimental results using this model show that the kinetics of lifetime evolution of silicon heterointerfaces are not universal. Furthermore, comparisons to simply using the room temperature model at elevated temperatures is given and significant differences are shown when using temperatures above 100 °C showing the necessity of using this model to properly do in-situ annealing experiments.

3.1 Introduction

Silicon Heterojunction (SHJ) solar cells are the world record holding silicon-based solar cell technology. Panasonic pioneered and utilized this technology to break the record for silicon based single junction solar cells with their Heterojunction with Intrinsic Thin film (HIT) interdigitated back contact (IBC) solar cell achieving 25.6 % efficiency at standard test conditions. [10] In order to improve the performance of solar cells based on this technology a deep understanding of the surface passivation of silicon wafers using hydrogenated amorphous silicon (a-Si:H) is vital. The passivation quality at the surface is a large factor in achieving the high open circuit voltage (V_{OC}) necessary to reach such high efficiencies. [19] Given the metastable nature of defects in a-Si:H caused by the Staebler Wronski Effect [32], research groups have been investigating the effect of light soaking and annealing on the passivation quality of SHJ interfaces. [43, 48] One way to undergo this investigation is to use photoconductance decay measurements developed by Sinton to study the carrier injection dependent lifetime of wafers passivated with a-Si:H. [66] In order to extract further information from these measurements, models that link the lifetime measurement to surface defect density (N_S), charge density (Q_S) and capture cross section (σ) can be used. [67, 68]

Studies have attempted to understand the nature of SHJ passivation by a-Si:H using post-deposition annealing. [42, 48] Furthermore, SHJ solar cells have been shown to have very good performance at higher temperatures. [19] This has been studied in more detail recently. [69] One method to study these effects is to use lifetime measurements carried out on a temperature stage that can be elevated to 200 °C. The complex models used to extract N_S , Q_S and σ from the lifetime measurements contain many parameters that are temperature dependent and use of them in literature thus far. This chapter first explains, in detail, how these models can be adapted to other temperatures. This is followed by annealing experiments to show a potential application of this temperature dependent model.

3.2 Lifetime Models Used in This Work

The foundations for the modeling used in this chapter are the bulk recombination model of Richter et al. and the surface recombination model by Olibet et al. [67, 68] Combining these models gives a carrier injection level dependent effective lifetime (τ_{eff}) that can be used to simulate and match the photoconductance decay (PCD) measurements. Using these models, the surface defect density (N_S) and surface charge (Q_S) can be extracted from these PCD measurements. This is done using the following equation: [60]

$$\frac{1}{\tau_{eff}} = \frac{1}{\tau_{bulk}} + \frac{1}{\tau_{surf}} \quad (3.1)$$

Where τ_{bulk} is the bulk lifetime and τ_{surf} is the surface lifetime. τ_{surf} can be

calculated using the surface recombination velocities by:

$$\frac{1}{\tau_{\text{surf}}} = \frac{S_{\text{front}}}{W} + \frac{S_{\text{rear}}}{W} \quad (3.2)$$

Where W is the thickness of the silicon wafer, S_{front} is the front surface recombination velocity and S_{rear} is the rear recombination velocity. In the case that there is a symmetrical structure where S_{front} is equal to S_{rear} this equation can be rewritten equating both surface recombination velocities to an effective surface recombination velocity, S_{eff} .

$$\frac{1}{\tau_{\text{eff}}} = \frac{1}{\tau_{\text{bulk}}} + \frac{2S_{\text{eff}}}{W} \quad (3.3)$$

In order to extract the desired parameters, N_S and Q_S , τ_{bulk} and S_{eff} must be properly calculated using the Richter and Olibet models. [67, 68] These models are briefly discussed here to aid the reader in understanding the parameters that are sensitive to temperature.

3.2.1 Bulk Recombination Model

The bulk recombination model used here was proposed by Richter et al. [68] This model factors radiative and Auger recombination mechanisms for bulk crystalline silicon. Shockley Read Hall recombination is ignored here as both the high quality wafers used for SHJ solar cells have defect densities that have a negligible effect on the τ_{eff} . The equation for τ_{bulk} as a function of excess carrier concentration (Δn) is:

$$\tau_{\text{bulk}} = \frac{\Delta n}{(np - n_i^2) (2.5 \times 10^{-31} g_{\text{eeh}} n_0 + 8.5 \times 10^{-32} g_{\text{ehh}} p_0 + 3 \times 10^{-29} \Delta n^{0.92} + B_{\text{rel}} B_{\text{low}})} \quad (3.4)$$

Where g_{eeh} and g_{ehh} are enhancement factors introduced by Altermatt et al. [70]:

$$g_{\text{eeh}} = 1 + 13 \left\{ 1 - \tanh \left[\left(\frac{n_0}{3.3 \times 10^{17}} \right)^{0.66} \right] \right\} \quad (3.5)$$

$$g_{\text{ehh}} = 1 + 7.5 \left\{ 1 - \tanh \left[\left(\frac{p_0}{7 \times 10^{17}} \right)^{0.63} \right] \right\} \quad (3.6)$$

In Equation 3.4, B_{low} is the radiative recombination coefficient as measured by Trupke [71] for lightly doped silicon and B_{rel} is the relative radiative recombination coefficient determined by Altermatt. [70] The product of these two coefficients account for the radiative recombination component of bulk crystalline silicon and are both temperature sensitive. n_i is the intrinsic carrier concentration

of silicon, and n_0 and p_0 are the thermal equilibrium concentrations of electrons and holes respectively.

3.2.2 Surface Recombination Velocity Model

Once the τ_{bulk} has been calculated, the next step is to calculate the surface lifetime (τ_{surf}) which is given by the effective surface recombination velocity (S_{eff}) and the wafer thickness (W). One model to calculate S_{eff} is proposed by Olibet that considers the amphoteric nature of dangling bonds in a-Si:H and the c-Si surface. [67]

$$S_{\text{eff}} = \frac{U_S}{\Delta n} \quad (3.7)$$

Where U_S is the surface recombination rate. U_S is related to the surface electron and hole densities by:

$$U_S = \frac{n_S \sigma_n^0 \nu_{\text{th-e}} + p_S \sigma_p^0 \nu_{\text{th-h}}}{1 + \frac{p_S \sigma_p^0}{n_S \sigma_n^+} + \frac{n_S \sigma_n^0}{p_S \sigma_p^-}} N_S \quad (3.8)$$

Where n_S and p_S are the charge carrier surface densities. $\nu_{\text{th-e}}$ and $\nu_{\text{th-h}}$ are the thermal velocities of electrons and holes in silicon and N_S is the surface defect density. σ values here are capture cross sections for defects with designations corresponding to the charge carrier and the direction of carrier capture. These terms are defined as follows:

- σ_n^0 - capture cross section of neutral states for excited electrons
- σ_p^0 - capture cross section of neutral states for holes
- σ_n^+ - capture cross section of positively charged states for excited electrons
- σ_p^- - capture cross section of negatively charged states for holes

A more detailed description of these terms can be found in the work of Olibet et al. [67]

To calculate the n_S and p_S values, the following equations are used:

$$n_S = (n_0 + \Delta n) e^{\frac{q(\psi - \phi_n)}{k_B T}} \quad (3.9)$$

$$p_S = (p_0 + \Delta n) e^{\frac{-q(\psi - \phi_p)}{k_B T}} \quad (3.10)$$

Where Δn is the injection level, n_0 and p_0 are the electron and hole carrier densities at thermal equilibrium, q is the elementary charge, k_B is Boltzmann's constant and T the temperature of the substrate. ϕ_n and ϕ_p are the quasi Fermi levels

of electrons and holes at the edge of the space charge region. ψ is the surface potential. Using these parameters, the surface charge can be calculated:

$$Q_S = \pm \sqrt{\frac{2k_B T n_i \epsilon_0 \epsilon_{Si}}{q^2} \left[e^{\frac{q(\phi_p - \psi)}{k_B T}} - e^{\frac{q\phi_p}{k_B T}} + e^{\frac{q(\psi - \phi_n)}{k_B T}} - e^{\frac{-q\phi_n}{k_B T}} + \frac{q\psi(p_0 - n_0)}{k_B T n_i} \right]} \quad (3.11)$$

Where ϵ_0 is the vacuum permittivity and ϵ_{Si} is the relative permittivity of silicon. Using an iterative fitting method, the n_S and p_S values can be calculated back from a given Q_S value. This eventually can work back to a S_{eff} value that can be used, in combination with τ_{bulk} that was calculated in Equation 3.4, to fit to a measured τ_{eff} from a PCD measurement. Therefore, Q_S , N_S and σ values can be calculated back from a τ_{eff} measurement. Though this model is a powerful tool to gain information about the passivation quality of a given SHJ sample, care must be taken to ensure its accuracy when the sample is at a temperature above room temperature.

3.3 Temperature Dependencies

In order to perform in situ annealing experiments using this model, the effects on temperature must first be decoupled from the model. If the goal is to see how N_S , Q_S and the σ values change upon annealing, one must be very careful to first make sure that all parameters of the model are modified to their proper value at elevated temperature. Seif et al. briefly explained this when exploring the temperature coefficient of silicon heterojunction solar cells. [69] However, this section expands on all of the parameters that have to be accounted for in the model. These are, primarily, the bandgap, effective density of states, the carrier densities, thermal velocity, permittivity and Fermi level. In addition to these semiconductor properties aspects of recombination processes need to be taken into account, namely, radiative recombination coefficients and σ .

This section is composed of different parameters used in the model and their temperature dependence. Sources for the temperature dependence of each parameter is given along with how that parameter fits into the overall model for τ_{eff} . Following these descriptions, Section 3.3.5 illustrates how τ_{eff} changes with temperature once all parameters are taken into account.

3.3.1 Carrier Concentration

The intrinsic carrier concentration, n_i is dependent on the both the bandgap of the material as well as temperature: [72]

$$n_i = n_i(300K) \left(\frac{T}{300} \right)^3 e^{\frac{E_G(T)}{k} \left(\frac{1}{300} - \frac{1}{T} \right)} \quad (3.12)$$

where n_i is linked to the carrier densities n and p by $n_i = \sqrt{np}$. As is noted in Equation 3.12, the bandgap (E_G) also changes with temperature. This has been parametrized by Varshni with the following equation [73]

$$E_G(T) = E_G(0K) - \frac{\alpha T^2}{T + \beta} \quad (3.13)$$

Where $E_G(0K)$ of silicon is reported to be 1.170 eV. α and β are material specific constants that were determined to be 4.734×10^{-4} eV/K and 636 K respectively. [74]

In addition to n_i the carrier densities at thermal equilibrium n_0 and p_0 need to be calculated as well. For n-type semiconductors this can be shown as:

$$n_0 = \frac{N_D}{2} + \sqrt{\frac{N_D^2}{4} + n_i^2} \quad (3.14)$$

$$p_0 = \frac{n_i^2}{n_0} \quad (3.15)$$

Where N_D is the donor concentration. In the case of n-type semiconductors, n_0 can be approximated to N_D . Though N_D can vary at temperatures close to absolute 0, in the temperature range concerning annealing temperatures for SHJ interfaces, N_D can be held constant. However, since n_i does vary in these temperatures, p_0 has to be adjusted according to the temperature dependent n_i . These equations can essentially be duplicated for p-doped silicon with the adjustment that p_0 would remain constant (roughly equal to the acceptor concentration, N_A) while n_0 has to be adjusted for the changing n_i values.

3.3.2 Thermal Velocity

The thermal velocities of holes and electrons (v_{th-h} and v_{th-e}) are needed to calculate the recombination rate as shown in Equation 3.8. These values are defined by: [72]

$$v_{th-h} = \sqrt{\frac{8k_B T}{\pi m_h}} \quad (3.16)$$

$$v_{th-e} = \sqrt{\frac{8k_B T}{\pi m_e}} \quad (3.17)$$

m_h is the effective mass of holes (7.29×10^{-31} kg) and m_e is the effective mass of electrons (5.10×10^{-31} kg).

3.3.3 Fermi Level

Equation 3.11 is also dependent on the Fermi level of silicon. The Fermi level, however, is also dependent on temperature with the relationship for n-type: [60]

$$E_F - E_{Fi} = k_B T \ln \left(\frac{n_0}{n_i} \right) \quad (3.18)$$

and the relationship for p-type:

$$E_F - E_{Fi} = -k_B T \ln \left(\frac{p_0}{n_i} \right) \quad (3.19)$$

Where E_{Fi} is the intrinsic Fermi level, which is assumed here to be the middle of the bandgap.

3.3.4 Bulk Recombination Properties

Equation 3.4 shows the model used for calculating τ_{bulk} . The two radiative coefficients B_{rel} and B_{low} are temperature dependent. The temperature dependence of the product of B_{rel} and B_{low} (B) has been demonstrated by Altermatt and that relationship is used here. [70, 75]

3.3.5 Model Outcomes

The temperature dependencies of the lifetime models are shown in Figure 3.1. Here a sample thickness of 280 μm was used. An N_S of $1 \times 10^9 \text{ cm}^{-2}$ and a Q_S of $-1 \times 10^9 \text{ cm}^{-2}$ were used. The capture cross section ratios were: $\frac{\sigma_n^0}{\sigma_p^0} = 0.2$ and $\frac{\sigma_p^-}{\sigma_p^0} = \frac{\sigma_n^+}{\sigma_n^0} = 500$. These values were all held constant, while the temperature dependencies described in the previous section were considered. Therefore this figure shows how a change in temperature affects the different lifetime values, even if no annealing is taking place.

Figure 3.1a shows how τ_{bulk} varies with temperature according to the parameters described above. Note that there is practically no difference between the τ_{bulk} curves as a function of temperature. However, Figure 3.1b shows that S_{eff} does, indeed, change with temperature. Finally, Figure 3.1c shows the changes in the final τ_{eff} parameter as a function of temperature. It is clear here that in the injection levels of interest, there are significant changes in lifetime due to temperature. Overall, τ_{eff} decreases with temperature. If the temperature dependencies discussed in this chapter are not properly accounted for, differences in lifetime may be attributed to annealing when these differences are simply the result of property changes at elevated temperatures.

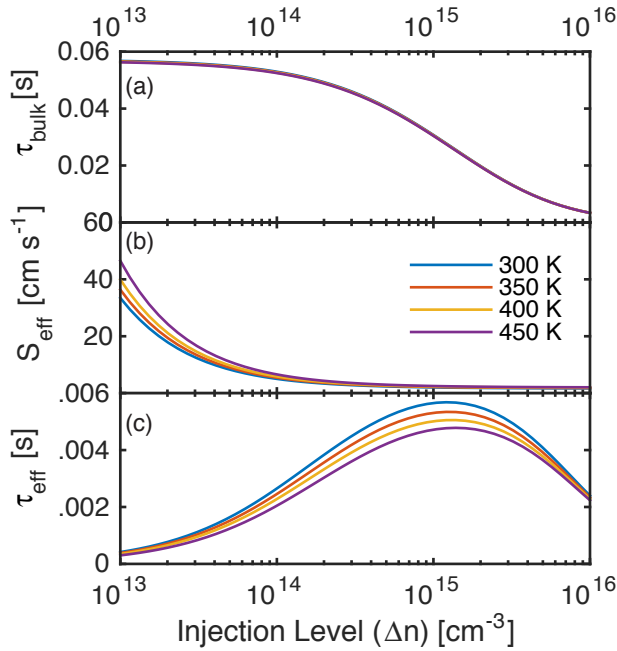


Figure 3.1: Model variations based on temperature. (a) shows the bulk lifetime (τ_{bulk}) as a function of carrier injection over a variety of temperatures with no practical variation, (b) shows the effective surface recombination velocity (S_{eff}) as a function of carrier injection level over a variety of temperatures and (c) shows the final effective lifetime (τ_{eff}) as a function of carrier injection level under the same variety of temperatures.

3.4 Experimental Results

In-situ annealing experiments were carried out on three passivated samples. The goal of these experiments was to examine c-Si wafers passivated with a-Si:H to gather insights into the annealing kinetics of the a-Si:H/c-Si heterojunction interface. The results of the experiments and the model outcomes are given first. This is followed by a comparison of the fitting results using the temperature adjusted model to the fitting results using the model at room temperature.

3.4.1 Experimental Details

Float zone, double polished, n-type c-Si wafers with $\langle 111 \rangle$ crystal orientation are used. Wafers were cleaned using a three step wet chemical cleaning procedure described elsewhere. [76] Both sides of each wafer were symmetrically passivated with 30 nm of a-Si:H using plasma enhanced chemical vapor deposition

(PECVD). The thickness of a-Si:H was held constant in order to account for thickness dependent effects on the lifetime. [77] Two different sets of deposition conditions for the a-Si:H were used. The first method, referred to here as undiluted a-Si:H was prepared using 40 sccm of SiH_4 at 0.7 mbar and at a power density of 0.015 W cm^{-2} . The second method, referred to here as diluted a-Si:H, was deposited using 4 sccm SiH_4 and 200 sccm H_2 at 8 mbar and at a power density of 0.056 W cm^{-2} . Both methods deposited at a substrate temperature of 180°C .

After the samples were prepared they were moved to the Sinton WCT 120-TS for τ_{eff} measurements. The stage has a controllable temperature. Samples were placed on the stage at room temperature and then the τ_{eff} was monitored at regular temperature increments until the stage reached 150°C . At this point the temperature stage remained at 150°C for two hours while the samples were measured at regular temperature intervals to monitor changes in the passivation quality during annealing. Each lifetime measurement both in the temperature ramp up phase and the longer term annealing phase represents an average of five measurements. Error bars on the fitting results represent the confidence interval of that parameter in the fit.

3.4.2 Annealing Experiments Using the Temperature Adjusted Model

Figure 3.2 shows the results of the annealing experiment on a sample using undiluted a-Si:H. In this case it is observed that the Q_S value stays within error margins throughout the annealing process while the N_S decreases as the sample is annealed. This is consistent with the findings of De Wolf et al. [42] However, this is not always the case. Figure 3.3 shows a repetition of this experiment where the N_S value stays within fitting error throughout the annealing process. Though it is unclear exactly why this sample exhibited a lower susceptibility to annealing, this shows that that samples passivated with a-Si:H do not always exhibit increased passivation quality upon thermal annealing.

Another finding from Figure 3.3 is that though the τ_{eff} curves, indeed, change significantly throughout the changes in temperature as shown in Figure 3.3a, the model does not show a corresponding change in N_S when differences in temperature are taken into account in Figure 3.3b. This shows importance of using this model when characterizing in-situ annealing experiments for c-Si wafers passivated with a-Si:H as changes in τ_{eff} may be due only to the material properties of Si changing rather than an actual reduction of N_S .

Figure 3.4 shows the results of the annealing experiment run on a sample using diluted a-Si:H. This method of a-Si:H passivation has been shown to be very susceptible to annealing effects especially when deposited at lower temperatures. [35, 47] Using this in-situ experimental method, it is revealed that most of the improvements in diluted a-Si:H passivation occur on very fast timescales during the temperature ramp up, itself. Figure 3.4c in particular shows that the majority of the reduction of N_S occurs during the temperature ramp-up from around 70°C to

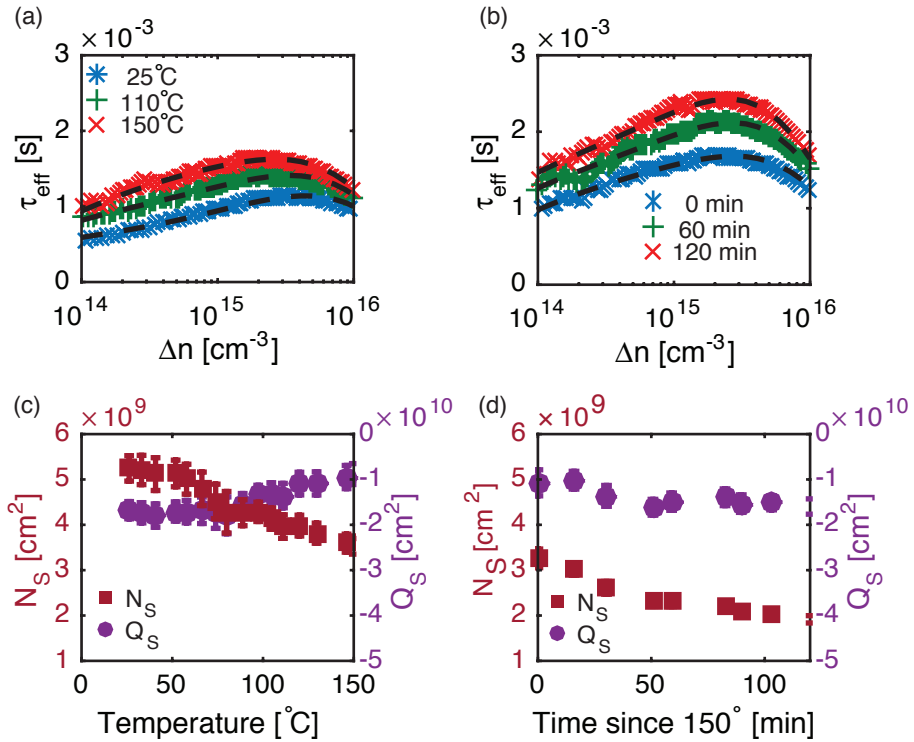


Figure 3.2: Annealing experiment on a c-Si wafer passivated with undiluted a-Si:H. (a) Carrier injection dependent lifetime of the sample at three different temperatures. Black dashed lines represent the model that was fit to the measurements, which are represented by colored markers. (b) Carrier injection dependent lifetime of the sample at three different annealing times once temperature has stabilized to 150 °C. Black dashed lines represent the model that was fit to the measurements, which are represented by colored markers. (c) Fitting results of parameters N_S (left axis) and Q_S (right axis) at different temperatures. (d) Fitting results of parameters N_S (left axis) and Q_S (right axis) at different annealing times.

150 °C, while a small decrease in N_S is apparent during the two hour annealing process.

These results illustrate the potential of using the temperature model given in Section 3.3 in conjunction with annealing experiments. The model helps to distinguish between changes in τ_{eff} that are due to changes in passivation quality and charge buildup from changes in τ_{eff} that are due to changes in the properties of Si at elevated temperatures. The results from the experiments presented in Figure 3.2, 3.3 and 3.4 show that the τ_{eff} kinetics of a-Si:H passivated samples are not universal. Further experimentation using this model can help to better understand the nature of these annealing kinetics and any potential effects they

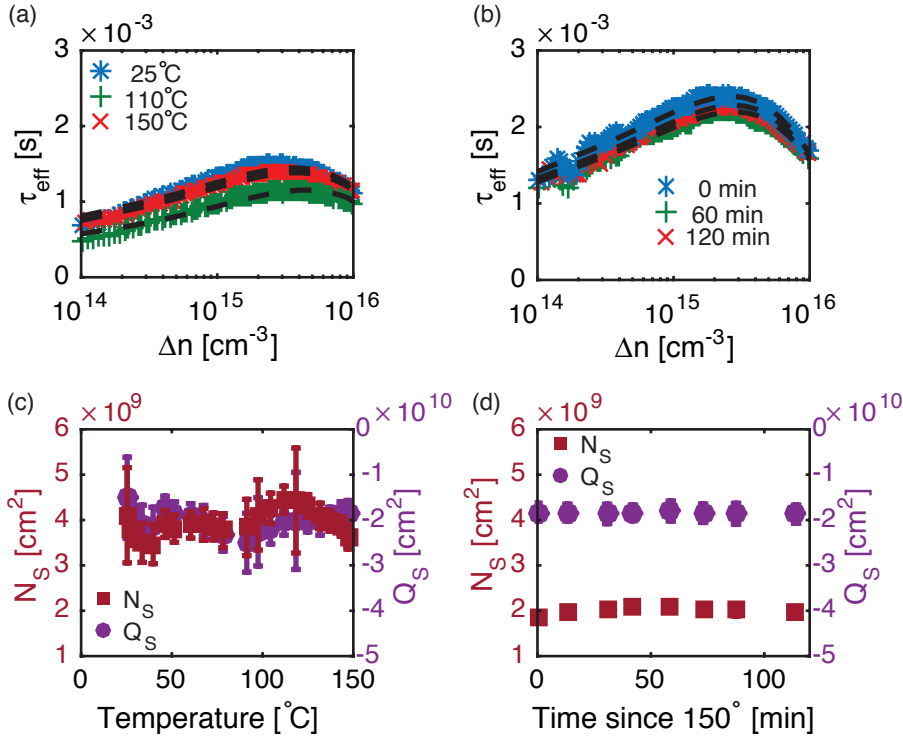


Figure 3.3: Repetition of annealing experiment on a c-Si wafer passivated with undiluted a-Si:H as shown in Figure 2. (a) Carrier injection dependent lifetime of the sample at three different temperatures. Black dashed lines represent the model that was fit to the measurements, which are represented by colored markers. (b) Carrier injection dependent lifetime of the sample at three different annealing times once temperature has stabilized to 150 °C. Black dashed lines represent the model that was fit to the measurements, which are represented by colored markers. (c) Fitting results of parameters N_S (left axis) and Q_S (right axis) at different temperatures. (d) Fitting results of parameters N_S (left axis) and Q_S (right axis) at different annealing times.

have on silicon heterojunction solar cell performance.

3.4.3 Comparison of Temperature Dependent Model to Room Temperature Model

To illustrate the utility of the temperature dependent model described in this chapter, a comparison was done on the three experiments outlined above. Figure 3.5 shows how the outputs of the model (N_S and Q_S) vary when using the temperature dependent model and when temperature is ignored.

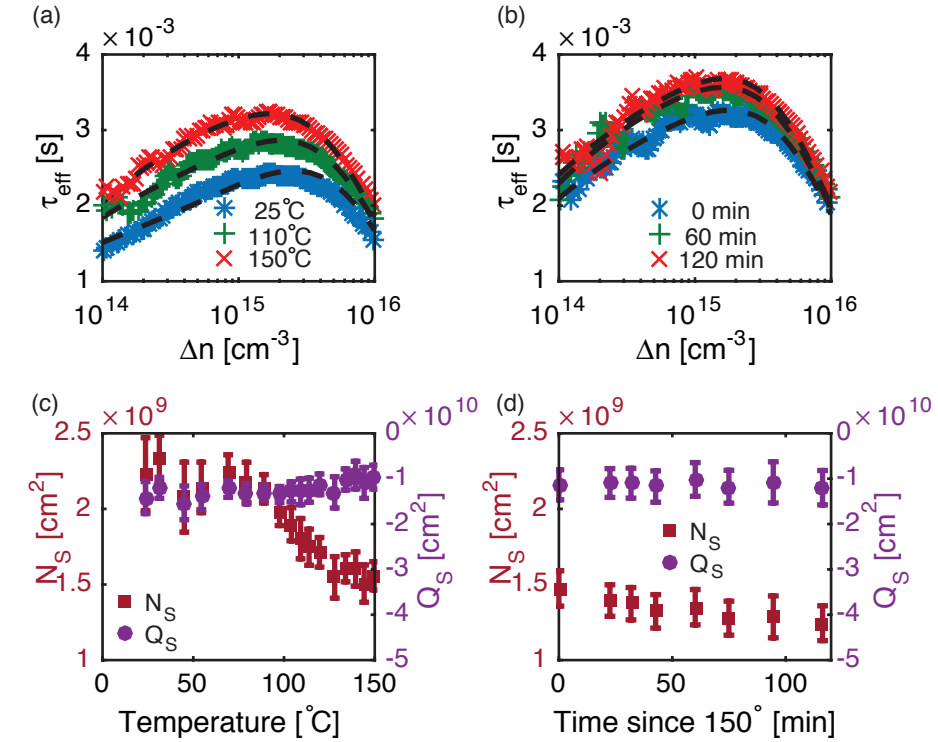


Figure 3.4: Annealing experiment on a c-Si wafer passivated with diluted a-Si:H. (a) Carrier injection dependent lifetime of the sample at three different temperatures. Black dashed lines represent the model that was fit to the measurements, which are represented by colored markers. (b) Carrier injection dependent lifetime of the sample at three different annealing times once temperature has stabilized to 150 °C. Black dashed lines represent the model that was fit to the measurements, which are represented by colored markers. (c) Fitting results of parameters N_S (left axis) and Q_S (right axis) at different temperatures. (d) Fitting results of parameters N_S (left axis) and Q_S (right axis) at different annealing times.

Figure 3.5a shows that in both the diluted a-Si:H and the undiluted a-Si:H, the τ_{eff} model is significantly temperature dependent when trying to calculate N_S from the τ_{eff} at temperatures above 100 °C as calculations of N_S from either model are outside of the error margin of the calculation of the other model. This continues with the annealing experiment at 150 °C in Figure 3.5b. In contrast, Figures 3.5c and d show that Q_S stays within the error margins when fitting using the either the temperature dependent model or the room temperature model.

The differences in N_S are more pronounced at higher defect densities. This is shown in Figures 3.5a and b when comparing the undiluted case (higher N_S) to the diluted case. In the undiluted case, there is a larger difference between using

the temperature dependent model and the room temperature model. Looking closer at the results in Figure 3.5b also confirms this. As the N_S value reduces due to annealing, the calculated values of the models get closer together and thus the effect of temperature becomes negligible.

These results suggest that if calculating N_S from a τ_{eff} measurement is the primary objective then it is useful to use this temperature correction if the sample is elevated to over 100 °C. However, if Q_S is all that is needed, using the temperature correction here will not yield a significant difference.

3.5 Conclusions

This chapter has shown how the models of Richter[68] and Olibet[67] can be modified in order to account for temperature to calculate back the passivation quality from measured τ_{eff} values. Properties of Si such as the carrier concentration, thermal velocity and Fermi level are all temperature dependent and these values affect the calculation of τ_{eff} as a function of N_S , Q_S and σ ratios. The effect of temperature on the calculation given constant passivation quality values has been demonstrated. Furthermore sample in-situ annealing experiments have been carried out to show that different types of a-Si:H can exhibit different annealing kinetics that are only apparent by using a temperature dependent lifetime model. Finally a comparison of using the temperature dependent model and the room temperature model given in literature has been carried out. This showed that correcting for temperature was significant when calculating N_S over 100 °C, but not significant when calculating Q_S up to 150 °C. This tool can now be used in further experimentation to better understand the nature of annealing induced improvements in passivation quality of c-Si by a-Si:H.

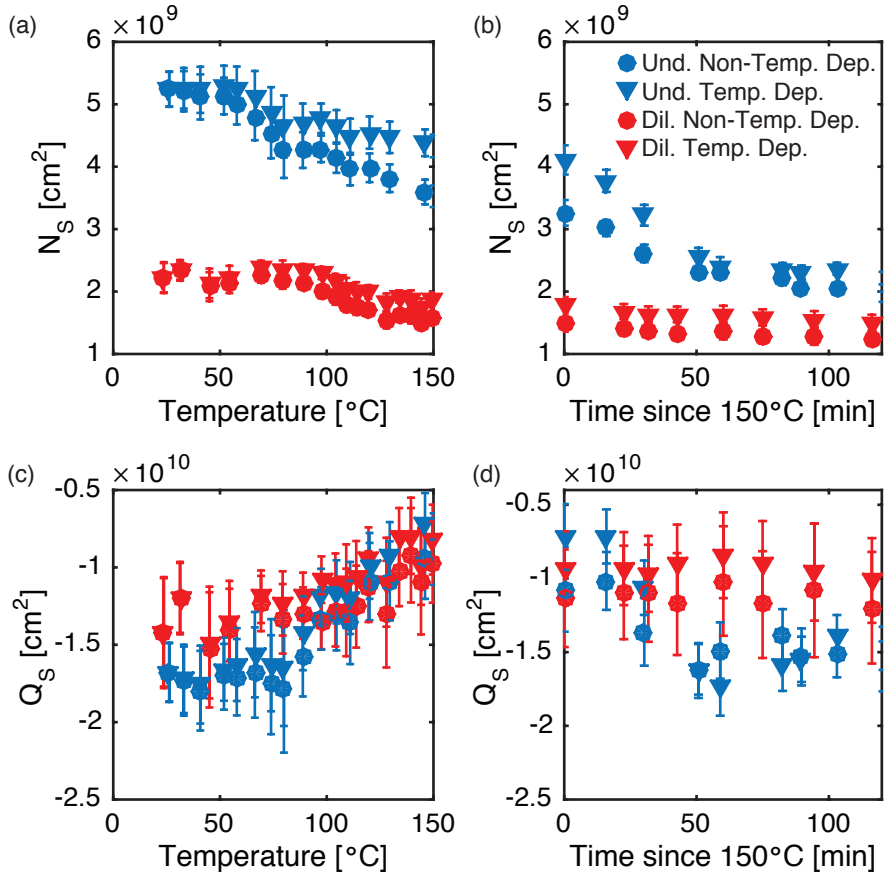


Figure 3.5: Comparison of temperature dependent model to using the room temperature model. In all figures the blue markers correspond to fittings done on data from Figure 3.2 (undiluted a-Si:H) and red markers correspond to fittings done on data from Figure 3.4 (diluted a-Si:H). Triangles correspond to fittings done using the temperature dependent model and circles correspond to fittings using the standard room temperature model. (a) Defect density vs Temperature during the temperature ramp up from room temperature to 150 °C. (b) Defect density vs annealing time at 150 °C. (c) Charge density vs Temperature during the temperature ramp up from room temperature to 150 °C. (d) Charge density vs annealing time at 150 °C.

4

Light-Induced Effects on a-Si:H/c-Si Passivation

This chapter is part of a publication submitted to the Journal of Photovoltaics

Abstract

This work investigates the properties of the amorphous silicon/crystalline silicon heterojunction interface by monitoring the passivation quality when samples are exposed to light. The results show that crystalline silicon wafers passivated with hydrogenated amorphous silicon may exhibit, not only light induced degradation of passivation quality, but also light induced improvements. In the case of p-type wafers, this light induced improvement is linked to oxide left over before amorphous silicon deposition. In the case of n-type wafers it is linked to voids in the microstructure of the amorphous silicon layer.

4.1 Introduction

Silicon heterojunction (SHJ) solar cell technology currently holds the world record for silicon based photovoltaic energy conversion. Panasonic has achieved a record efficiency of 25.6 % with their Heterojunction with Intrinsic Thin film (HIT) solar cell using an interdigitated back contacted design. [10] The fundamental structure of this technology is a crystalline silicon (c-Si) wafer that is passivated on both sides with intrinsic hydrogenated amorphous silicon (a-Si:H). Doped a-Si:H films are deposited on either side of the a-Si:H/c-Si/a-Si:H stack to form the emitter and back surface field. Though this structure produces high quality solar cells, physical understanding of the a-Si:H/c-Si interface still presents challenges. This can be shown by the complex models that are used to attempt to describe the current transport methods through the c-Si/a-Si:H interface. [78, 79] One area of this physical understanding is in the defects at the c-Si/a-Si:H interface.

The bulk absorber of SHJ solar cells is a c-Si wafer that is grown through the float-zone (FZ) or Czochralski (CZ) method. In the case of c-Si, defects have been very well studied and described in the past. [17] Light induced degradation (LID) does occur in crystalline silicon absorbers, but this is typically only with p-type wafers with boron-oxygen interstitial defects. [31] While the bulk of c-Si has a well defined crystalline lattice, dangling bonds (DBs) at the surface increase the surface recombination velocity and need to be passivated prior to adding the doped layers necessary to form the p-n junction and back surface field for solar cell operation. [80] This is typically done with intrinsic a-Si:H as it has fewer defects than doped a-Si:H. Adding a thin layer of a-Si:H, therefore, results in a lower surface recombination velocity and thus, a higher open-circuit voltage (V_{OC}) for a working SHJ device. [66]

The a-Si:H, used for passivation, is a disordered material with defect densities of 10^{16} - 10^{19} cm⁻³. [28] The defects can consist of contamination defects, DBs and vacancy defects among others. [29] Some defects in a-Si:H have been described as metastable, meaning that they are susceptible to the so-called Staebler-Wronski effect (SWE). [32] Defect densities in a-Si:H are increased through LID, but can decrease again through annealing. Various models have been applied to explain the SWE, however there is still no consensus on the fundamental mechanisms at hand. [7, 29, 81] One theory is that DBs become unpassivated during light soaking, though more recent research has shown that the nanostructure of the a-Si:H plays a role as well. [81, 82] The a-Si:H/c-Si interface is affected by the surface properties of the c-Si as well as the quality of the passivating a-Si:H layer. [19]

One established way to monitor the quality of a-Si:H passivation of c-Si wafers is to use photoconductance decay (PCD) lifetime measurements. This method probes the interface by measuring the effective minority carrier lifetime (τ_{eff}) in a c-Si wafer or full device. [66] Since the recombination is dominated by the surface, the measurement can be directly related to the quality of the a-Si:H/c-Si interface. [83] In general, higher lifetimes measured in this way suggest a better

quality interface and a device with a higher open circuit voltage (V_{OC}). [84]

Utilizing this method, work has been done to observe the degradation of the τ_{eff} upon light soaking. De Wolf et al. has shown that through light soaking, τ_{eff} does change. [42, 43] This change in τ_{eff} has been linked strictly to DB generation using a model on the amphoteric nature of dangling bonds in SHJs. [44] Furthermore, experiments have shown that wafers with $\langle 111 \rangle$ orientation are not susceptible to this light-induced degradation, while wafers with $\langle 100 \rangle$ orientation are. [43] The process has been shown to be partially reversible through annealing. [45] Mahtani et al. has shown that there can also be light-induced improvement in τ_{eff} . [48] In this paper the light-induced improvement was linked solely to the initial τ_{eff} (τ_{eff}^0) where samples with a low τ_{eff}^0 exhibit light-induced improvement and samples with a high τ_{eff}^0 exhibit LID. The measurement procedure used in these studies is described in this manuscript as multiple exposure photoconductance decay (MEPCD). In these measurements, hundreds to thousands of PCD measurements are taken in order to study the change in τ_{eff} , and thus the change in a-Si:H/c-Si interface passivation quality over upon light exposure from the PCD measurement flashes.

The study of the metastability of the a-Si:H/c-Si interface passivation quality is studied further here by expanding the deposition parameters of the a-Si:H and the preparation steps of the c-Si wafers. Though changes in passivation quality have been previously attributed solely to DB density increases at the a-Si:H/c-Si interface, results here show that this is not always the case. By changing the light soaking parameters, wafer type, cleaning parameters and a-Si:H deposition conditions, further insight is gained regarding the mechanisms of this metastability and the implications on SHJ solar cell performance. Results here show that simple generation of DBs at the interface is not sufficient to explain the changes that are observed and that other factors such as fixed charge can play a significant role depending on which set of sample parameters are used. Furthermore, the results presented here provide further insight into the mechanisms of light-induced improvement.

4.2 Experimental Details

4.2.1 Sample Preparation

The samples in this work were deposited on $\sim 280 \mu\text{m}$ thick, $\sim 4.0 \text{ cm}$, double polished, FZ c-Si wafers. Both phosphorus-doped (n-type) and boron-doped (p-type) wafers were used. The cleaning procedure consisted of 10 minutes of 99 % HNO_3 at room temperature followed by 10 minutes of 69 % HNO_3 at 105°C to encapsulate organic contaminants in an oxide layer. After this, the oxide was stripped away by a dip in a solution of 0.55 % HF for a variable amount of time. The a-Si:H layers were deposited by radio frequency (RF) plasma enhanced chemical vapor deposition (PECVD) at 13.56 MHz. The depositions were carried out

at a substrate temperature of 180 °C unless otherwise specified. Thicknesses were kept between 30 nm to 65 nm and these thicknesses were verified using spectroscopic ellipsometry (SE). A schematic of the sample structure is given in Figure 4.1b.

The a-Si:H films were deposited using two sets of deposition conditions. The first set of conditions, referred to here as undiluted, was deposited at 0.7 mbar, 40 sccm SiH₄ and at a power density of 0.015 W cm⁻². The second set of conditions, referred to here as diluted, was deposited at 8 mbar, 4 sccm SiH₄, 200 sccm H₂ and at a power density of 0.056 W cm⁻². This second set of high-diluted material has been known to produce thin film solar cells with a high V_{OC} and provides good passivation for SHJ solar cells. [35, 47, 85] In all cases, the samples were annealed at 130 °C to 150 °C for 30 min to 2 h in a furnace after the a-Si:H deposition before measurements were carried out.

4.2.2 Lifetime Measurements

Lifetime measurements were carried out using a Sinton WTC-120 PCD setup. This setup uses a light flash that is filtered to only allow red/infrared light to pass through. The setup is fitted with an external light soaking light emitting diode (LED) as shown in Figure 4.1a. The spectra for both the light soaking LED and the measurement flash, are given in Figure 4.1c. These spectra were measured using an AVANTES Dual AvaSpec 2048. It should be noted that amplitude of the measurement flash spectra was extrapolated, as the measurement flash is much shorter than the minimum integration time of the measurement. The lifetime measurements at an excess charge carrier density of 10¹⁵ charge carriers cm⁻³ is used here.

Figure 4.1d shows the generation profile of the top a-Si:H layer and the c-Si bulk layer under illumination from both light sources. There is also a rear layer of a-Si:H, which is not represented in the figure because the vast majority of the light, in either case, is absorbed before it reaches this layer and thus the absorption there is negligible. These generation profiles were calculated using the Advanced Semiconductor Analysis (ASA) software developed by the Delft University of Technology's Photovoltaic Materials and Devices (PVMD) group. [86] The optical properties of both a-Si:H and c-Si were obtained using SE.

4.2.3 Fourier Transform Infrared Spectroscopy

Fourier Transform Infrared Spectroscopy (FTIR) was used to characterize a-Si:H films. In these cases, the same deposition conditions that were used to make a sample for MEPCD measurements were used to deposit a 100 nm thick a-Si:H layer on top of a CZ, single side polished wafer. FTIR measurements were carried out using a Thermo Fisher Nicolet 5700 FTIR spectrometer in transmittance mode.

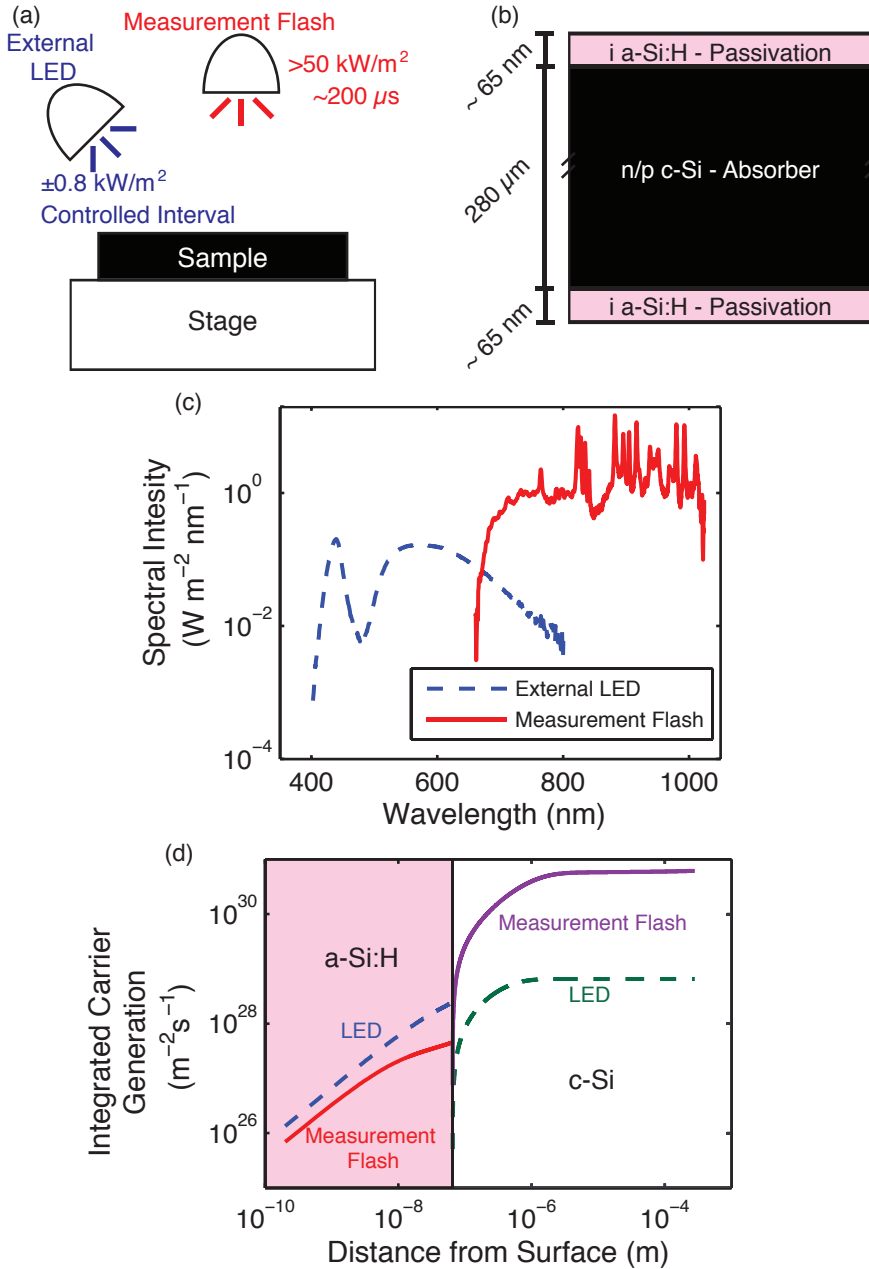


Figure 4.1: Experimental details of this work. (a) Diagram of experimental setup: Sinton WTC-120 and External LED, (b) sample preparation, (c) light spectrum of flash of Sinton PCD lifetime tester and the external LED from the experimental setup, and (d) cumulative generation profile of samples. The generation profile has been integrated to show how many charge carriers per cm^2 are generated in the a-Si:H film and the c-Si wafer.

Prior to fitting the FTIR measurements, the background is corrected by removing a third order polynomial. The fitting used is a deconvolution of the FTIR response into two Gaussian curves. The curve in the range of 1995-2005 cm^{-1} is known as the low-stretching mode (LSM) while the curve with a peak in the range of 2080-2090 cm^{-1} is known as the high stretching mode (HSM). [87] Responses in the LSM correspond to hydrogen which is incorporated into small volume deficiencies such as divacancies and is therefore assigned to monohydrides. [88]. The HSM, on the other hand can be attributed both to monohydrides and higher dihydrides on inner surface voids in a clustered form. [30, 45] In this work, monohydrides are assumed to contribute to the LSM while clustered monohydrides on the inner-void surface are assumed to contribute to the HSM. Though dihydrides also contribute to the HSM, this contribution is minimal as the monohydrides on the inner surface are much more dominant. [29]

Information about the microstructure of the a-Si:H films used for passivation can be extracted from FTIR measurements using the assumed contributions to the LSM and HSM given above. This can be done using the microstructure parameter R^* as:

$$R^* = \frac{I_{\text{HSM}}}{I_{\text{HSM}} + I_{\text{LSM}}} \quad (4.1)$$

where I_{HSM} and I_{LSM} are the peak integrals of the HSM and LSM respectively. [35, 85] In general, a higher R^* parameter corresponds to a film with a higher void density, or a more porous film.

In addition to this the atomic percentage of hydrogen (C_{H}) was calculated by using the wagging mode of at 640 cm^{-1} . The peak at 640 cm^{-1} was integrated and multiplied by the conversion factor of 1.6×10^{19} . [29]

4.3 Results and Discussion

The results of the light soaking experiments performed on both n-type and p-type wafers are given here. In both cases, external light soaking was used to monitor effects of different illumination times.

This is followed by measurements done utilizing only the measurement flash of the PCD lifetime tester of n-type wafers where further information can be gathered about the evolution of τ_{eff} . Here, the generation is dominated by the c-Si wafer and annealing effects of long periods of light exposure are minimized. The deposition temperature of the a-Si:H is varied to ascertain further insights into the nature of the observed.

Finally MEPCD measurements are carried out on wafers passivated with diluted a-Si:H. These samples exhibit higher initial lifetimes and are more representative of the a-Si:H/c-Si interfaces used in state of the art SHJ devices.

4.3.1 Light Soaking Experiments

Figure 4.2 shows the evolution of τ_{eff} utilizing the external light soaking LED on a sample consisting of an n-type $\langle 100 \rangle$ wafer passivated by undiluted a-Si:H. Here, as with all MEPCD measurements presented in this chapter, the relative τ_{eff} ($\tau_{\text{eff}} / \tau_{\text{eff}}^0$) is plotted while the initial τ_{eff} (τ_{eff}^0) is also provided. τ_{eff}^0 is defined here as the first τ_{eff} measured immediately after annealing. These samples were annealed at 130 °C for 30 min and repeatedly measured the samples until no abrupt changes were observed in τ_{eff} (45 flashes were used in this experiment). These measurements are shown in the ‘Dark’ portion of the figure. At this point light soaking steps were implemented from 10 μs up to 1000 s and the samples were measured with 5 flashes after each light soaking step and the average τ_{eff} over those 5 flashes is plotted here.

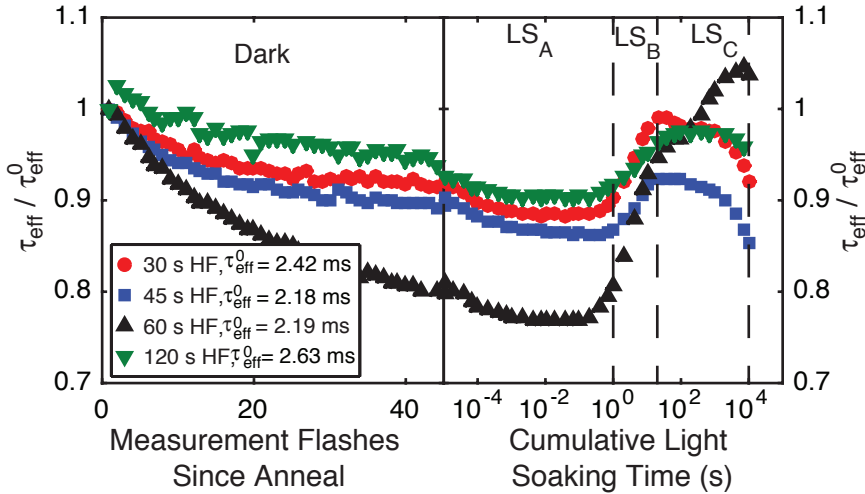


Figure 4.2: MEPCD measurement with external light soaking on an n-type $\langle 100 \rangle$ wafer passivated with undiluted a-Si:H. HF dip times were varied. Initial lifetimes (τ_{eff}^0) are given in the figure.

The final cleaning step, the HF dip, was varied in these samples. The τ_{eff} decays further in the LS_A period depending on how long the sample was dipped. The one anomaly in this experiment is the sample that was dipped for 120 s, which decays less than other samples in the series. Overall, however, the shape of the kinetics remained fairly constant for these samples all had the same general trend of a decrease in τ_{eff} followed by an increase in τ_{eff} .

During the ‘Dark’ phase of the experiment, a continuous decay of lifetime was observed. Upon external light soaking, 3 regimes were noticed and labeled here as LS_A , LS_B and LS_C . During the LS_A phase, a continuous decay of τ_{eff} is noted.

This is followed by an increase in τ_{eff} during the LS_B phase and a decrease in the LS_C phase. It should be noted that these changes in τ_{eff} are metastable, i.e. if the sample is annealed and measured again, similar kinetics in τ_{eff} evolution are shown.

Other experiments have explained the τ_{eff} kinetics by an increase of the DB density at the a-Si:H interface. [43] However, if this were the case, there would be a continuous decay in τ_{eff} due to light soaking. These results, therefore, show that an increase in DB density at the interface cannot be the only physical explanation for changes in τ_{eff} due to light soaking.

There may be, however, multiple explanations for the increase in τ_{eff} in the LS_B and LS_C regions. The light soaking at large steps could also be heating the sample and having an annealing effect, which could decrease the defect density at the a-Si:H/c-Si interface, thereby increasing the τ_{eff} . Additionally, the external light soaking causes generation in both the a-Si:H as well as the c-Si bulk in relatively equal amounts as shown in Figure 4.1d.

Figure 4.3 shows a similar light soaking experiment as was shown in Figure 4.2 using p-type wafers instead of n-type wafers. These measurements show that when a p-type wafer is used, the kinetics may be the opposite of that found on samples using n-type wafers when the p-type wafers were cleaned with HF dip times of 15 to 30 s before a-Si:H deposition. At higher HF dip times the kinetics in the LS_A period follow that of the n-type samples. The samples prepared with lower HF dip times exhibited less hydrophobicity than those of higher HF dip times implying that the native oxide may not have been entirely removed prior to a-Si:H deposition.

This suggests that when using p-type wafers, the cleaning procedure can have a major impact on the τ_{eff} kinetics. One possible, explanation, may be that this reversal of kinetics is caused by a native oxide layer causing a light-induced negative fixed charge at the a-Si:H/c-Si interface. This negative fixed charge build up would help to repel the minority charge carriers (electrons) from the surface to the higher lifetime bulk p-type c-Si thus increasing the τ_{eff} . This would explain why these results are not present when n-type samples are used as a build up of negative charge would only further decrease the τ_{eff} when the minority charge carrier is a hole. However, this remnant oxide would be between the a-Si:H and the c-Si and therefore extremely hard to measure. Further investigation would be necessary to ascertain whether the native oxide explanation is valid.

4.3.2 Measurement Flashes Only

To determine whether light-induced improvements at long light exposure times occur without the possible annealing effect, measurements were carried out on n-type, $\langle 111 \rangle$ wafers to also observe whether or not light induced degradation and improvement of τ_{eff} is present there. Figure 4.4 shows an MEPCD measurement done with no external light soaking on such a sample. Though there is no external light soaking, light induced τ_{eff} does start to occur after 100 measurement flashes.

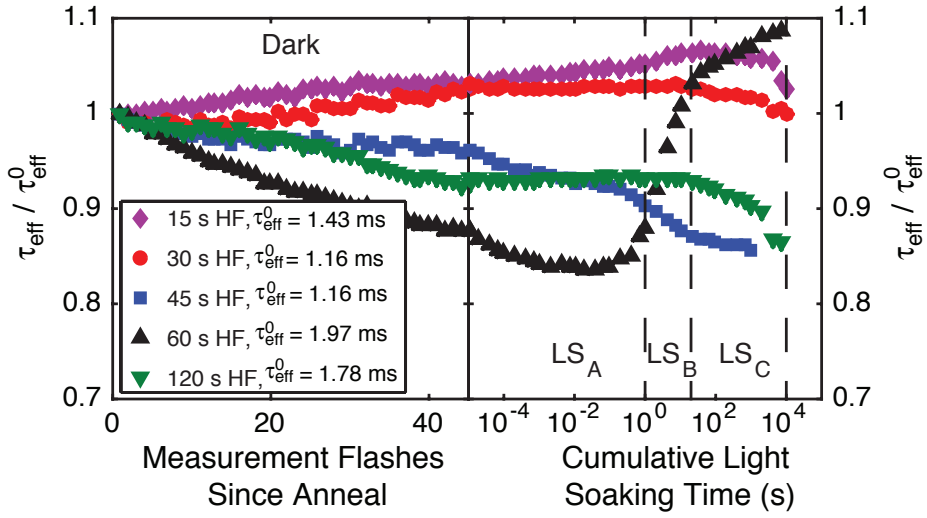


Figure 4.3: MEPCD measurement with external light soaking on a p-type $\langle 100 \rangle$ wafer passivated with undiluted a-Si:H. HF dip times were varied.

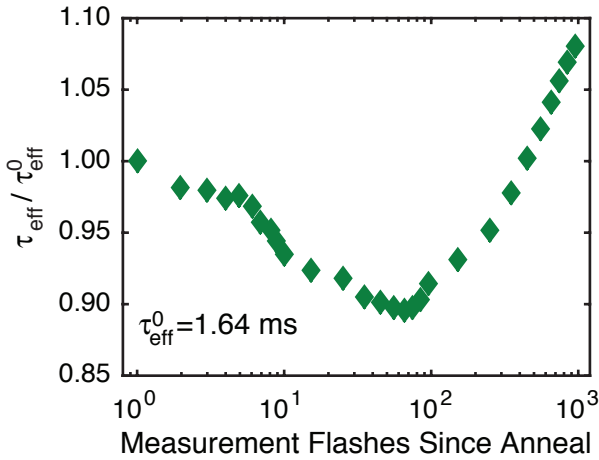


Figure 4.4: MEPCD measurement on an n-type $\langle 111 \rangle$ wafer passivated by undiluted a-Si:H. No external light soaking is used here.

This measurement presents two important findings. Firstly that, contrary to what was observed by De Wolf et al. samples prepared here on n-type $\langle 111 \rangle$ wafers can, indeed, exhibit significant kinetics upon light soaking. [43] Further-

Table 4.1: Peak position (ω) and peak integral (I) of low stretching mode (LSM) and high stretching mode (HSM) of FTIR curves from Figure 4.5a at different deposition temperatures (T_{dep}). R^* is the microstructure parameter from Equation 4.1. C_H is the atomic percentage of hydrogen calculated from the wagging mode.

T_{dep} [°C]	ω_{LSM} [cm ⁻¹]	I_{LSM}	ω_{HSM} [cm ⁻¹]	I_{HSM}	R^*	C_H at. %
100	2005	93.63	2077	57.33	0.38	13.1
140	2001	60.14	2079	19.78	0.28	9.0
160	1999	147.54	2081	19.05	0.11	11.5
180	1996	73.66	2081	6.11	0.08	6.6
220	1994	131.62	-	0.00	0.00	7.2

more, this result shows that light induced improvement occurs without long light exposure and higher energy photons (see Figure 4.1c and d) implying that this is not due to an annealing process. In order to investigate the cause of light induced improvement in τ_{eff} , variations on the deposition temperature of the a-Si:H film were carried out.

Changes in the deposition temperature of the passivating a-Si:H film are investigated here. Deposition temperature was chosen as a varying parameter because it is known to affect the microstructure of a-Si:H. [29] The microstructure of the a-Si:H films are measured using FTIR as shown in Figure 4.5a.

The R^* parameter, as determined by Equation 4.1 along with the peak position of the high and low stretching modes (ω_{HSM} and ω_{LSM}) are calculated from the FTIR measurements in Figure 4.5a and are all given in Table 4.1.

Passivation using these deposition conditions were carried out on n-type $\langle 111 \rangle$ wafers. Before looking at the kinetics and how the lifetime evolves due to measurement flashing, the initial lifetimes are observed. Figure 4.5b shows how the as deposited lifetime varies with deposition temperature as well as how R^* varies with deposition temperature. A clear trend is shown here that more porous materials provided poorer passivation. This is in agreement with other studies who have shown that voids in a-Si:H films show them to be poor passivation materials. [19]

These samples were annealed at 150 °C for 2 h and then flashed 1000 times in the dark. The results of this experiment are shown in Figure 4.6. These results can be split into three regimes where the samples prepared at 100 °C and 140 °C exhibit lifetime kinetics that are dominated by light induced increases in τ_{eff} , the sample prepared at 220 °C exhibits lifetime kinetics that are dominated by light induced decreases in τ_{eff} and the samples prepared at 160 °C and 180 °C exhibit lifetime kinetics with a light induced decrease followed by a light induced increase in τ_{eff} .

These kinetic regimes can be linked to the R^* parameter of the a-Si:H films as shown in Figure 4.5b. The C_H of the films is also provided in Table 4.1. The

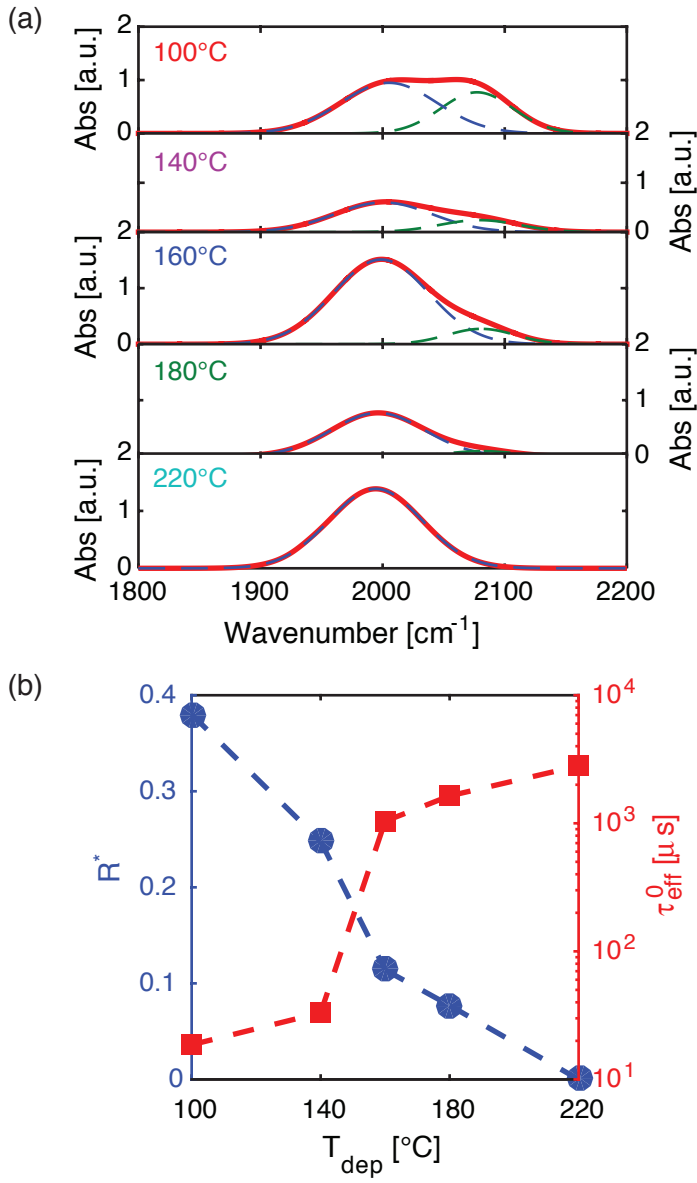


Figure 4.5: (a) FTIR measurements on c-Si/a-Si:H interface where a-Si:H was deposited at different deposition temperatures (T_{dep}). Substrate temperature was varied from 100 °C to 200 °C. (b) R^* parameter calculated from FTIR measurements as well as initial lifetime (τ_{eff}^0) vs deposition temperature.

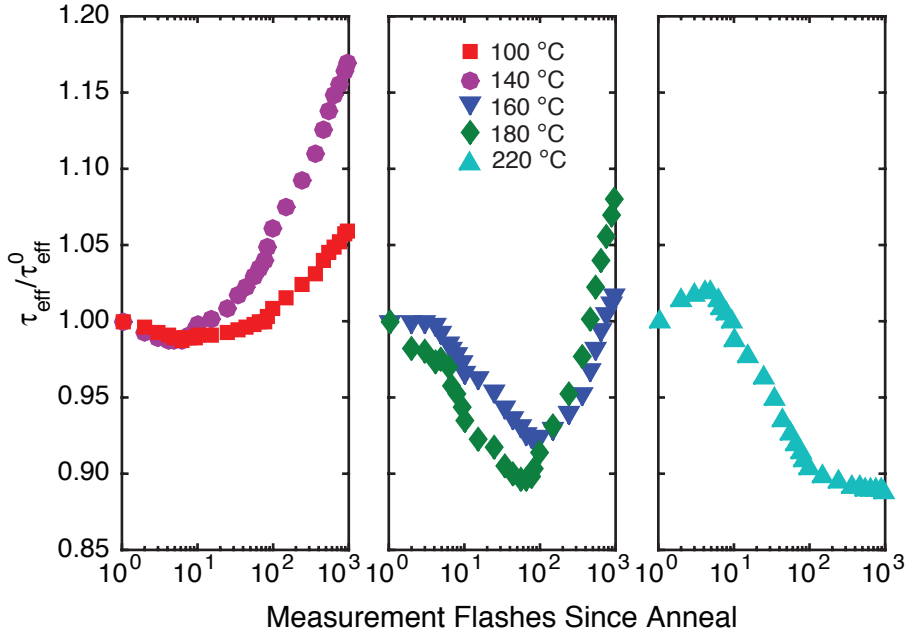


Figure 4.6: MEPCD measurements on samples with different temperatures. Three panels with different kinetic regime are shown. Leftmost corresponds to samples with $R^* > 0.25$, center corresponds to samples with $0 < R^* < 0.25$, rightmost corresponds to a sample where $R^* \approx 0$.

values here change between 7.2 % and 13.1 % but do not correlate with kinetics. As nothing else was varied in the deposition parameters, this suggests that the microstructure of the passivating a-Si:H film plays a role in the measurement flash kinetics of the τ_{eff} . The results show that wafers passivated with a-Si:H films with an R^* of more than 0.25, light flashes tend to increase the lifetime. These films are more porous than ones with a lower R^* . In wafers passivated by a-Si:H films with an R^* of 0, which are dominated by smaller volume deficiency defects such as vacancy defects, the τ_{eff} primarily degrades. Finally when wafers are passivated with medium dense films with an R^* above 0 but less than 0.25, the kinetics the τ_{eff} decreases followed by an increase after around 100 flashes. In these films there are a detectable amount of voids in the films but significantly less than those in the more porous regime.

This suggests that a possible explanation for the light induced increase in τ_{eff} observed on samples using n-type wafers comes from voids in the passivating a-Si:H films, while the degradation is linked to vacancies in the films. The decay in τ_{eff} can be explained, as has been in literature, by DB formation at the a-Si:H/c-Si interface. This would imply that the quality of chemical passivation is decreased.

[43] Though the exact mechanism of the increase in τ_{eff} cannot be fully explained by the results here, one possible explanation is that there is a positive charge build up at the interface. As charge carriers enter the a-Si:H film, defects at the void surface may charge positively and this build up of charge would repel the minority charge carriers of the n-type c-Si wafer (holes) from the interface back into the high lifetime bulk of the n-type c-Si wafer. This would, in essence, increase the lifetime of generated holes in the interface. This effect implies that the light induced changes affect the field-effect passivation of the samples. To investigate this further, similar experiments were performed using p-type wafers.

To explain the mechanism behind the effect of void charging a band diagram of the a-Si:H/n-type c-Si interface is given in Figure 4.7. This charging could occur because of the inversion layer where the band bending in the n-type c-Si will cause holes to drift towards that interface. This is combined with a barrier caused by the valence band offset between the a-Si:H and the c-Si. This could result in a build up of holes at the interface which would cause a positive charging effect at that interface. This is explored further in Chapter 5.

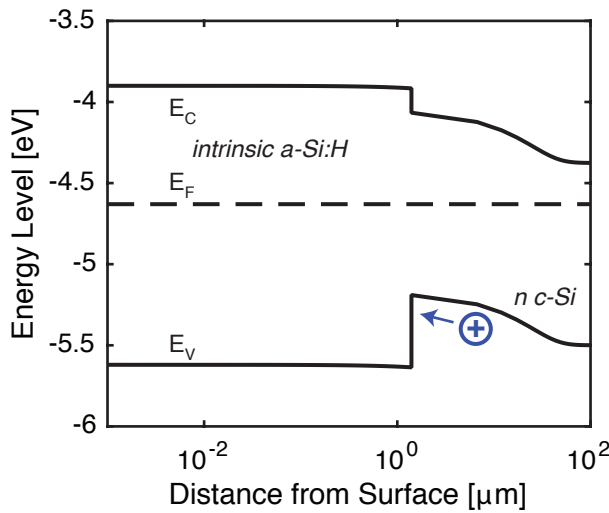


Figure 4.7: Band diagram of the c-Si/a-Si:H interface using n-type c-Si and intrinsic a-Si:H. Bands were calculated using the modeling software, AFORS-HET. Hole pictured at the left of the c-Si to show the capability of trapping at the interface.

4.3.3 Diluted a-Si:H Study

Experiments above were all done using undiluted a-Si:H. However, recent results have shown that diluted a-Si:H can achieve better passivation quality. [47] This material is characterized by being similarly dense as the films deposited at 180 °C

and 160 °C in the experiments in Figure 4.5 while having a higher density of hydrogen (15 % to 20 %). [35] MEPCD measurements were carried out on samples prepared in this way. Figure 4.8 shows MEPCD measurements on n-type wafers of both $\langle 111 \rangle$ and $\langle 100 \rangle$ orientations. Though τ_{eff} values here are higher than those presented with diluted films, the kinetics of the changes to the τ_{eff} are similar exhibiting both light induced degradation and light induced improvement.

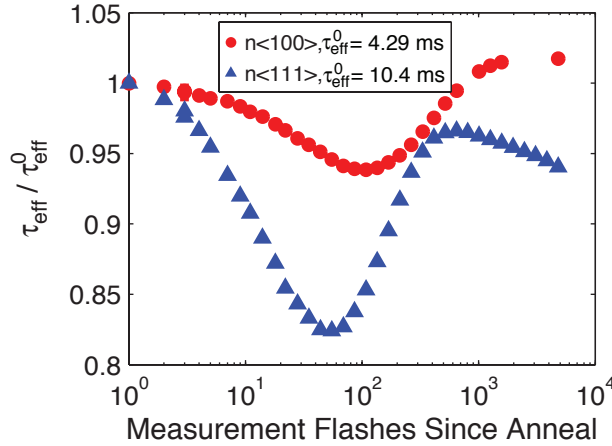


Figure 4.8: MEPCD measurements on different wafer orientations passivated with highly diluted a-Si:H.

Figure 4.9 shows similar measurements on p-type $\langle 100 \rangle$ samples. Here, diluted films were used for passivation as well. Just as with the light soaking experiments in Figure 4.3, low HF dip times result in a slight light induced improvement of τ_{eff} , while higher HF dip times result in samples that exhibit light induced degradation of τ_{eff} . It should be noted that when similar experiments were carried out with n-type wafers, no notable reversal of kinetics was shown with low HF dip times.

4.4 Conclusions

This manuscript has shown an investigation of the light induced degradation and increase of the τ_{eff} of c-Si wafers passivated with a-Si:H. These wafers are prepared with a similar procedure as they would be for use in a full SHJ device. It has been shown that in the case of n-type wafers, light soaking tends to decrease the τ_{eff} when the passivating film is dense and tends to increase the τ_{eff} when the passivating film is porous. In the case of p-type wafers minority charge carrier lifetime evolution due to light soaking is dependent on the cleaning procedure

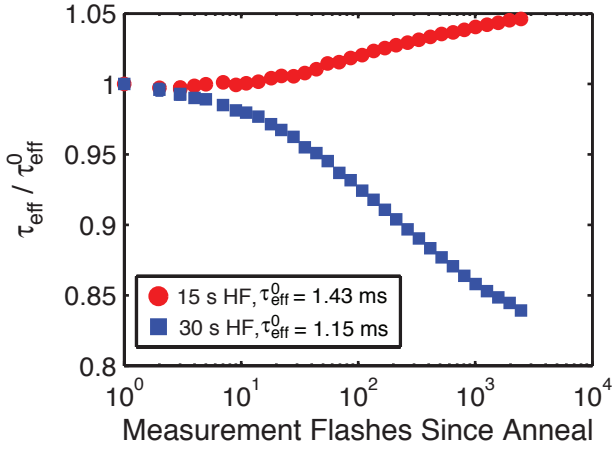


Figure 4.9: MEPCD measurements on p-type wafers passivated with diluted a-Si:H. HF dip times were varied.

used where low HF dip times can result in a slight light induced improvement in τ_{eff} . Both of these results suggest that DB formation at the c-Si/a-Si:H interface is not the only factor at play and a build up of positive charge, in the case of porous films passivating n-type wafers, and a build up of negative charge, in the case of p-type wafers prepared with a low HF dip time may also play a role in these kinetics. This aids in better understanding the nature of the a-Si:H/c-Si interface.

5

The Effect of Doped Layers on the Light-Induced Effects of a-Si:H/c-Si Passivation

This chapter is part of a publication submitted to the Journal of Photovoltaics

Abstract

The effect of depositing doped amorphous silicon (a-Si:H) to n-type crystalline silicon (c-Si) wafers passivated with intrinsic a-Si:H is investigated. This is studied by monitoring the effective lifetime as it changes with light exposure. Using p-type a-Si:H layers results in light induced increases in lifetime, while using n-type a-Si:H results in light induced degradation of lifetime. Furthermore, full silicon heterojunction precursors with both n-type and p-type a-Si:H are investigated and it is found that the light soaking kinetics depend on which side of the sample is flashed. Flashing on the p-type a-Si:H results in light induced enhancement of the lifetime while flashing on the n-type a-Si:H results in light induced degradation of lifetime. Though the nature of this phenomena is unclear, current explanations in literature are ruled out to better understand the complexity of light induced effects on the a-Si:H/c-Si heterostructure.

5.1 Introduction

The use of amorphous silicon (a-Si:H) as passivation layers and carrier selective layers for wafer based crystalline silicon (c-Si) photovoltaics now holds the world record for the highest silicon based solar cell technology. [10] This structure is called a silicon heterojunction (SHJ) solar cell as the emitter and back surface fields (BSF) are made up of a-Si:H, which has a bandgap between 1.6 eV and 1.8 eV, while the absorber layer is made up of a c-Si which has a bandgap of 1.1 eV. This structure is gaining in interest from a research point of view as well as gaining market share as a higher efficiency alternative to typical multi-crystalline silicon based solar cells. As a-Si:H plays a role in SHJ technology, and a-Si:H is highly susceptible to light induced degradation (LID) via the Staebler-Wronski Effect[32], research has been undertaken to understand the light induced properties on SHJ solar cells. However, the majority of the research undertaken has been on symmetrical structures of c-Si passivated with intrinsic a-Si:H. This chapter expands on this investigation by observing light induced effects on structures when doped a-Si:H layers forming the emitter and back surface field (BSF) are included.

Prior work has shown that the effective lifetime (τ_{eff}) of c-Si wafers passivated with a-Si:H are susceptible to light induced degradation. [43] This has been linked to a increase of dangling bond (DB) density at the c-Si/a-Si:H interface. However, here the thickness of the a-Si:H used was much thicker (30 nm) than the thicknesses used in actual SHJ devices (5 nm to 10 nm). Similar studies have been done in this thesis. Here it has been shown that light induced effects can also cause increases in τ_{eff} upon light exposure. This tends to happen in samples where the a-Si:H used for passivation has a higher void density. The light induced improvement of τ_{eff} is linked to charging of the voids at these surfaces thereby increasing the τ_{eff} . Though other work has also shown significant changes in τ_{eff} of these samples due to light exposure, full SHJ devices do not exhibit significant changes in performance. [41]

There are many explanations for why there is no significant change in SHJ device performance, while there is a significant change in τ_{eff} in the experiments done by De Wolf and in this thesis. One possible explanation is that thinner a-Si:H layers are used in real SHJ devices than the ones used in the other experiments. Thin film silicon solar cell research has shown that devices with thinner intrinsic a-Si:H absorber layers degrade less than those with thicker absorber layers. [33] Another explanation is that the doped layers play a role in the metastable properties of the a-Si:H/c-Si interface. This work looks at these potential explanations and investigates the metastability of samples with appropriately thin layers and with the addition of doped layers. A similar investigation has been done by Mahtahni et al. [48] Here, only the emitter (p-type a-Si:H) was explored and increases in τ_{eff} were observed. Furthermore, only long time scales were explored in the work of Mahtani, while previous work has shown that there are a lot of light induced changes on very short timescales. [43] This work uses c-Si wafers

passivated with a-Si:H using thicknesses close to what are used in real devices and uses doped layers and investigates the short time scales immediately after annealing.

5.2 Experimental Details

The samples in this work were deposited on $\sim 280\ \mu\text{m}$ thick, $\sim 4.0\ \text{cm}$, double polished, float zone, c-Si wafers. These wafers were all phosphorous doped (n-type) with $\langle 111 \rangle$ orientation with a resistivity of $\sim 5\ \Omega\text{cm}$. The cleaning procedure consisted of 10 minutes of 99% HNO_3 at room temperature followed by 10 minutes of 69% HNO_3 at $105\ ^\circ\text{C}$ to encapsulate organic contaminants in an oxide layer. After this, the oxide was stripped away by a dip in a solution of 0.55% HF for 75 seconds.

The a-Si:H layers were deposited on the c-Si wafer by radio frequency (RF) plasma enhanced chemical vapor deposition (PECVD) at 13.56 MHz. The depositions were carried out at a substrate temperature of $180\ ^\circ\text{C}$. The intrinsic a-Si:H used was deposited at 8 mbar, 4 sccm SiH_4 , 200 sccm H_2 and at a power density of $0.056\ \text{W cm}^{-2}$. The p-layer used was deposited at 0.7 mbar, 20 sccm SiH_4 and 3 sccm of B_2H_6 at a power density of $0.021\ \text{W cm}^{-2}$. The n-layer used was deposited at 0.6 mbar, 40 sccm SiH_4 and 11 sccm of PH_3 at a power density of $0.021\ \text{W cm}^{-2}$. The justification for all of these conditions are given in the thesis of Dr. Dong Zhang. [55]

The thickness of the a-Si:H layers was determined using spectroscopic ellipsometry (SE). The goal of the experiments is to view the effect of doped layers on the metastability of the τ_{eff} of the SHJ interface. As thickness may play a role in this the total a-Si:H thickness was held constant in all cases and here 14 nm was used. Therefore, on samples with just an intrinsic layer deposition, 14 nm of intrinsic a-Si:H is deposited. On samples with doped layers, 7 nm of intrinsic a-Si:H is deposited followed by 7 nm of doped a-Si:H. Schematics of all the different samples are given in Figure 5.1.

τ_{eff} measurements were carried out using photoconductance decay (PCD). These were done using a Sinton WCT-120 PCD measurement setup. All τ_{eff} values here are at an excess charge carrier density of $10^{15}\ \text{charge carriers cm}^{-3}$. After a-Si:H depositions samples were first annealed at $150\ ^\circ\text{C}$ on a hot plate in air for 120 minutes after deposition. During this time, the τ_{eff} was monitored using a Sinton WCT-120TS stage with controllable temperature. The samples were then brought to the WCT-120 measurement setup and measured 1000 times. Throughout the annealing steps and the measurements the sample was kept in darkness. The only light that the samples are exposed to throughout the experiment are those of the measurement flash. These measurements are referred to as multiple exposure photoconductance decay (MEPCD) measurements.

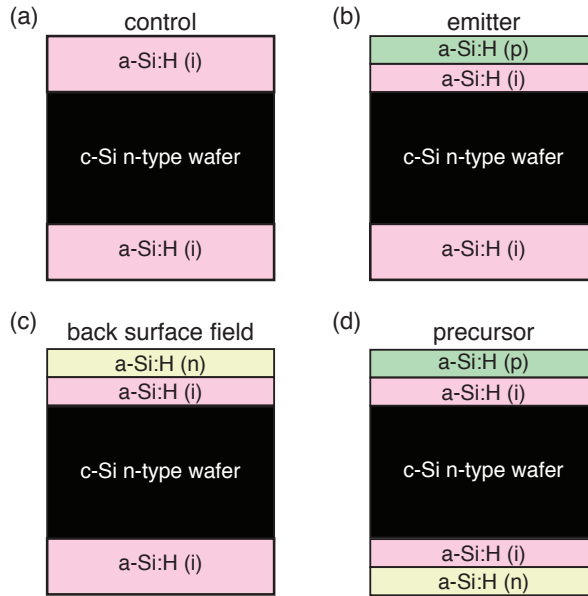


Figure 5.1: Schematics of the samples used in this work. (a) the standard sample with 14nm of passivating a-Si:H on either side of the c-Si wafer. (b) the sample with a deposited emitter on one side of the sample. (c) the sample with a deposited back surface field on one side of the sample. (d) full precursor of a SHJ solar cell with both an emitter and a back surface field.

5.3 Results and Discussion

Four distinct samples were created to undergo the process described above. These are (schematics shown in Figure 5.1) given in Table 5.1.

Figure 5.2 shows the lifetime of each of the samples changed due to annealing. In the left panel, the ramp up of temperature from room temperature to 150 °C. The right panel shows the lifetime throughout the two hour annealing process. All samples show a similar trend where the lifetime increases due to annealing temperature. The samples arrive at different relative lifetimes. There is no clear explanation for this difference in as deposited or annealed lifetimes. More runs of this procedure would be necessary to confirm that the differences are actually caused by the layer doping. However, these results do show that regardless of additional doped layers, τ_{eff} does increase upon thermal annealing after deposition.

Figure 5.3 shows the results of the experimental procedure on measurement on the control sample. Just as in Chapter 4, a signature of a decrease in τ_{eff} followed

Table 5.1: Sample descriptions and as deposited τ_{eff} values

Stack	Name	As Deposited τ_{eff} [ms]
i/c-Si/i	Control	2.3
p/i/c-Si/i	Emitter	2.2
n/i/c-Si/i	BSF	2.6
p/i/c-Si/i/n	Precursor	3.9

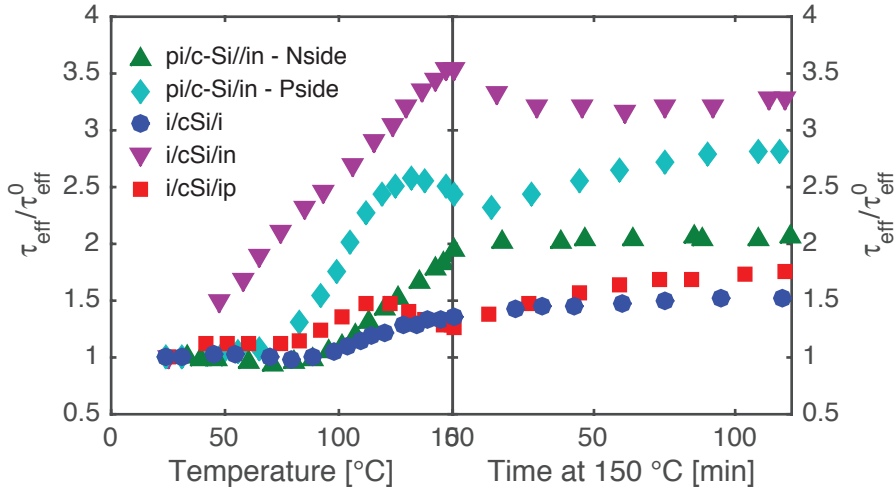


Figure 5.2: Results of annealing experiment on different sample stacks. (a) shows the relative τ_{eff} as temperature is ramped up from room temperature to 150 °C. (b) shows the relative τ_{eff} monitored during the two hours of annealing at 150 °C.

by an increase is shown here. The decrease in τ_{eff} has been linked to an increase in surface defect density (N_s) while the decrease in τ_{eff} has been linked to charging of void defects in the a-Si:H (see Chapter 4).

Figure 5.4 shows the MEPCD measurements performed on all the samples. The lifetime of the sample with an additional n-layer decreases with measurement flashes while the lifetime of the sample with an additional p-layer increases with measurement flashes. The result of this experiment suggest that doped a-Si:H layers do, indeed, affect the lifetime kinetics upon light soaking. This suggests that the BSF sample is dominated by an N_s increase upon light soaking while screening out void charging effects while the emitter sample is dominated by void charging effects while screening out N_s effects. Further analysis about the causes of these screening effects by doped layers is given in Section 5.4.

In Mahtani et al.'s work, a similar experiment is done and similar results are exhibited. [48] Here, the improvement in samples with an emitter had three pos-

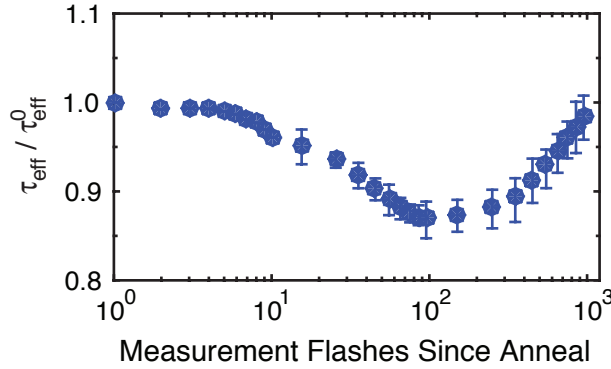


Figure 5.3: MEPCD measurement on i/c-Si/i stack

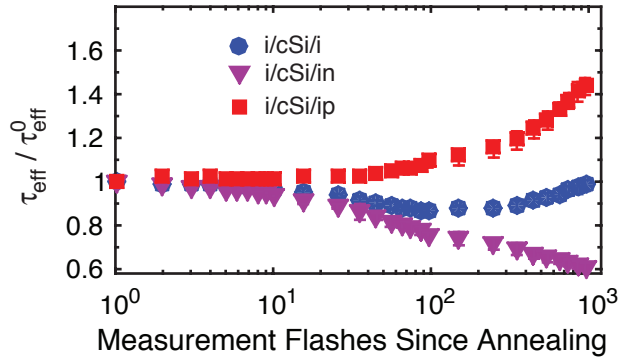


Figure 5.4: MEPCD measurement on i/c-Si/i stack, emitter stack and BSF stack.

sible explanations. The first explanation is that a defect gradient is imposed due to a higher concentration of defects in the p-type layer compared to the intrinsic layer at the surface of the c-Si wafer. Changes in this gradient due to recombination at the surface may cause interface defects to change in different ways than if there is just an intrinsic layer. However, this explanation would not distinguish between a defect gradient with n-type doping and p-type doping. In this work it is shown that the type of doping has an effect on the kinetics, and light-induced improvement only occurs when p-type doping is applied.

In their case, there was a difference in thickness between their sample with just an intrinsic a-Si:H layer and the one with a p-type layer stack. They claimed that this may be a contribution to the difference in light induced change kinetics, but as this was held constant in the experiments shown here, that explanation does not seem to hold.

Finally, they explain the results claiming that the change in electric field due to the doped layer may have an effect. This may change the rate of movement of defects during formation. This last example is the only one that is valid for the results shown from these experiments. Therefore our results, in conjunction with the analysis of Mahtani et al., suggest that the electric field induced by the emitter layer is the primary cause of light induced improvement of τ_{eff} upon light soaking.

The next step, after adding a single doped layer to the sample, was to produce a complete SHJ precursor. A p-type, a-Si:H layer is on one side of the sample to form the emitter and an n-type, a-Si:H layer is on the other side forming the BSF. When these samples are first exposed to MEPCD measurements, the lifetime tends to increase with measurement flashes. In this case, the side exposed to light was on the emitter (p-type) side of the sample. This sample was annealed again and exposed to the measurement flashes flipped over with the back surface field (n-type) side exposed. In this second run the kinetics were dominated by a decrease in lifetime. This is shown in Figure 5.5a. In Figure 5.5b the experimental order was reversed. Here, the back surface field side was flashed on the first anneal after deposition and then after the second anneal the emitter side was flashed. The kinetics were consistent with the first experiment showing that the flashing side, not the number of annealing cycles, determined whether or not the lifetime would increase.

5.4 Analysis

Explaining all the results shown in Figure 5.5 requires looking at both effects and causes of changes in τ_{eff} . Illumination of these heterostructures can both increase and decrease the τ_{eff} . The work in Chapter 4 linked decreases in τ_{eff} to an increase of N_{S} , while increases in τ_{eff} were linked to positively charging voids in the passivating a-Si:H layers. So the effects on the sample are void charging and a change of N_{S} .

Understanding what causes these effects starts with the potential effects of light exposure on samples. There are three main relevant impacts on the sample each time light is flashed. Firstly there is the generation of charge carriers in the different materials involved in the sample. A calculation of the cumulative generation profile is given in Figure 4.1. There is significantly higher generation in the c-Si wafer than in any either of the a-Si:H passivation layers here. There is also generation in the top a-Si:H with very little generation in the rear a-Si:H layer as most of the light has already been absorbed by the c-Si wafer. The second impact of this effect is recombination. In literature, recombination is widely given as the cause of the defect density increase in a-Si:H which happens during the Staebler-Wronski Effect. [89, 90] As cumulative generation is orders of magnitude higher in the c-Si wafer, and the diffusion length of minority and majority charge carriers are orders of magnitude higher than wafer thicknesses used here, recombination

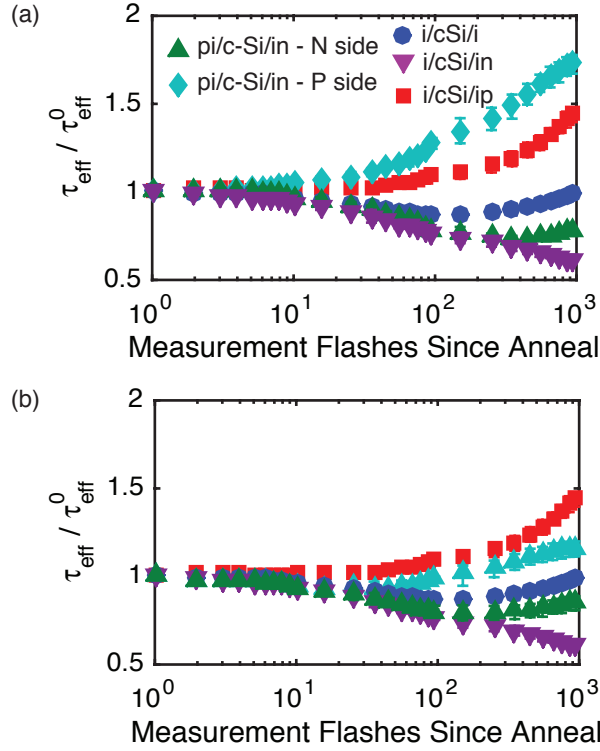


Figure 5.5: MEPCD measurement on precursor stack as well as other stacks shown in Figure 5.4. The two figures presented here obtain the same measurements for the i/i and single doped layer samples. However in the case of the precursor sample, in (a) the emitter side was illuminated first, while in (b) the back surface field side was illuminated first.

should occur in relatively equal amounts at both the front and rear side of the sample assuming similar recombination velocities at both sides. Therefore the a-Si:H layers at the front side have more generation than the a-Si:H at the rear of the sample but with roughly the same rates of recombination. The final impact, is that the samples may be heated through the light soaking. This last effect, however, is minor and should not produce any sort of annealing effects.

Table 5.2 shows which samples exhibit which effects. Samples that exhibit light induced decreases in τ_{eff} have ticks in the “ N_S Increase” column and samples that exhibit light induced increases in τ_{eff} have ticks in the “Void Charging” column. This table shows that light-induced N_S increases in all samples except for the emitter and p-illuminated precursor. In both of these cases, the p-type layer is illuminated. This suggests that the field effect caused by the p-layer either screens away the N_S increase, or amplifies the charging in the a-Si:H. To explore this further, the band diagram of the emitter side of the sample is given in Fig-

Table 5.2: Effects that are apparent upon light exposure among different samples

Stack	Name	N_S Increase	Void Charging
i/c-Si/i	Control	xx	x
p/i/c-Si/i	Emitter		xx
n/i/c-Si/i	BSF	xx	
p/i/c-Si/i/n	Precursor (p-illumination)		xx
n/i/c-Si/i/p	Precursor (n-illumination)	xx	x

ure 5.6. The band diagrams given were calculated using the modeling software, AFORS-HET. Photogenerated holes in c-Si drift towards the a-Si:H/c-Si interface while being blocked by the heterojunction. This happens at the so-called inversion layer where the band bending of the c-Si becomes more p-type. This could explain the build up of positive charge at the interface that increases the τ_{eff} . That built up positive charge changes the band structure as shown in Figure 5.6 and thusly increases τ_{eff} .

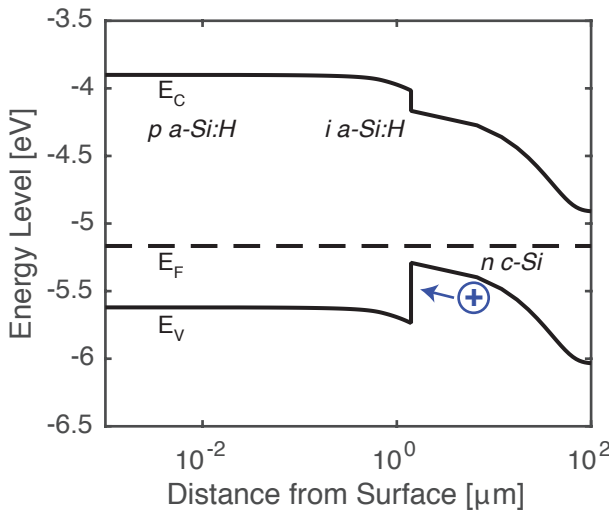


Figure 5.6: Band diagram of relevant sections of emitter sample calculated using AFORS-HET. Hole pictured at the left of the c-Si to show the capability of positive charge trapping at the interface.

The addition of a BSF has the opposite effect of the emitter. With the BSF sample, τ_{eff} degrades without any corresponding increase in τ_{eff} caused by positive void charging. This fits with the explanation that photogenerated holes may cause the positive charging in voids in a-Si:H as the BSF would screen away photogenerated holes in the a-Si:H and block photogenerated holes from the c-Si

wafer. The band diagram of the BSF of a SHJ solar cell is given in Figure 5.7. Photogenerated electrons in the c-Si will drift towards the a-Si:H/c-Si junction while encountering a barrier from the heterojunction in this case. This may cause a build up of negative charge at the interface which would reduce τ_{eff} in the same way that positive charging increases τ_{eff} . This is shown through the differences of band structures with negatively and neutrally charged interfaces in Figure 5.7.

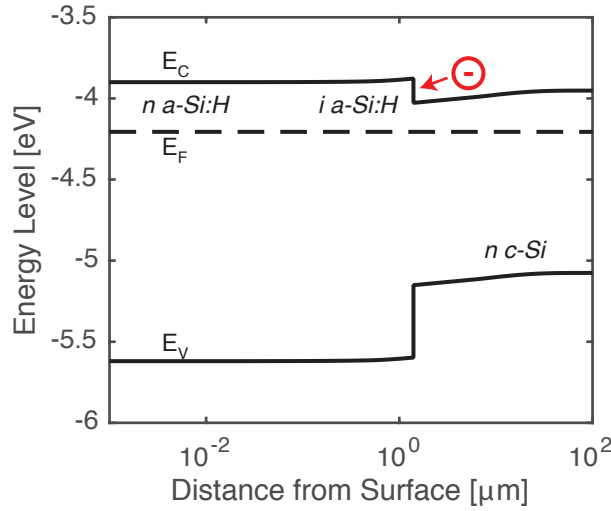


Figure 5.7: Band diagram of relevant sections of BSF sample. Electron pictured at the left of the c-Si in the conduction band to show the capability of negative charge trapping at the interface.

One potential issue with this explanation is that both the emitter sample and the BSF sample have a single intrinsic a-Si:H layer on the rear side of the wafer. The screening effects of the fields generated by the doped layers should not play any role for the rear side. However, this can be explained by recalling what the τ_{eff} measurements actually represent. In this chapter they represent the effective lifetime at an injection level of 1×10^{15} . However, this lifetime is based on the reciprocal sums of different lifetime contributions of different parts of the sample. This is expressed as:

$$\tau_{\text{eff}} = \left(\frac{1}{\tau_{\text{bulk}}} + \frac{1}{\tau_{\text{front}}} + \frac{1}{\tau_{\text{rear}}} \right)^{-1} \quad (5.1)$$

Where τ_{bulk} is the bulk lifetime, τ_{front} is the front surface lifetime and τ_{rear} is the rear surface lifetime. Because of the nature of this reciprocal addition, if the three lifetimes are of very different values, the lowest value dominates. Here $\tau_{\text{bulk}} \gg \tau_{\text{front}}$ and $\tau_{\text{bulk}} \gg \tau_{\text{rear}}$ at the injection level of $1 \times 10^{15} \text{ cm}^{-3}$. There-

fore, τ_{eff} is dependent mainly on the surface lifetimes of τ_{front} and τ_{rear} . Similarly, if $\tau_{\text{front}} \ll \tau_{\text{rear}}$ then the measured τ_{eff} will primarily be based on τ_{front} . In the case of the BSF and emitter samples, the lifetime of the side with the doped layers will likely be lower than the lifetime of the side with the thicker intrinsic layer on the back as the doped a-Si:H adds extra dangling bonds thus increasing the N_S value. Though the field effect of adding doped layers also has an influence on lifetime, an assumption is used here that N_S is a larger factor than additional field effects of doped layers on the surface lifetime. If this assumption holds, τ_{eff} is primarily determined by the lifetime of the side with the doped layer. This explains why the screening of the doped layers have such a significant effect on the τ_{eff} during light soaking even though both void charging and N_S are likely occurring at the rear side of the wafer.

Explaining the results of light soaking on precursors begins with isolating the two sides of the sample. Each of these sides have a unique surface lifetime referred to here as τ_{emitter} and τ_{BSF} . If τ_{emitter} and τ_{BSF} are on the same order of magnitude in the annealed state prior to light soaking, then changes to either surface would have a significant effect on τ_{eff} . This assumption is made by the very similar τ_{eff} values measured of the emitter and BSF sample and shown in Table 5.1.

If both sides have similar effects on the sample, and the effects are primarily caused by recombination at the interface, then there should not be a difference in light soaking kinetics depending on which side is illuminated. This is because due to the high diffusion lengths of high quality c-Si, and the fact that there are orders of magnitude more charge carriers generated in the c-Si, both sides of the sample should have relatively equivalent levels of recombination. The analysis above showed that τ_{emitter} increases upon illumination while τ_{BSF} decreases upon illumination. Assuming the surfaces of the precursors have similar properties as those used in the singled doped layer experiment, both surfaces change at equal but opposite rates when illuminated (the emitter sample reaches a final lifetime of 1.4x the initial lifetime and the BSF sample reaches a final lifetime of 0.6x the initial lifetime). If this were the case in the precursor, one would expect that the τ_{eff} would decrease based on light soaking since the degradation of lifetime would have a greater effect as is shown in Figure 5.8. In this Figure, τ_{emitter} and τ_{BSF} are reciprocally added together while one decreases and the other increases at the same rate. As can be seen, the resultant sum decreases overall. Since the precursor material does not decrease uniformly, this shows that surface recombination is not the only relevant factor in changing τ_{eff} due to light illumination. The fact that the kinetics are reversed depending on the light soaking side (Figure 5.5) implies that generation in the a-Si:H must also be playing a role in these kinetics.

This finding is fundamental to understanding the nature of light soaking kinetics of the silicon heterointerface. Prior work has suggested that recombination causes the increase in defects in a-Si:H that lead to the SWE. [89, 90] Therefore, since recombination at both sides is relatively equal regardless of the flashing side, the N_S increase should be similar regardless of the flashing side. The only

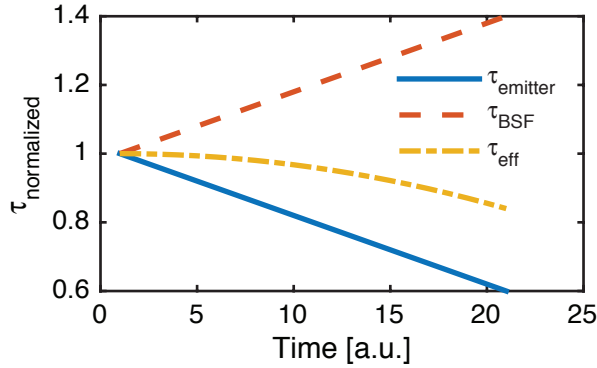


Figure 5.8: τ_{eff} if it was solely dependent on τ_{emitter} and τ_{BSF} . Here τ_{bulk} is ignored so $\tau_{\text{eff}} = \left(\frac{1}{\tau_{\text{emitter}}} + \frac{1}{\tau_{\text{BSF}}} \right)^{-1}$

difference between the two sides it that the illuminated side has significant generation while the rear side of the sample undergoes almost no light induced generation. Though this would not significantly effect the changes in N_S it could affect the light induced change in surface charging. This would imply that the negative charging at the BSF and the positive charging at the emitter may only occur when there is significant generation in the a-Si:H. As explained above, the charging can be explained by the accumulation of charge due to drift of charge carriers towards the interface that then experience a barrier at that interface. These barriers are shown in Figures 5.6 and 5.7. These results suggest that this charging that has long term effects on τ_{eff} may only occur when there is saturated generation in the a-Si:H layers. Therefore the side being flashed has a dominant effect when charging of one side would cause an increase in τ_{eff} and charging of the other side would have a decrease in τ_{eff} . This explanation of charging on illuminated sides of the sample explains why there is not the expected behavior in Figure 5.8 and why the flashed side dominates the τ_{eff} kinetics.

5.5 Conclusions

This work investigated the effect of doped a-Si:H layers on the metastable kinetics of the light induced changes to passivation quality. As has been previously shown, n-type wafers passivated with a-Si:H exhibit a decrease in lifetime followed by a recovery when exposed to light flashes. When a p-type layer is added, the sample exhibits only light induced increases in lifetime, while an n-type layer shows kinetics dominated by a decrease in lifetime. This has shown that doped layers do, in fact, have an influence on the light induced effects of the silicon heterostructure. Though similar work had been carried out in the past, this, more

extensive study, has ruled out possible explanations for the increase in lifetime caused by the p-type layer leaving only the explanation that the electric field generated at the a-Si:H interface may be influencing the lifetime kinetics. These results help to isolate the two effects of light soaking on a SHJ sample, which are an increase of N_S that decreases lifetime and a positive charging of voids in the material that increases lifetime.

Further work used full precursors that had both a p-type emitter and an n-type back surface field and tested the influence of light flashes on the lifetime of this sample. The experiments showed that the sample followed similar kinetics to those of the single doped layers and this depends on which side the sample is flashed on. Whereas previously the effects were isolated with only a BSF or only an emitter, these samples had both. The fact that the kinetics of the lifetime changes due to light soaking depend on the flashing side suggest that charging only occurs when a-Si:H has significant generation.

6

The Feasibility of FTPS on Crystalline Silicon Solar Cells

Abstract

Fourier transform photocurrent spectroscopy (FTPS) has been used to study defects in amorphous silicon layers and thin film silicon solar cells. This chapter investigates whether or not this method is suitable to study interface defects of silicon heterojunction (SHJ) solar cells and defects in thin film crystallized silicon solar cells on glass. Findings show that the subgap absorption spectrum correlates well with defect densities as measured through electron paramagnetic resonance (EPR) in thin film crystallized silicon solar cells. In terms of SHJ solar cells, subgap absorption peaks are shown to be measurement artifacts and do not correspond to interface defects. However, the SHJ FTPS study reveals some fundamental limitations and abilities of FTPS measurements of solar cells.

6.1 Introduction

Fourier transform photoconductance spectroscopy (FTPS) has been used to characterize hydrogenated amorphous silicon (a-Si:H) and nanocrystalline silicon (nc-Si:H) films to better understand their nanostructure and performance. [62, 63] The technique has been expanded to study full solar cell devices as this characterizes the contribution of these defects to full device performance more precisely. [40] This is advantageous as it allows for the study of defects during real solar cell operation rather than just as a film or powder. FTPS is a sensitive way to measure absorption at very low levels, including in the forbidden band gap. Photocurrent generated at these levels must involve defects of some sort as either excitations from the valence band to a defect or from a defect to the conduction band. [39] Therefore, FTPS signals can be related back to defect states through relating the generated photocurrent to a density of states equation by:

$$I_{\text{ph}}(E_{\text{ph}}) \propto \alpha_{\text{abs}} \propto \frac{1}{E_{\text{ph}}} \int_0^{\infty} [g(E) f(E)] \left[g(E + E_{\text{ph}}) (1 - f(E + E_{\text{ph}})) \right] dE \quad (6.1)$$

where I_{ph} is the measured photocurrent using FTPS, α_{abs} is the absorption coefficient of the absorber layer in the solar cell, E_{ph} is the excitation photon energy, $g(E)$ is the density of states and $f(E)$ is the occupation function. [91] A photocurrent level at a given energy level essentially represents how many electronic transitions are possible at that given energy level. However, Eq. 1 must be adapted for photocurrent methods such as FTPS, as only transitions to and from the extended states will result in a signal. [92] Therefore, any signal measured at a given E_{ph} below the bandgap can approximately represent either an unoccupied state E_{ph} above the valence band edge or an occupied state at E_{ph} below the conduction band edge. [40]

In this chapter, FTPS is used on two different solar cell technologies. These are polycrystalline silicon (poly-Si) on glass and Silicon Heterojunction (SHJ) solar cells. Firstly, the experimental setup is fully described. This is followed by a study that uses FTPS in conjunction with electron paramagnetic resonance (EPR) on poly-Si on glass solar cells to show the importance of shallow traps in this technology. Finally a section on why FTPS is an unsuitable method for detecting interface defects in SHJ solar cells. This last study shows the limitations of the measurement and how to interpret subgap currents in these solar cells.

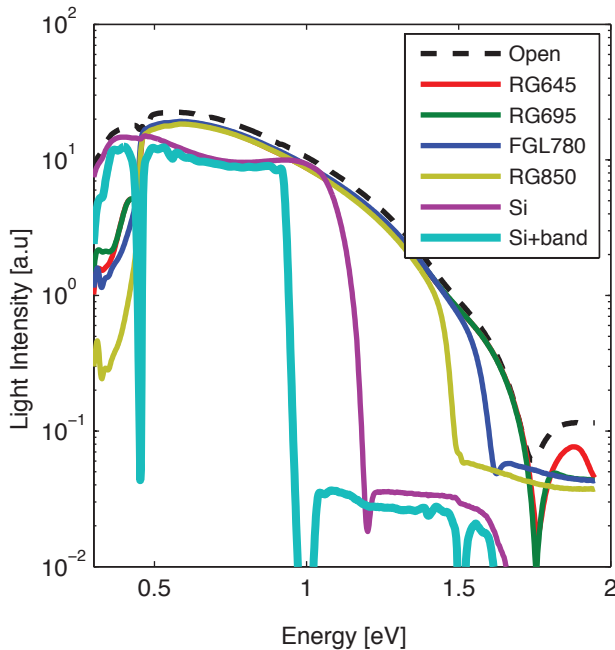
6.2 Experimental Details

The spectrometer used in the FTPS setup contains a Michelson interferometer. Different optical cut off filters are applied to the light source to allow for enhanced signals in different spectral regions. Details about this setup are described elsewhere. [63] In prior experiments five cutoff filters were used and measurements

Table 6.1: Filters used for FTPS-EQE Measurements

Filter Name	Spectral range
RG645	1.75 - 1.85 eV
RG695	1.58 - 1.75 eV
FGL780	1.40 - 1.58 eV
RG850	1.05 - 1.40 eV
c-Si Wafer	<1.05 eV
c-Si Wafer + Band Filter	<0.90 eV

were carried out through each filter. Additionally, the experiments in Section 6.4, an extra band filter is added that cuts off photon energies above 0.9 eV. This filter data is all provided in Table 6.1. The background signal measured by the FTPS signal after each filter is also given in Figure 6.1. FTPS measurements are stitched to a calibrated external quantum efficiency (EQE) measurement to make the measurements absolute. This results in a total spectrum referred to as an FTPS-EQE spectrum, which is, essentially, an EQE spectrum extended to infrared energy levels as low as 0.6 eV. [40] FTPS-EQE spectra for various solar cells employing different crystalline silicon technologies are shown in Fig. 6.2.

**Figure 6.1:** Background measurement of all filters used in this work.

In addition to poly-Si on glass (here SPC without RTA is presented as an example), a nc-Si:H [93] and a SHJ [19] solar cell are also presented. Processing procedures for these solar cells are presented elsewhere. [76, 93] Fig. 6.2 demonstrates how the subgap photocurrent (to the left of the gray line) is represented in an FTPS-EQE plot. For solar cells with very high quality crystalline absorbers and extremely low defect densities, such as the float-zone, monocrystalline silicon (mono-Si) absorber in the SHJ cells, the absorption sharply decays below the bandgap. For solar cells with absorber layers made up of a lower quality crystalline material, but still with relatively large crystalline grains, such as poly-Si on glass with grains up to mm in width and cm in length, there is a broader absorption tail extending into the bandgap pointing towards a greater defect density. In solar cell absorber layers made up of nc-Si:H, there is a significant amount of a-Si:H tissue (crystalline volume fractions of around 50-60%) [93] and smaller crystalline grains. [94] This results in even larger subgap absorption at photon energies as low as 0.7 eV that give rise to a measurable FTPS-EQE signal. Furthermore, fitting a defect distribution to this subgap absorption would require more than just a contribution from the exponential, tail state region.

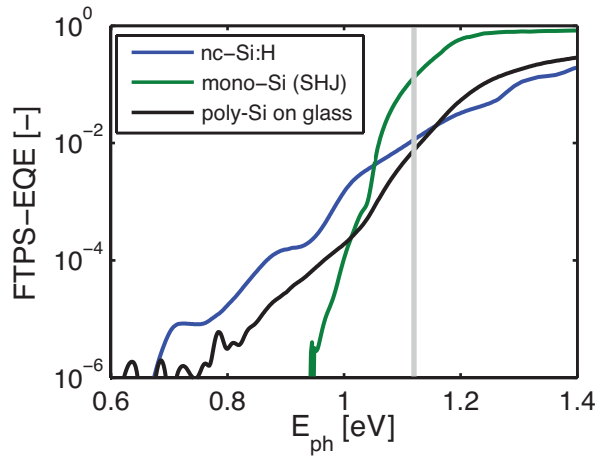


Figure 6.2: FTPS-EQE spectra for nc-Si:H, SHJ and poly-Si on glass based solar cells. The vertical gray line represents the bandgap of c-Si.

6.3 Evidence of Shallow Traps in Poly-Si Films

Polycrystalline silicon (poly-Si) on glass is a promising technology to combine low material use and processing cost with good quality crystalline silicon (c-Si) for use in solar cells. To make poly-Si on glass, amorphous silicon (a-Si) is grown

using plasma enhanced chemical vapor deposition (PECVD) or electron beam evaporation and then crystallized through different methods. [95, 96] In the past, solid phase crystallization (SPC) was established as the method of choice, but showed a clear limitation in terms of electronic quality due to a high number of intra- as well as inter-grain defects which resulted in open-circuit voltages (V_{OC}) below 500 mV. [97, 98] Recently, liquid phase crystallization (LPC) has shown promise as unique method to form large grained poly silicon on glass with well passivated interfaces and thus wafer equivalent V_{OC} of up to 656 mV. [99, 100] The record solar cell conversion efficiency of 11.8% has been reached using LPC. [101] A significant amount of research has been done exploring the relationship between defect densities and defect passivation on poly-Si films. [98, 102–104] These studies point to dangling bonds and grain boundaries as the primary defect entities in poly-Si on glass and have developed various methods of hydrogen passivation for these defects. [105, 106] There are currently two competing theories regarding the energetic position of the defects in poly-Si. One side claims that the defects are primarily composed of shallow traps [107] while others claim that these defects exist on deeper energy levels near midgap. [97] The current studies, however, lack an experimental methodology for determining the energetic positions of these defects. This work seeks to expand on these studies by experimentally determining defects in poly-Si solar cells grown on glass using a combination of electron paramagnetic resonance (EPR) and Fourier transform photocurrent spectroscopy (FTPS).

The evidence for shallow traps playing a role in recombination processes in poly-Si solar cells comes from a study done by Wong et al. using temperature dependent external quantum efficiency (EQE) measurements. [107] Activation energies between 0.17 eV and 0.21 eV of the carrier lifetimes point to shallow traps having a dominant effect at energies between 0.05 to 0.07 eV below the conduction band and 0.06 and 0.09 eV above the valence band. The role of deep defects was explored by Fehr et al. [97] In their study, quantitative EPR techniques were used to assign the paramagnetic defect density for different poly-Si materials to intra-grain and grain boundary defects. This study was extended by Sontheimer et al. on LPC Si layers with an average grain size of 200 μm and tailored SPC Si layers with similar intra-grain morphology but systematically varied grain sizes between 0.25 μm and 1 μm . This study revealed, that poly-Si in the investigated grain size regime comprises a significant amount of grain boundary defects, even after rapid thermal and hydrogen passivation treatments, while LPC-Si layers with 200 μm large grains are dominated by intra-grain defects. A further study by Seifert et al. used electron-beam induced current (EBIC) measurements to show that dislocations seem to not be present in high quality poly-Si samples on glass. [108]

A comprehensive study and set of calculations by Wong et al. has shown that a combination of deep and shallow level defects describe the solar cell performance much better than a model that only takes deep defects into account. [109] Currently, the deep level defects are being attributed to coordination defects and

defects at the surface of open volume deficiencies while the shallow traps are attributed to dislocations within crystal grains. [98] The techniques in the papers discussed so far, such as EPR, can effectively count the number of paramagnetic defects in poly-Si materials. However, FTPS can be used to measure the energetic positions of the defects in poly-Si solar cell absorber layers.

The purpose of this work is to study LPC and SPC poly-Si solar cell devices on glass with different defect densities as measured by EPR and use FTPS to measure the energetic position of the states in the bandgap. EPR specifically measures unpaired spin densities (N_S) of materials. In this case, the N_S of the absorber material of each solar cell is measured using EPR. Three different solar cells are investigated. These include an SPC cell with rapid thermal annealing (RTA), an SPC cell without RTA and an LPC cell. All samples were prepared on Corning Eagle XG glass substrates. For the SPC samples, 400 nm a-Si:H was deposited by PECVD using an H_2/SiH_4 precursor ratio of 100/20. [98] After absorber deposition the samples were crystallized for 20 h at 600 °C in a quartz furnace. Rapid thermal annealing was performed for 1 minute at 950 °C. Both SPC samples have crystal grains on the order of several μm . LPC samples were fabricated by electron beam evaporation of 10 μm amorphous silicon and subsequent crystallization using a line shaped electron beam at an energy density of 1 J/mm² and a scanning velocity of 6 mm/s. [110] The LPC and SPC without RTA samples were prepared on textured substrates while the SPC with RTA sample was prepared on a planar substrate as RTA does not crystallize properly on textured substrates. Though there are fundamental differences between the three solar cells under investigation, including crystallization type, texturing, thickness and others, the methodology used to compare these cells is still valid as a volumetric defect density is measured and only the slope of the FTPS-EQE curve is analyzed. Note that these samples are not meant to represent the best quality of each crystallization technique, but were instead selected to show a range of different poly-Si solar cell devices on glass with absorber layers of varying defect densities.

Table 6.2 shows the N_S values of the absorber materials of each solar cell as measured by EPR. These N_S values are known to have an error of approximately 30 % and are therefore rounded to the nearest order of magnitude. For the evaluation of deep defects EPR resonances around $g=2.005$, which are typically assigned to dangling bond like defects, were measured and double integrated. EPR measurements were carried out utilizing lift off of the silicon films after etching. [97]

The external parameters of the solar cells processed using the same techniques are also given. Note that the external parameters are not completely representative of the potential of the three crystallization technologies, as the thicknesses of the samples are not equal. The N_S values, however, represent a volumetric defect density and can, therefore, be directly compared.

The FTPS-EQE spectra of the three cells are shown in Fig. 6.3. The exponential region of the curve is fitted to the following equation:

Table 6.2: External parameters of poly-Si solar cells under investigation

	Cell Thickness (μm)	N_S (cm^{-3})	V_{OC} (mV)	J_{SC} (mA cm^{-2})	FF (-)	η (%)
LPC	10	10^{15}	455	14.7	0.46	3.1
SPC w/o RTA	1.1	10^{16}	241	5.01	0.28	0.34
SPC w/ RTA	1.6	10^{17}	465	21.8	0.58	5.9

$$I_{ph-ex}(E_{ph}) = I_{ph} - I_{ph-0} \exp\left(\frac{E_{ph}}{E_0}\right) \quad (6.2)$$

This equation is derived from the work of Jackson and Amer that relates the excess absorption to this exponential quantity. [111] I_{ph-ex} is the excess photocurrent due to subgap states, I_{ph} is the total photocurrent measured from FTPS and I_{ph-0} is a fitting parameter. This equation is usually used to remove the exponential part from the measurement to find the excess photocurrent due to defects, however, here only the exponential part is used to extract the E_0 parameter. Measured photocurrent is directly related to the absorption properties of the intrinsic layer of the solar cell, therefore absorption coefficient values have been replaced with photocurrent values here. Consequently, it is not possible to use the integrated subgap absorption multiplied by a proportionality constant to estimate the defect density, as has been done before for a-Si:H. [112] Furthermore, the subgap absorption as shown in Fig. 2 is extremely low, so it is not possible to pick a reliable FTPS-EQE value below the bandgap that could be used to estimate the defect density. Instead, the E_0 parameter is evaluated as an indicator of the defect density. The E_0 value used in Eq. 2 is known as the Urbach energy and has been used to characterize the exponential region in absorption of semiconductors. [113] The E_0 region is dominated by defect states in the tail region that can be linked to shallow traps. It should be noted that the oscillations present in the FTPS-EQE signal of the SPC with RTA sample are present because this sample was prepared on a planar substrate while the others were prepared on textured ones, which will smoothen out any interference. However, since the slope, E_0 is used for analysis here, these fringes do not affect the conclusions of this letter.

The E_0 values from the three solar cells are directly related to N_S values measured by EPR. This relationship is illustrated in Fig. 6.4. This shows that the spin densities obtained through EPR and the E_0 values obtained from FTPS-EQE measurements are strongly correlated. With this in mind, more can now be said about the nature of the defects that exist in poly-Si solar cells on glass.

The FTPS-EQE measurements can be used to extract information about the defect positions of absorber layers of the solar cells. Utilizing Eq. 6.2, it is clear that the increase in E_0 implies that there is a broadening of the tail state region. This can come from either the valence band or conduction band tail states. The differences between poly-Si solar cells with high defect densities and poly-Si solar

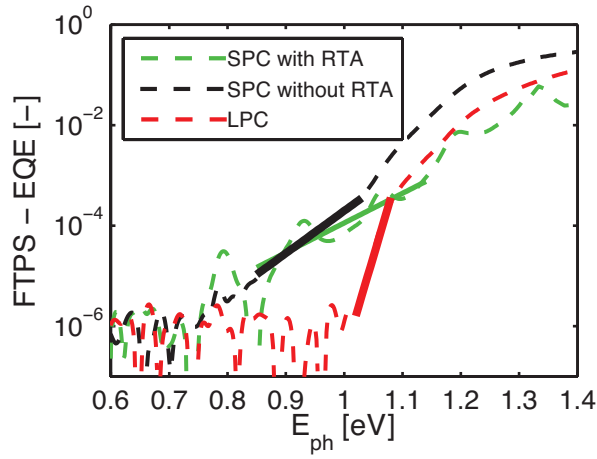


Figure 6.3: FTPS-EQE spectra from LPC, SPC without RTA and SPC with RTA solar cells. Measurement data are represented by dashed lines while exponential fits from Equation 2 are shown in solid lines.

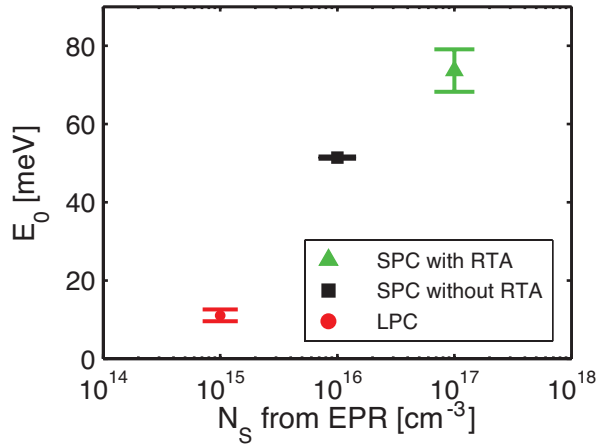


Figure 6.4: E_0 vs N_S for LPC, SPC without RTA and SPC with RTA solar cells and individual films on glass

cells with low defect densities only show up in this tail region. There appears to be little to no change in the FTPS-EQE values at energy levels below 0.85 eV. This does not, necessarily, mean that there are no deep defects present in either material as the defect levels may simply be lower than the detection limit of the FTPS

due to low light intensity at these levels. Another possibility is that the lifetime of charge carriers exceeds the limit imposed by the modulation frequency of the FTPS measurement. [39]

This relationship between N_S and E_0 can point to two different interpretations. These depend on whether or not it is accepted that shallow traps contribute to N_S or if N_S is only determined by the deep defect states. Fig. 6.5a qualitatively demonstrates what the density of shallow states and deep states would look like if shallow states contribute to N_S . In this case the different samples have different shallow state densities while the deep defects stay at the same level. This implies that the change in tail state densities accounts for the change in N_S . Fig. 6.5b demonstrates how the density of states could change if shallow states as represented by E_0 are independent of the N_S values. Here, shallow states and N_S change independently, but together. The shallow states can represent bond strains and dislocations in grains that may not result in unpaired spins. This is similar to the relationship that Stutzmann et al. claimed for a-Si:H films. [28]

Though it is not possible to distinguish whether Fig. 6.5a or Fig. 6.5b or a combination of the two is a more accurate representation of the density of defect states for the samples tested, a few assertions about poly-Si on glass can be made from these measurements. It is apparent that defect rich poly-Si and low defect poly-Si have a similarly different density of shallow traps, implying that if a high density of shallow traps is present in a material, it is likely to be of poor quality. Further, though the existence of deep defects in poly-Si cannot be ruled out, the lack of a signal in the 0.6-0.8eV range in the FTPS-EQE measurements suggests that these defects do not have significantly high densities. Similar measurements made on a-Si:H solar cells do produce significant signals in the subgap, which are strongly linked to defects. [40] Finally, it can be asserted that extracting the E_0 parameter from an FTPS-EQE measurement is a powerful complementary tool to EPR for monitoring the quality of both poly-Si films and absorber layers in solar cells on glass.

6.4 Interface Defects of SHJ Solar Cells

As described in previous chapters of this thesis, interface defects are an important part of understanding the nature of SHJ solar cell technologies. As FTPS-EQE had been used effectively to study defects in various solar cell technologies, a study on SHJ solar cells was performed to test if this technique is feasible to gain further understanding to the nature of these interface defects.

Figure 6.6 shows a typical FTPS-EQE spectrum. Here the five typical filters were used as given in Table 6.1. Of note in Figure 6.6 are the peaks present in the energy levels below the bandgap of the c-Si absorber. Other samples were created with different conditions at the interface and these peaks consistently showed up across various samples. As subgap absorption relates to defects in FTPS-EQE measurements of a-Si:H cells and interface defects are of interest, this

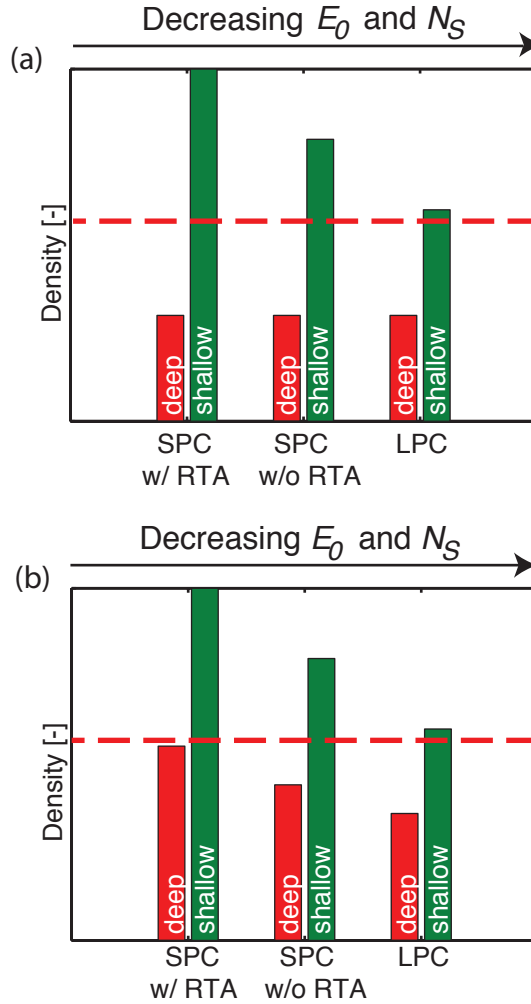


Figure 6.5: Representation of interpretations of Fig. 6.4. (a) shows the possibility where shallow traps make a significant contribution to N_S . (b) shows a possible case where N_S and shallow traps are independent. Both cases are not drawn to scale and merely serve to illustrate qualitative differences. The red, dashed line represents the detection limit for deep defects with FTPS.

poses the research question as to whether or not these peaks are created by the defects themselves. Therefore, an additional filter was purchased and used, referred to as the band filter in Table 6.1. This filter cuts off more of the absorption spectrum while passing through the light where the subgap peaks exist. The result of using this filter in the lower energy photon range is also given in Figure

6.6. Here those peaks disappear into noise while the light in that spectral region is still equivalent. This shows that these peaks are not evidence of defects but rather an artifact of the FTPS-EQE measurement when using more light.

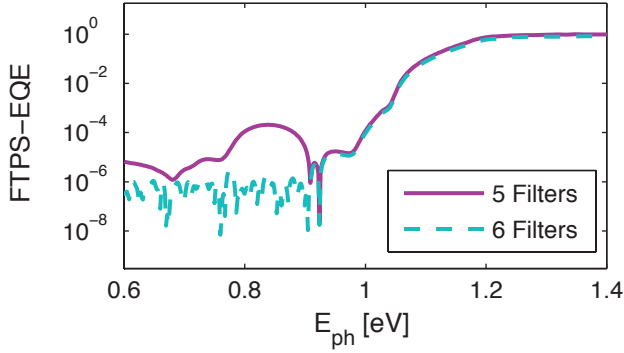


Figure 6.6: FTPS-EQE measurement on a SHJ solar cell. 5 filter measurement done without the use of the band filter and 6 filter measurement done with all filters listed in Table 6.1

To explain the nature of this artifact the FTPS measurement of just the c-Si wafer is provided in Figure 6.7. In Figure 6.6 only the signal below 1.4 eV was used from this measurement but in seeing the signal above this level it is clear that the sub-gap peaks are mirrored and similar peaks are visible at higher energy levels. It is very likely that these peaks have nothing to do with the materials under investigation but are simply sidelobes due to imperfections in apodization of the signal. As windowing is involved in interpreting an interferogram to produce an FTPS signal, the window used can create sidelobes in the signal. This is visualized in Figure 6.8 with a very crude boxcar windowing function. Though more advanced windowing functions are used in the FTPS-EQE measurements, these results show that if you look at signals orders of magnitude below the peak measurement in an FTPS signal, sidelobes can still appear.

Furthermore, the fundamental principle of the measurement implies that there may be barriers to detecting defects using FTPS. FTPS-EQE measurements operate on the basis of generating a measurable photocurrent. In the case of a-Si:H solar cells, where the bulk absorbing material contains defects of interest, they significantly increase the density of states in the forbidden gap. Therefore electrons can move from the valence band to an unoccupied state or move from an occupied state to the conduction band and the resultant charge carriers can contribute significantly to current. [39, 63] However, in the case of SHJ solar cells, the defects only exist in a very narrow depth of a few nanometers whereas the bulk absorbing material is on the order of hundreds of micrometers. Since the defects of interest are no longer in the bulk absorbing material, and are thereby now in a

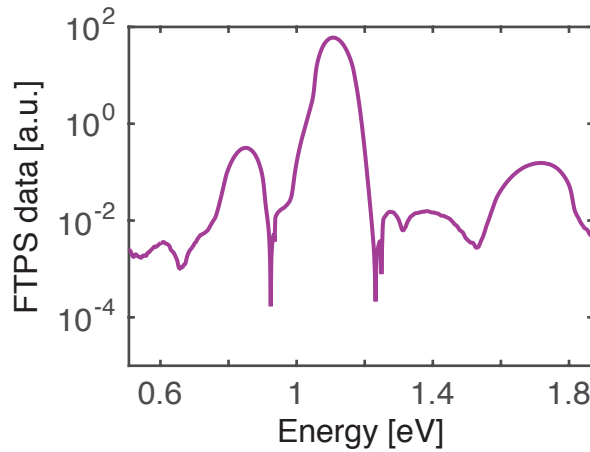


Figure 6.7: FTPS-EQE measurement of SHJ solar using only the Si filter.

small interface, it is unlikely that there is an abundance of states large enough to significantly contribute to the photocurrent measured by the system.

6.5 Conclusions

This chapter has shown that solar cell FTPS-EQE measurements correlate with defect density measurements made by EPR in poly-Si based solar cells on glass. The measurements suggest that increasing spin densities, as measured by EPR, correspond to an increased broadening of the tail state region, as measured by FTPS. This supports the claim that the defects in the absorber material of poly-Si solar cells are composed of shallow traps. Finally, this work has demonstrated that FTPS is a valid complimentary tool or alternative to EPR to measure the quality of the absorber material in poly-Si solar cells. Further work and measurements on a wider variety of poly-Si samples is suggested to confirm the statistical significance of this relationship.

Furthermore, experiments on SHJ solar cells illustrate fundamental limitations of the FTPS-EQE measurement technique. Here it was shown that signal represented in the subbandgap energy levels were not, in fact, due to photocurrent through defects but just an artifact of limited apodization of the signal. Though this did not lead to any useful insights to the a-Si:H/c-Si interface, it did illustrate important limitations to this technique.

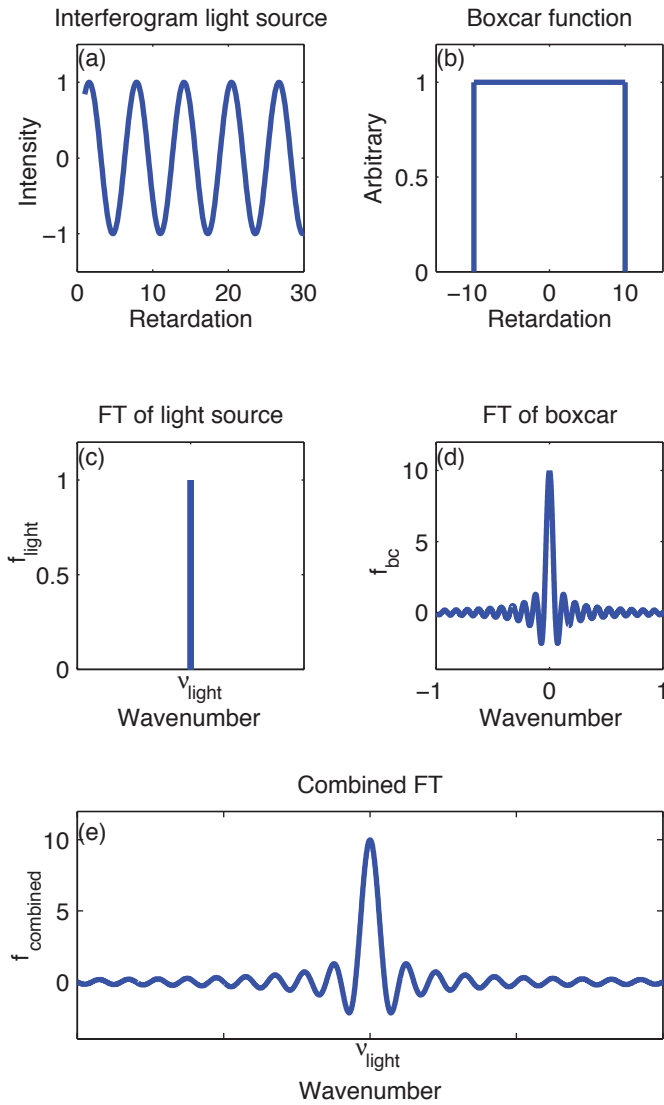


Figure 6.8: Illustration of sidelobe issues. (a) an interferogram of a monochromatic light source. (b) the boxcar windowing function. (c) the Fourier transform of the interferogram of the monochromatic light source. (d) the Fourier transform of the boxcar windowing function. (e) the convolution of (c) and (d) to give the final signal as would be measured by an FTPS setup.

7

A Tandem nc-Si:H/Silicon Heterojunction Solar Cell Designed for Water Splitting

This chapter is based on the publication:

R. Vasudevan, Z. Thanawala, L. Han, T. Buijs, H. Tan, D. Deligiannis, P. Perez-Rodriguez, I. A. Digdaya, W. A. Smith, M. Zeman, and A. H. Smets, "*A thin-film silicon/silicon heterojunction hybrid solar cell for photoelectrochemical water-reduction applications*", *Solar Energy Materials and Solar Cells* 150, 82 (2016). [114]

Abstract

A hybrid tandem solar cell consisting of a thin-film, nanocrystalline silicon top cell and a silicon heterojunction bottom cell is proposed as a supporting solar cell for photoelectrochemical applications. Tunneling recombination junction engineering is shown to be an important consideration in designing this type of solar cell. The best hybrid cell produced has a spectral utilization of 30.6 mA cm^{-2} , a J_{SC} of 14 mA cm^{-2} , a V_{OC} of 1.1 V, a fill factor of 0.67 and thus an efficiency of 10.3%. A high solar-to-hydrogen efficiency of 7.9% can be predicted when using the hybrid cell in conjunction with current a-SiC photocathode technology.

7.1 Introduction

Photoelectrochemical (PEC) water splitting is becoming a viable and important method for solar energy conversion in the form of hydrogen fuels. A complete PEC cell requires two electrodes where one of them is photoactive (either a photocathode or photoanode) and the other electrode is called the counterelectrode. Solar-to-hydrogen (STH) conversion efficiencies of up to 18.3% have been reported. [115] However, these devices use expensive, scarce materials such as gallium arsenide and gallium indium phosphide, which are also not highly water-resistant. [115, 116] Thin-film amorphous silicon carbide (a-SiC:H) has been used as a photocathode material for water reduction as it is a much more practical material for larger scale applications. [117–120] This technology is showing a lot of promise as a photocathode based on a-Si_{0.9}C_{0.1}:H can theoretically generate a maximum photocurrent density of 15 mA cm⁻² or a STH efficiency of 18% corresponding to its bandgap of 2.0 eV. [51, 121] Figure 7.1 illustrates the fundamental components of an a-SiC:H based photocathode consisting of a thin intrinsic a-SiC:H absorber as well as a gradient doped boron-doped (p-type) a-SiC:H layer and a phosphorous doped (n-type) nanocrystalline silicon oxide (nc-SiO_x) layer.

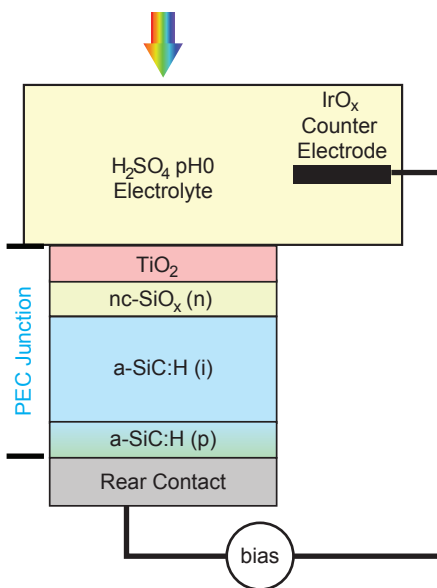


Figure 7.1: Schematic illustration of an a-SiC:H photocathode. Note a 1 nm platinum catalyst at the TiO₂ surface is not present in the sketch.

A challenge to achieving a high STH efficiency is that the low photovoltage of photocathodes (0.8 V in the case of a-SiC:H technology) is not enough to over-

come the thermodynamic water-splitting potential of 1.23 V. [49] In addition to this 1.23 V the overpotentials necessary to drive the overall redox reactions need to be considered. [50] As a result, an external bias is required for this structure to achieve its maximum current density. [118]

Integrating a solar cell at the back of the PEC device to realize a monolithic PEC/PV device can directly produce hydrogen without any external bias. [122–124] Various PEC/PV configurations have been demonstrated based on amorphous silicon alloys, such as a-SiC:H/a-Si:H, a-SiC:H/a-Si:H/nc-Si:H, and a-SiC:H/nc-Si:H/nc-Si:H junctions. [51] The STH efficiency in all of these cases is primarily hindered by the potential current density of the supporting solar cell based on thin-film silicon technology.

For typical lab-scale PV device engineering, the target is usually to achieve the highest solar-to-electricity (STE) efficiency under an AM 1.5 spectrum. For PV devices that support PEC structures in a monolithic device, however, the role of the PV supporting structure is to overcome the water-splitting overpotentials while driving the necessary current to maximize the STH efficiency that the photoactive electrode is capable of. Another way of saying this is that the JV curve of the PV device under the transmitted light spectrum of the PEC junction should intersect the saturation current of the PEC.

In this work, an alternative PV structure is proposed for the a-SiC:H photocathode to realize a silicon based and bias free prototype with a high STH efficiency. This PV component consists of a thin-film, nano-crystalline silicon (nc-Si:H) top cell and a silicon heterojunction (SHJ) bottom cell. A schematic of the monolithic structure with an a-SiC:H photocathode and the supporting nc-Si:H/SHJ stack is given in Figure 7.2a. It should be noted that to achieve a monolithic support structure, the solar cell should be illuminated from the n-side rather than traditional p-side illumination for nc-Si:H and SHJ technology. For the SHJ cell, in particular, this resulted in a decision to use a p-type wafer instead of the traditional n-type wafer. Though state of the art SHJ solar cells based on n-type wafers can achieve efficiencies of up to 25.6%, [125] progress has also been made on p-type c-Si wafers. [19, 126] A cross-sectional scanning electron microscope (SEM) image of the hybrid cell highlighting the high quality nc-Si:H junction is shown in Figure 7.2b.

Nc-Si:H and SHJ technologies were chosen as they can properly utilize the transmitted spectrum of a-SiC:H as shown in Figure 7.2c. This transmitted spectrum was measured with the same class AAA solar simulator that is used for JV measurements in this work. Having two PV cells with bandgaps of 1.1 eV is a very effective way to utilize the remaining spectrum shown in red in Figure 7.2c. This work shows the optimization of this hybrid nc-Si:H/SHJ solar cell as a component in the silicon based PEC/PV device as well as a simulation of how the hybrid cell will perform in the full PEC/PV monolithic device along with an a-SiC:H photocathode.

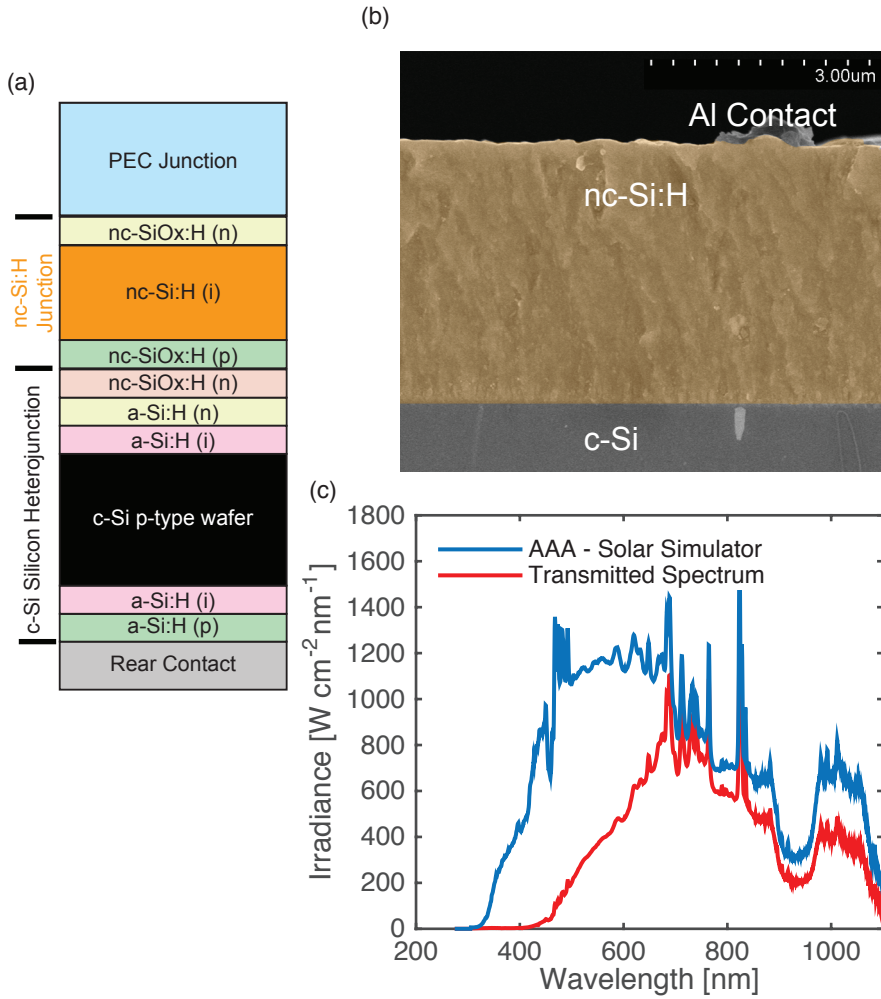


Figure 7.2: (a) Schematic illustration of the monolithic PEC/PV cathode based on a-SC:H/nc-Si:H/SHJ structure. (b) SEM cross section of the standalone PV hybrid cell. (c) Measurement of solar simulator spectrum as well as the transmitted spectrum after the a-SiC:H photocathode

7.2 Experimental Details

7.2.1 Photocathode Preparation

In this work, an a-SiC:H photocathode was fabricated to determine the design rules for the supporting PV structure. The details of its fabrication by radio-frequency plasma-enhanced chemical vapor deposition (RF-PECVD) are shown elsewhere. [51] It was deposited on a corning glass substrate. The photocathode stack consisted of a 10 nm p-doped a-SiC:H(B) layer, a 40 nm gradient p-doped a-SiC:H(B) layer, a 100 nm intrinsic a-SiC:H layer, a 10 nm nc-SiO_x layer with a 25 nm TiO₂ layer coated with a 1 nm platinum catalyst. The individual layers that make up the PEC were independently deposited and measured with spectroscopic ellipsometry (SE) to obtain their optical parameters for use in optical simulations.

The *JV* of the a-SiC:H photocathode was measured under simulated AM 1.5 solar illumination (100 mW cm⁻²) using a NEWPORT Sol3A Class AAA solar simulator (type 94023A-SR3). A spot of 6 mm in diameter on the photocathode was illuminated, corresponding to an active area of 0.283 cm². A plated iridium oxide (IrO_x) counter-electrode was utilized. An electrolyte with a 1M concentration of sulfuric acid (H₂SO₄) with a pH of 0 is used. These measurements show how the photocathode acts in a complete PEC cell as a two-electrode measurement was used. Therefore, barriers in the whole water-splitting system, such as losses in the counter electrode and properties of the electrolyte are all considered. [127, 128]

7.2.2 Optical Simulations

Optical simulations were carried out using an in-house built software GenPro. GenPro uses a 1D simulation tool to solve Fresnel equations and determine how much light is absorbed in the absorber layer of each junction. This absorption amount is converted to an incident photon conversion efficiency (IPCE) for the case of the PEC junction and an external quantum efficiency (EQE) in the case of PV junctions. The electrical losses are neglected here as this is only the first approximation. In the case of the c-Si wafer, optical data from Green et al. were used. [129] In the case of nc-Si, optical data from Murata et al. were used. [130] For the other thin-film layers, SE data were used to extract the relevant optical parameters for the simulation. These simulations served to determine optimal thicknesses to current match the absorber materials in the a-SiC:H/nc-Si:H/SHJ PEC/PV device as well as the standalone nc-Si:H/SHJ hybrid PV cell produced in this work.

7.2.3 Solar Cell Fabrication

The fabrication of the SHJ and nc-Si:H were carried out using the same PECVD cluster tools. For the SHJ solar cells, $\sim 280\text{ }\mu\text{m}$ thick, ~ 4.0 inches in diameter, double-side polished float-zone c-Si, p-type $\langle 100 \rangle$ oriented wafers from Topsil were used as substrates. These substrates were cleaned according to a standard procedure described elsewhere. [76] The final termination step was carried out in a 0.5% diluted HF solution for 40 seconds. The a-Si:H layers were prepared using RF-PECVD and Indium Tin Oxide (ITO) was deposited using a magnetron sputtering tool. Contacts were deposited using physical vapor deposition (PVD).

The nc-Si:H single-junction solar cells were prepared on a piece of flat Corning XG glass as growth on this substrate would closely resemble growth on a flat wafer used in the hybrid tandem device. Indium Tin Oxide (ITO) was deposited on the glass using a magnetron sputtering tool. This was followed by a protective aluminum doped zinc oxide (AZO) protective layer, which was also deposited using sputtering. The remaining layers were deposited using RF-PECVD. The stack is made up of doped nanocrystalline silicon oxide layers (nc-SiO_x:H) and an intrinsic nc-Si:H layer. The deposition conditions have been explained elsewhere. [93]

7.2.4 Solar Cell Characterization

The *JV* characteristics of all solar cells were measured under illumination of a WACOM Class AAA solar simulator. External quantum efficiency (EQE) measurements were performed with an in-house setup, utilizing a monochromatic light source. The *JV* curves presented here have been transposed using the current density values measured by EQE in order to avoid overestimation from the *JV* measurements. For the transmitted spectrum *JV* measurement in Figure 7.7c, the full a-SiC:H device was used as a light filter resulting in the red spectrum as shown in Figure 7.2c.

7.3 Results

7.3.1 Photocathode

Figure 7.3 shows the performance of the a-SiC:H PEC device without a supporting solar cell. At 0 V external bias, this PEC cell only produces around 1 mA cm^{-2} though significant currents up to 6.5 mA cm^{-2} are possible with an external bias. This *JV* curve provides us with the parameters necessary for designing a supporting PV structure. Based on the *JV* curve in Figure 7.3, the PV cell should be able to deliver a current density of 6 to 7 mA cm^{-2} at a voltage of 0.8 to 1.0 V. This should be achieved under the illumination of the transmitted spectrum through the a-SiC:H layers as shown in Figure 7.2c. Enhancements in photocathode technology will eventually increase the current density produced here shifting the *JV*

curve downwards to an eventual saturation current of up to 19.7 mA cm^{-2} . [131] Enhancements in catalyst and counterelectrode technology will also reduce the overvoltage of the PEC system shifting the curve to the left. Therefore producing a hybrid cell that can produce higher currents at around 0.8 to 1.0 V is favorable taking into account these future enhancements.

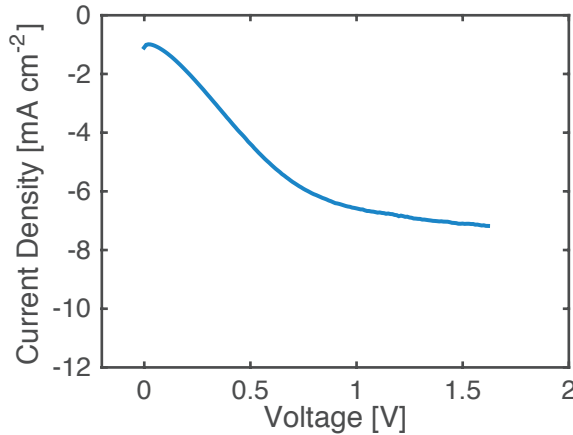


Figure 7.3: The J/V curve of an a-SiC:H photocathode as measured with a two-electrode measurement with an IrO_x counter electrode.

7.3.2 Simulations

Before implementing this solar cell, simulations were carried out to determine the optimum thickness of the nc-Si:H absorber layer. Figure 7.4 shows the absorption spectrum of the a-SiC:H (PEC), nc-Si:H (PV) and SHJ (PV) cells, respectively, whereas Figure 7.5 shows the optimized simulation of a nc-Si:H/SHJ hybrid tandem cell illuminated by simulated AM 1.5 solar spectrum.

For a first approximation, the thickness of the c-Si wafer was held constant as $280 \mu\text{m}$ and the thicknesses of the PEC and nc-Si:H junction were changed until ideal current matching conditions. In this case, current matching occurred with a a-SiC:H thickness of 415 nm and a nc-Si:H thickness of $9.2 \mu\text{m}$. This resulted in a matched current of 10.7 mA cm^{-2} . The spectral absorption is given in Figure 7.4a. These thicknesses are unrealistic as devices with those thicknesses would exhibit significant electrical losses and require long deposition times. This does, however, present the maximum current that can be produced if light trapping techniques are utilized to maximize the optical thickness of the thin film absorber layers while leaving them realistically thin.

Another simulation was carried out with a limit of $5\text{ }\mu\text{m}$ applied to the nc-Si:H absorber layer. Here an a-SiC:H thickness of 246 nm produces the highest current of 9.4 mA cm^{-2} even though the SHJ will produce a higher current of 12.9 mA cm^{-2} . The spectral absorption of this, more realistic option, is given in Figure 7.4b.

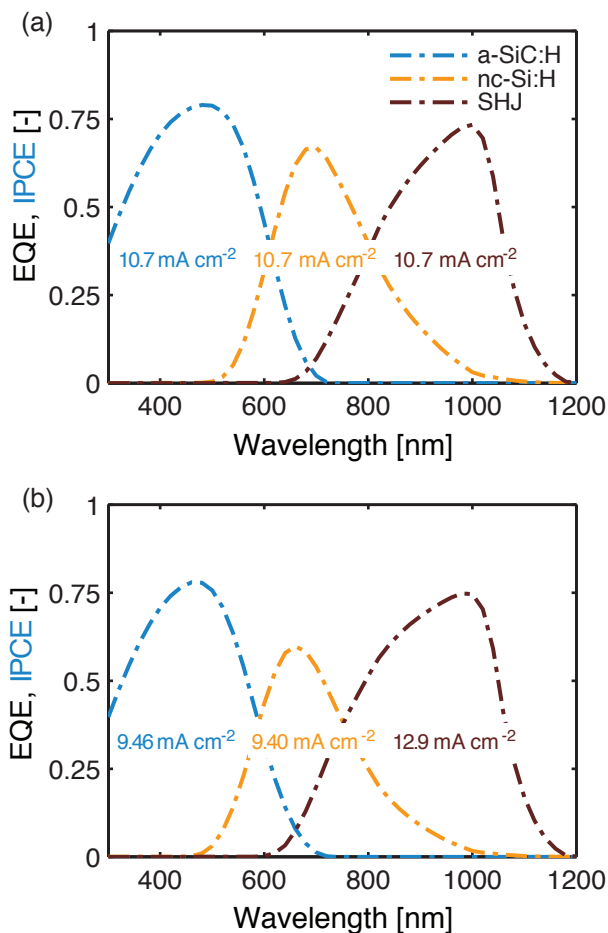


Figure 7.4: Simulated IPCE of an a-SiC:H photocathode and EQE of supporting PV stack. (a) Thicknesses used to achieve ideal current matching. (b) Practical thicknesses used.

As the focus of this chapter is the optimization of the nc-Si:H/SHJ PV stack, simulations were also carried out to current match the PV junction with a full AM 1.5 spectrum. Figure 7.5 shows the EQE of a thickness optimized double-

junction cell that ignores the photocathode. As shown here, a thickness of $2.8\text{ }\mu\text{m}$ in the nc-Si:H absorber gives a very closely matched current of 17.7 mA cm^{-2} with the wafer of the SHJ. Though the ideal layer thickness for a current matched double cell is predicted here to be $2.8\text{ }\mu\text{m}$, $3.5\text{ }\mu\text{m}$ was used as this would serve to perform better in the transmitted spectrum used to simulate using this PV stack in a monolithic device while still achieving comparable currents in AM 1.5 conditions.

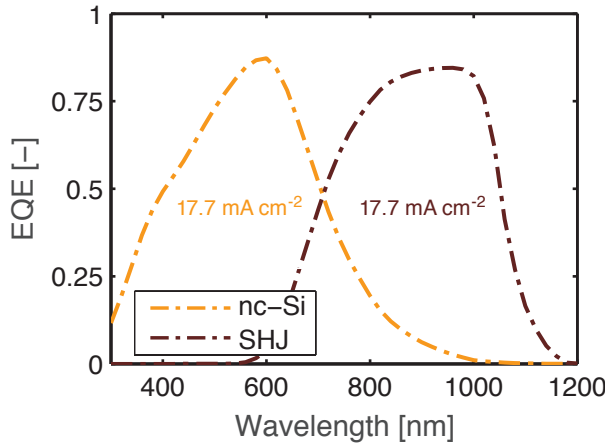


Figure 7.5: Optical simulation of standalone nc-Si/SHJ PV stack.

7.3.3 Single Junction Solar Cells

The hybrid tandem cell required the development of nc-Si:H solar cells and SHJ solar cells that are illuminated from the n-side. This section presents the challenges involved in engineering both of these single junctions as solar cells illuminated from n-side.

In the case of nc-Si:H, efficiencies of above 10% have been reported with these deposition conditions. [93] However, this was based on a growth on a textured substrate with p-side illumination. Table 7.1 shows the external parameters of the solar cell when deposited on a flat substrate and illumination from the n-side as compared to the best results reported with this recipe. It should be noted that these devices cannot be directly compared due to a difference in the thickness of the absorber layer. However, due to the poorer light trapping properties of a flat device and the electrical and shading losses from the n-side illumination, J_{SC} decrease significantly. The V_{OC} and FF do not deviate significantly from the textured, p-side illuminated cell.

For the SHJ, a p-type $\langle 100 \rangle$ wafer was used. It should be noted that a rear emitter solar cell with an n-type wafer is also possible, though better results were

Table 7.1: External parameters of single junction n-illuminated nc-Si:H solar cell on textured substrate as well as on flat substrate with n-side illumination

	Optimal Device [93]	Flat substrate w/ n-illumination
thickness (μm)	3	2.5
V_{OC} (V)	0.551	0.532
J_{SC} (mA cm^{-2})	26.0	20.04
FF	0.701	0.694
η (%)	10.0	7.40

obtained here by using a p-type wafer. One parameter that was important for improving the efficiency of this junction in the cell stack was the front i-layer. Wei et al. has shown that increasing the thickness of the front i-layer on a p-type SHJ solar cell increases the J_{SC} and FF . [132] Repeating this experiment showed similar results as shown in Figure 7.6. The J_{SC} is the main factor for the increase in STE efficiency here. The increase in J_{SC} points to a current collection issue at the front n/i interface when the i-layer is not of a sufficient thickness.

7.3.4 Hybrid Tandem Solar Cell

The black, dashed line in Figure 7.7a shows the JV curve of the first hybrid tandem cell. A thickness of $3.5 \mu\text{m}$ was used for the nc-Si:H intrinsic, absorber layer. There is a notable S curve indicating a large barrier in the solar cell. Engineering the tunneling recombination junction (TRJ) mitigates this. Two main approaches for this optimization were carried out. The first approach was to add an n-type nc-SiO_x layer between the two junctions. A discussion of the processing techniques of this material is presented elsewhere. [133] This was followed by an increase in the doping of the n-layer of the SHJ by increasing the phosphine flow in the processing plasma. Figure 7.7a shows how engineering the TRJ effects the JV curve of the solar cell and it is evident that adding nc-SiO_x and increasing the doping of the SHJ n-layer significantly improves the performance of the PV cell. The resultant nc-Si:H/SHJ hybrid tandem cell has a V_{OC} of 1.1 V and an efficiency, under AM 1.5 illumination, of 10.3%.

This is consistent with engineering of multijunction thin-film silicon devices such as so-called micromorph solar cells. N-type nc-SiO_x has been used in TRJs of micromorph cells to improve both optical and electrical characteristics. [134] Adding highly doped layers at the TRJ has increased recombination in this junction and thus improved multijunction solar cell efficiencies. [135] Having a relatively lower doped TRJ creates a barrier in the tandem device whereas adding highly doped layers in the TRJ increases recombination, which aids in the performance of multijunction devices and shows here to be essential when engineering a nc-Si:H/SHJ tandem device.

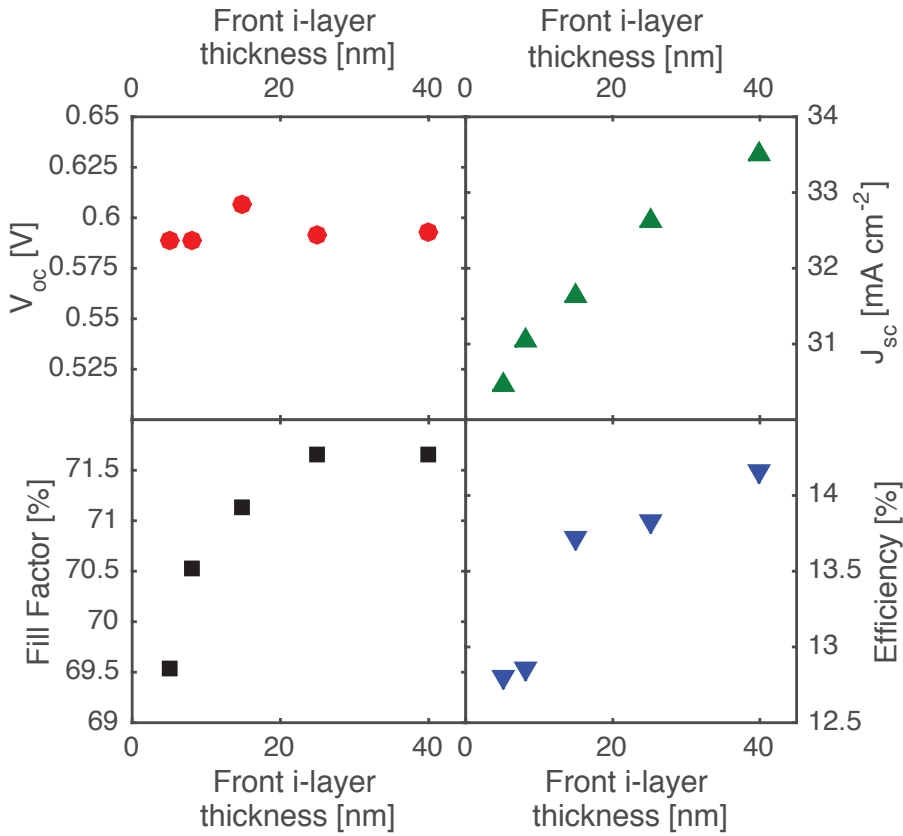


Figure 7.6: External parameters of SHJ solar cells based on a p-type wafer from varying the thickness of the i-layer on the emitter side.

Figure 7.7b shows an EQE of this solar cell. This demonstrates that current matching under AM 1.5 illumination conditions was achieved. Summing up the J_{sc} of the two junctions of this hybrid cell shows that it achieves a spectral utilization of 30.6 mA cm^{-2} with a flat configuration. Though this works as a first step into thin-film silicon/SHJ hybrid tandem cell technologies for water splitting, implementing light trapping techniques such as texturing and intermediate reflectors with this technology could achieve a greatly improved spectral utilization. Further optimization of the TRJ and better performing p-type SHJ solar cells (V_{OC} of 0.717 V have been reported[126]) could potentially increase the V_{OC} of this hybrid device to between 1.2 and 1.3 V.

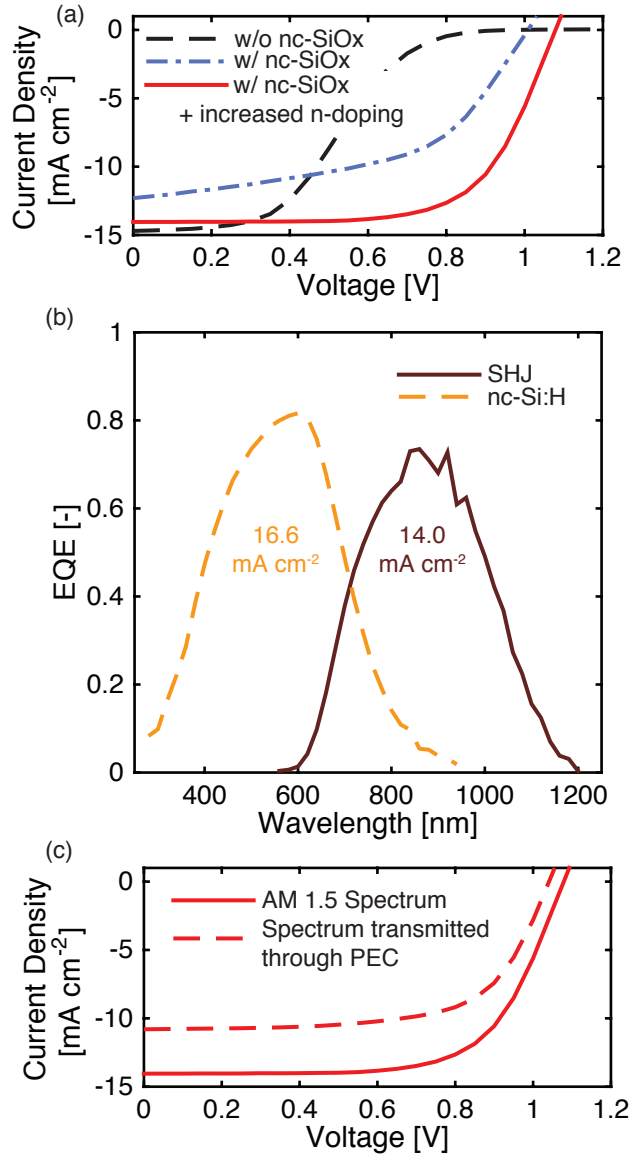


Figure 7.7: Optimization of nc-Si:H/SHJ hybrid tandem cell. (a) *JV* curve of the hybrid solar cell with different TRJ configurations. (b) EQE curves of the optimized hybrid solar cell. (c) Shifting of the *JV* curve of the hybrid cell when a standard PEC is used as a filter to only allow the light that would hit the hybrid cell if it were integrated into a monolithic PEC/PV structure.

7.4 Integration Simulation

In order to determine the potential of this hybrid tandem cell in the PEC/PV hybrid tandem structure for water splitting, the performance of the solar cell under the spectrum transmitted by the a-SiC:H photocathode must be produced. This transmitted spectrum is shown in Figure 7.2b. The spectrum was produced by taking an a-SiC:H photocathode and using it as an optical filter under the WACOM solar simulator in front of the nc-Si:H/SHJ hybrid tandem device. The resulting JV curve is shown in Figure 7.7c. It is clear that the operating points are reduced because of the more limited illumination conditions.

This JV curve can be overlaid with the measured spectra of the a-SiC:H photocathode, which has been shown in Figure 7.3b. The overlapping JV curves are given in Figure 7.8. The crossing point of this graph predicts that if the nc-Si:H/SHJ hybrid cell were to be used as a supporting solar cell structure, it would produce a current density of 6.43 mA cm^{-2} which corresponds to an STH efficiency of 7.90%. Improvements in PEC technology will shift the JV curve of the PEC down and to the left pushing the ideal crossing point closer to the maximum power point of the hybrid PV cell presented here. Therefore as PEC technology progresses, the hybrid cell will be an even more suitable candidate for a PV support structure.

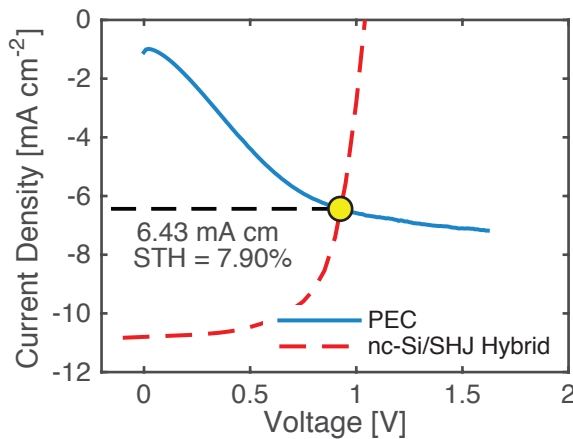


Figure 7.8: Integration simulation of nc-Si:H/SHJ hybrid tandem cell with a-SiC:H based photocathode. JV curve of hybrid PV structure and PEC curve shown along with predicted current density and STH efficiency.

7.5 Conclusions

This chapter has demonstrated the capabilities of using an a-SiC:H photocathode with a nc-Si:H/SHJ hybrid solar cell as a supporting structure. A working solar cell has been produced yielding a STE efficiency of 10.4% under an AM 1.5 spectrum. Tunneling recombination engineering has been identified and addressed as an important consideration for this hybrid device where the use of nc-SiO_x and doping concentrations of the SHJ n-layer can significantly improve the efficiency of the solar cell. Furthermore, an integration of the solar cell with current PEC technology has been simulated predicting a high operating current of 6.43 mA cm⁻² corresponding to a STH efficiency of 7.90%.

8

Conclusions

As stated in Section 1.5, the goal of this work was to answer the following research questions:

1. What is the nature of the metastable properties of a-Si:H passivation of c-Si?
 - a) How is the a-Si:H/c-Si interface affected by annealing?
 - b) How is the a-Si:H/c-Si interface affected by light soaking?
 - c) How does adding doped layers affect these light induced effects?
2. Can Fourier Transform of Photocurrent Spectroscopy (FPTS) be used to better understand the a-Si:H/c-Si interface?
3. How can novel applications using SHJ solar cells be used to aid in water-splitting applications?

This chapter discusses the progress made in all of these goals.

8.1 What is the nature of the metastable properties of a-Si:H passivation of c-Si?

This question has been explored in Chapters 3, 4 and 5. Each of these chapters answer one of the subitems above.

8.1.1 How is the a-Si:H/c-Si interface affected by annealing

Chapter 3 showed that to answer this question, proper temperature dependent modeling of the injection dependent, minority carrier lifetime is necessary. This model uses defect density, charge density and capture cross sections as input parameters and outputs the minority carrier lifetime. Minority carrier lifetime curves can be measured using photoconductance decay. Fitting these measured curves with this model allows for the calculation of defect and charge density at the a-Si:H/c-Si interface. Though this model existed in literature, this chapter showed how to account for temperature based effects in order to utilize the model at annealing temperatures rather than just room temperature.

In literature, annealing has shown to decrease the dangling bond density at the a-Si:H/c-Si interface while keeping charge density constant. Some sample experiments using the new temperature dependent model showed that the deposition conditions of the a-Si:H could influence the change in dangling bond density. Furthermore, when a-Si:H was deposited using other deposition conditions, annealing had little to no defect or charge density. This leaves the question of the annealing kinetics open. Though the experiments here did not bring full understanding to the annealing kinetics, the tools for further exploration, namely the temperature dependent stage and the interface modeling were fully formed and presented.

8.1.2 How is the a-Si:H/c-Si interface affected by light soaking?

Light induced minority carrier lifetime kinetics were explored in Chapter 4. Literature up to this point has explained minority carrier lifetime changes of silicon heterojunctions by an increase in dangling bond density at the a-Si:H/c-Si interface. Work here has shown that for many a-Si:H/c-Si interfaces, this explanation is insufficient. At long continuous light exposure as well as a large number of measurement flashes, certain samples exhibit light induced improvements to minority charge carrier lifetime. This cannot be explained by simply dangling bond generation.

For the case of silicon heterojunctions using n-type c-Si wafers, light induced improvements of minority carrier lifetime has been linked to the microstructure property of a-Si:H, R^* . Very dense a-Si:H passivated samples exhibit almost no light induced improvement while samples with a greater void density can either exhibit only light-induced improvement or a combination of light induced degradation followed by improvement depending on the void density. This effect is explained by a build up of positive charge at the interface at the voids that then push holes back to the high lifetime bulk c-Si.

In the case of silicon heterojunctions using p-type c-Si wafers, light induced improvement of minority carrier lifetime is linked to the cleaning procedure. Us-

ing lower HF dip times cause the sample to improve lifetime due to light flashes while greater HF dip times lead to a degradation of the lifetime. One possible explanation for this is that oxide may be left over could be charging negatively from the electrons thus increasing the lifetime of electrons in the bulk.

8.1.3 How does adding doped layers affect these light induced effects?

While Chapter 4 focussed on light induced effects on samples of wafers passivated with intrinsic a-Si:H, Chapter 5 expanded these experiments using doped a-Si:H layers. In this chapter, n-type c-Si wafers were used. It was found that doped a-Si:H, indeed, has a significant effect on light induced minority lifetime kinetics. Samples with an n-layer (back surface field) exhibited light induced degradation of minority carrier lifetimes while samples with a p-layer (emitter) exhibited light induced improvement of minority carrier lifetime. Both of these effects were explained by examining where charge can build up upon illumination. In the back surface field sample, negative charge can build up at the a-Si:H/c-Si interface which would reduce the hole lifetime while in the emitter

When precursors were used with both p-type and n-type a-Si:H layers on either side of the wafer, results showed that the flashing side determined the light soaking kinetics of the lifetime. The fact that the kinetics of the lifetime changes due to light soaking depend on the flashing side suggest that charging effects only occur when a-Si:H is has sufficient generation.

8.2 Can FTPS be used to better understand the a-Si:H/c-Si interface?

Chapter 6 explored the use of advanced Fourier transform photocurrent spectroscopy - external quantum efficiency (FTPS-EQE) techniques to study interface defects. Though initial results seemed promising, a thorough analysis of the principles of the technique as well as a refining of the measurement procedure showed that signals were not of use in studying interface defects. Though this study did not provide further insight into the physics of SHJ solar cells, it determined limitations of the FTPS-EQE. The analysis done here showed that FTPS-EQE is only appropriate when investigating bulk defects in the absorber layer and when the charge carrier lifetime is sufficiently low. This is because FTPS-EQE measures the contribution of transitions from defect energy levels to the conduction band to the photocurrent of a solar cell. In the case of thin film a-Si:H solar cells, there is a significant bulk defect density in the absorber layer of the solar cell. These bulk defects contribute a measurable amount of photocurrent and can thusly be measured by FTPS-EQE. [40] However, in the case of SHJ solar cells, the bulk absorber layer is made up of high quality c-Si and though interface

defects are significant electrically, there are not enough of them volumetrically to contribute to the photocurrent of the solar cell.

However, using FTPS-EQE for studying polycrystalline silicon solar cells deposited on glass showed some promising results. Here EPR results showing defect densities were linked to defect positions close to the bands by FTPS-EQE. This implies that shallow traps play a significant role in poly-Si solar cells on glass.

8.3 How can novel applications of SHJ solar cells be best used to aid in water splitting applications?

Chapter 7 discussed the use of SHJ solar cells for water splitting applications. In this chapter, the use of SHJ in a tandem structure with a thin film nanocrystalline silicon solar cell was shown to provide good electronic properties for a supporting PV structure for silicon carbide based photocathodes. The hybrid, SHJ/nc-Si, solar cell has an efficiency of 10.4% under an AM 1.5 spectrum. Tunneling recombination engineering was identified as a key area of importance for making a high performing solar cell. Finally, an integration simulation was run to predict how the hybrid solar cell would function in conjunction with an a-SiC:H photocathode. This simulation predicted a current of 6.43 mA cm^{-2} corresponding to a solar to hydrogen efficiency of 7.90%.

8.4 Recommendations for Further Exploration

To better answer the research questions put forward, the following recommendations are put forward to continue research to better understand some of the findings presented in this thesis.

1. *Utilize minority carrier lifetime model for degradation.* Of notable exception to the studies done in Chapter 4 and 5 are the use of a similar model as given in Chapter 3. This model would extract data like defect and charge density from the full carrier injection dependent lifetime measurements. These results could be used to gather further information on the role of charge at the interface during light induced kinetics. However, these experiments were carried out prior to my knowledge of this model. Fitting was attempted, however, the model was unable to fit the measurements appropriately. The reason for this failure to fit was that the measurements did not use WTC-120's averaging measurement used to average the results of many measurements at once. As such there was a lot of noise in the lower injection levels and though much data processing was attempted, reporting on these results seemed dishonest. Therefore these experiments should be repeated using

averaged measurements that are suitable for good fitting. This may give better insight to the light induced improvements observed in this work.

2. *Perform more annealing experiments in-situ to test kinetic rates from literature.* Chapter 3 showed how to use a temperature dependent model of minority carrier lifetimes and included some results on initial annealing experiments on silicon heterojunction structures but this should be carried out in further detail. Utilizing a range of sample preparation conditions and longer annealing times, this model could be used to gather more detailed and accurate annealing kinetics data. As the experiments can now be done in-situ and through automation, an exploration study on this could lead to some very interesting findings that may confirm or reject current theories on what is the driving force of these annealing kinetics.
3. *Perform light soaking and annealing studies with ITO.* In Chapter 5, doped silicon layers were added to the sample stacks. This helped to get closer to the fully realized SHJ solar cell. However, full SHJ solar cells also have transparent conducting oxides (usually, ITO). These oxides are also known to affect the lifetime of the sample when deposited through sputtering, but seem to not affect the lifetime when deposited through atomic layer deposition (ALD). [136, 137]
4. *Further exploration of p-type wafer experiments.* In Chapter 4 light induced improvements in minority carrier lifetime were shown in silicon heterojunction structures using p-type wafers. This could be further examined by a more detailed study on p-type wafers. In the course of this work, passivation of p-type wafers was less consistent and lifetimes were consistently lower than with n-type wafers, however, a more detailed study into the annealing and light soaking kinetics of p-type wafers passivated with a-Si:H may help to better understand the underlying mechanisms if passivation quality can be applied more consistently.
5. *Expand a-Si:H deposition parameters.* The majority of the work done in this thesis used two deposition regimes of a-Si:H when fabrication silicon heterojunction structures. These were referred to as the undiluted and diluted cases. However, there are always more parameters that can be modified. Chapter 4 showed that varying the deposition temperature with an undiluted recipe changed both the microstructure and the light soaking lifetime kinetics. This links the two properties together, however there may be other ways to vary the microstructure and it would be very interesting to use other changes in deposition conditions to either confirm or expand the parameters of this explanation.
6. *Realize full monolithic device with SiC and SHJ/nc-Si.* In Chapter 7, a monolithic hybrid device is proposed. However, this full device was not yet realized due to unknown problems with creating wafer based photocathodes.

This work can be expanded by diving further into this study to determine the issues at hand and fully realize this device. Furthermore, this should be compared to utilizing SHJ solar cells in series directly powering an efficient electrolyzer to gauge whether the solar to hydrogen potential is more effective than this simpler solution.

Bibliography

- [1] J. Jean, P. R. Brown, R. L. Jaffe, T. Buonassisi, and V. Bulović, *Energy & Environmental Science* **8**, 1200 (2015).
- [2] IEA, *Key World Energy Statistics 2014*, Tech. Rep. (2014).
- [3] IEA, *Technology Roadmap: Solar Photovoltaic Energy*, Tech. Rep. (2014).
- [4] IEA, *2015: Snapshot of global photovoltaic markets*, Tech. Rep. (2016).
- [5] *Photovoltaics Report*, Tech. Rep. November (Fraunhofer Institute for Solar Energy Systems, 2015).
- [6] W. Shockley and H. J. Queisser, *Journal of Applied Physics* **32**, 510 (1961).
- [7] R. Street, *Hydrogenated amorphous silicon* (Cambridge University Press, Cambridge).
- [8] S. M. Hu and W. J. Patrick, *Journal of Applied Physics* **46**, 1869 (1975).
- [9] K. R. McIntosh, M. J. Cudzinovic, D. D. Smith, W. P. Mulligan, and R. M. Swanson, in *3rd World Conference on Photovoltaic Energy Conversion* (2003) pp. 971–974.
- [10] Panasonic, “Panasonic HIT Solar Cell Achieves World’s Highest Conversion Efficiency of 24.7% at Research Level,” (2013).
- [11] A. Goodrich, P. Hacke, Q. Wang, B. Sopori, R. Margolis, T. L. James, and M. Woodhouse, *Solar Energy Materials and Solar Cells* **114**, 110 (2013).
- [12] A. Hauser, A. Richter, S. Leu, M. Burger, and G. Thun, *Cell and module design from the LCOE perspective*, Tech. Rep. (Meyer Burger, 2014).
- [13] K. Okuda, H. Okamoto, and Y. Hamakawa, *Japanese Journal of Applied Physics* **22**, L605 (1983).
- [14] M. Tanaka and M. Taguchi, *Japanese Journal of Applied Physics* **31**, 3518 (1992).
- [15] D. Schroder, *Semiconductor Material and Device Characterization*, 3rd ed. (John Wiley & Sons, Inc., Tempe, AZ, 2006).

- [16] G. Watkins, *Chinese Journal of Physics* **15**, 92 (1977).
- [17] G. D. Watkins, *Materials Science in Semiconductor Processing* **3**, 227 (2000).
- [18] A. G. Aberle, *Progress in Photovoltaics: Research and Applications* **8**, 473 (2000).
- [19] S. De Wolf, A. Descoeurdes, Z. C. Holman, and C. Ballif, *Green* **2**, 7 (2012).
- [20] H. Angermann, J. Rappich, L. Korte, I. Sieber, E. Conrad, M. Schmidt, K. Hübener, J. Polte, and J. Hauschild, *Applied Surface Science* **254**, 3615 (2008).
- [21] Z. Chen, P. Sana, J. Salami, and A. Rohatgi, *IEEE Transactions on Electron Devices* **40**, 1161 (1993).
- [22] R. Hezel, *Journal of The Electrochemical Society* **136**, 518 (1989).
- [23] W. Fuhs, K. Niemann, and J. Stuke, *AIP Conference Proceedings* **20**, 345 (1974).
- [24] J. I. Pankove and M. L. Tarng, *Applied Physics Letters* **34**, 156 (1979).
- [25] J. Mitchell, *Journal of Applied Physics* **114**, 193702 (2013).
- [26] S. Olibet, E. Vallat-Sauvain, L. Fesquet, C. Monachon, A. Hessler-Wyser, J. Damon-Lacoste, S. De Wolf, and C. Ballif, *Physica Status Solidi (a)* **207**, 651 (2010).
- [27] H. Dersch, *Applied Physics Letters* **38**, 456 (1981).
- [28] M. Stutzmann, *Philosophical Magazine Part B* **60**, 531 (1989).
- [29] A. H. M. Smets, W. M. M. Kessels, and M. C. M. van de Sanden, *Applied Physics Letters* **82**, 1547 (2003).
- [30] A. H. M. Smets and M. van de Sanden, *Physical Review B* **76**, 073202 (2007).
- [31] J. Schmidt and K. Bothe, *Physical Review B* **69**, 024107 (2004).
- [32] D. L. Staebler and C. R. Wronski, *Applied Physics Letters* **31**, 292 (1977).
- [33] J. Melskens, M. Schouten, A. Mannheim, A. S. Vullers, Y. Mohammadian, S. W. H. Eijt, H. Schut, T. Matsui, M. Zeman, and A. H. M. Smets, *IEEE Journal of Photovoltaics* **4**, 1331 (2014).
- [34] H. Kakinuma, S. Nishikawa, and T. Watanabe, *Journal of Non-Crystalline Solids* **59-60**, 421 (1983).
- [35] M. Fischer, H. Tan, J. Melskens, R. Vasudevan, M. Zeman, and A. H. M. Smets, *Applied Physics Letters* **106**, 043905 (2015).

- [36] T. Matsui, H. Sai, K. Saito, and M. Kondo, *Progress in Photovoltaics: Research and Applications* **21**, 1363 (2013), arXiv:1303.4604 .
- [37] A. Shah, P. Torres, R. Tscharnner, N. Wyrsh, and H. Keppner, *Energy* **285**, 692 (2000).
- [38] M. H. Brodsky and R. S. Title, *Physical Review Letters* **23**, 581 (1969).
- [39] J. Holovský, *In Tech Open*, edited by G. Nikolic (2011) pp. 257–282.
- [40] J. Melskens, M. Schouten, R. Santbergen, M. Fischer, R. Vasudevan, D. J. van der Vlies, R. J. V. Quax, S. G. M. Heirman, K. Jäger, V. Demontis, M. Zeman, and A. H. M. Smets, *Solar Energy Materials and Solar Cells* **129**, 70 (2014).
- [41] S. Bowden, U. Das, S. Herasimenka, and R. Birkmire, *Conference Record of the IEEE Photovoltaic Specialists Conference* , 2 (2008).
- [42] S. De Wolf, S. Olibet, and C. Ballif, *Applied Physics Letters* **93**, 032101 (2008).
- [43] S. De Wolf, B. Demareux, A. Descoedres, and C. Ballif, *Physical Review B* **83**, 233301 (2011).
- [44] S. Olibet, E. Vallat-Sauvain, and C. Ballif, *Physical Review B* **76**, 035326 (2007).
- [45] E. Mahdi, E. Mhamdi, J. Holovsky, C. Ballif, and S. D. Wolf, *Applied Physics Letters* **104**, 252108 (2014).
- [46] S. De Wolf, C. Ballif, and M. Kondo, *Physical Review B* **85**, 113302 (2012).
- [47] D. Deligiannis, R. Vasudevan, A. H. M. Smets, R. A. C. M. M. V. Swaaij, and M. Zeman, *AIP Advances* **5**, 097165 (2015).
- [48] P. Mahtani, R. Varache, B. Jovet, C. Longeaud, J.-P. Kleider, and N. P. Kherani, *Journal of Applied Physics* **114**, 124503 (2013).
- [49] J. R. Bolton, S. J. Strickler, and J. S. Connolly, *Nature* **316**, 495 (1985).
- [50] M. F. Weber, *Journal of The Electrochemical Society* **131**, 1258 (1984).
- [51] L. Han, I. A. Digdaya, T. W. Buijs, F. Abdi, Z. Huang, R. Liu, B. Dam, M. Zeman, W. A. Smith, and A. H. M. Smets, *Journal of Materials Chemistry A* **3**, 4155 (2015).
- [52] D. B. Fenner, D. K. Biegelsen, and R. D. Bringans, *Journal of Applied Physics* **66**, 419 (1989).

- [53] G. Trucks, K. Raghavachari, G. Higashi, and Y. Chabal, *Physical Review Letters* **65**, 504 (1990).
- [54] H. Angermann, W. Henrion, M. Rebien, and a. Röseler, *Solar Energy Materials and Solar Cells* **83**, 331 (2004).
- [55] D. Zhang, *Surface passivation and optical design of silicon heterojunction solar cells*, Ph.D. thesis (2015).
- [56] D. Deligiannis, S. Alivizatos, A. Ingenito, D. Zhang, M. van Seville, R. A. C. M. M. V. Swaaij, and M. Zeman, *Energy Procedia* **55**, 197 (2014).
- [57] W. Kern, *Journal of The Electrochemical Society* **137**, 1887 (1990).
- [58] K. Reinhardt and W. Kern, *Handbook of Silicon Wafer Cleaning Technology*, 2nd ed. (William Andrew Inc., Norwich, NY., 2008).
- [59] U. Kroll, A. Shah, H. Keppner, J. Meier, P. Torres, and D. Fischer, *Solar Energy Materials and Solar Cells* **48**, 343 (1997).
- [60] S. Rein, *Lifetime Spectroscopy: A Method of Defect Characterization in Silicon for Photovoltaic Applications*, edited by R. Hull, J. Parisi, R. M. Osgood, and H. Warlimont (Verlag Berlin Heidelberg, 2006).
- [61] E. Weisstein, "Fourier Transform Spectrometer," (1996).
- [62] M. Vanecek and A. Poruba, *Applied Physics Letters* **80**, 719 (2002).
- [63] J. Melskens, G. van Elzakker, Y. Li, and M. Zeman, *Thin Solid Films* **516**, 6877 (2008).
- [64] *A Thermo Electron Bussines*, Tech. Rep. (Thermo Nicolet Insitution, 2001).
- [65] R. Santbergen, A. H. M. Smets, and M. Zeman, *Optics Express* **21**, A262 (2013).
- [66] R. A. Sinton, in *25th PVSC* (1996) pp. 457–460.
- [67] S. Olibet, E. Vallat-Sauvain, and C. Ballif, *Physical Review B* **76**, 035326 (2007).
- [68] A. Richter, S. W. Glunz, F. Werner, J. Schmidt, and A. Cuevas, *Physical Review B* **86**, 165202 (2012).
- [69] J. P. Seif, G. Krishnamani, C. Ballif, and S. D. Wolf, *IEEE Journal of Photovoltaics* **5**, 718 (2015).
- [70] P. P. Altermatt, F. Geelhaar, T. Trupke, X. Dai, A. Neisser, and E. Daub, *NUSOD '05 - Proceedings of the 5th International Conference on Numerical Simulation of Optoelectronic Devices* **2005**, 47 (2005).

- [71] T. Trupke, M. A. Green, P. Würfel, P. P. Altermatt, A. Wang, J. Zhao, and R. Corkish, *Journal of Applied Physics* **94**, 4930 (2003).
- [72] R. F. Pierret, *New York* (1996) p. 792.
- [73] Y. Varshni, *Physica* **34**, 149 (1967).
- [74] D. Wolpert and P. Ampadu, *Managing Temperature Effects in Nanoscale Adaptive Systems* (2012) pp. 15–34.
- [75] P. P. Altermatt, F. Geelhaar, T. Trupke, X. Dai, A. Neisser, and E. Daub, *Applied Physics Letters* **88**, 92 (2006).
- [76] D. Zhang, I. Digdaya, R. Santbergen, R. van Swaaij, P. Bronsveld, M. Zeman, J. van Roosmalen, and a.W. Weeber, *Solar Energy Materials and Solar Cells* **117**, 132 (2013).
- [77] D. Deligiannis, V. Marioleas, R. Vasudevan, C. C. G. Visser, R. A. C. M. M. van Swaaij, and M. Zeman, *Journal of Applied Physics* **119**, 235307 (2016).
- [78] Y. Song, M. Park, E. Guliants, and W. Anderson, *Solar Energy Materials and Solar Cells* **64**, 225 (2000).
- [79] T. F. Schulze, L. Korte, E. Conrad, M. Schmidt, and B. Rech, *Journal of Applied Physics* **107**, 023711 (2010).
- [80] B. Hoex, J. J. H. Gielis, M. C. M. van de Sanden, and W. M. M. Kessels, *Journal of Applied Physics* **104**, 113703 (2008).
- [81] J. Melskens, A. H. M. Smets, M. Schouten, S. W. H. Eijt, H. Schut, and M. Zeman, *IEEE Journal of Photovoltaics* **3**, 65 (2013).
- [82] M. Fehr, A. Schnegg, B. Rech, O. Astakhov, F. Finger, R. Bittl, C. Teutloff, and K. Lips, *Physical Review Letters* **112**, 066403 (2014).
- [83] A. B. Sproul, *Journal of Applied Physics* **76**, 2851 (1994).
- [84] S. De Wolf and M. Kondo, *Journal of Applied Physics* **105**, 103707 (2009).
- [85] A. H. M. Smets, M. Fischer, and M. Zeman, in *21st Photovoltaic Science and Engineering Conference* (2011) pp. 1–2.
- [86] B. Pieters, J. Krc, and M. Zeman, *Conference Record of the 2006 IEEE 4th World Conference on Photovoltaic Energy Conversion*, 1513 (2006).
- [87] J. Melskens, A. H. M. Smets, S. W. H. Eijt, H. Schut, E. Brück, and M. Zeman, *Journal of Non-Crystalline Solids* **358**, 2015 (2012).
- [88] S. Chakraborty and D. Drabold, *Physical Review B* **79**, 1 (2009).

- [89] M. Stutzmann, W. Jackson, and C. Tsai, *Physical Review B* **32** (1985).
- [90] R. S. Crandall, *Physical Review B* **43**, 4057 (1991).
- [91] J. Kocka, M. Vanecek, and A. Triska, in *Amorphous Silicon and Related Materials* (1989) pp. 297–327.
- [92] A. O. Kodolbas and Ö. Öktü, *Optical Materials* **20**, 147 (2002).
- [93] H. Tan, E. Psomadaki, O. Isabella, M. Fischer, P. Babal, R. Vasudevan, M. Zeman, and A. H. M. Smets, *Applied Physics Letters* **103**, 173905 (2013).
- [94] A. H. M. Smets, T. Matsui, and M. Kondo, *Journal of Applied Physics* **104**, 034508 (2008).
- [95] R. Bergmann, *Applied Physics A* **194**, 187 (1999).
- [96] R. Brendel, R. B. Bergmann, P. Lölgen, M. Wolf, and J. H. Werner, *Applied Physics Letters* **70**, 390 (1997).
- [97] M. Fehr, P. Simon, T. Sontheimer, C. Leendertz, B. Gorka, a. Schnegg, B. Rech, and K. Lips, *Applied Physics Letters* **101**, 123904 (2012).
- [98] T. Sontheimer, A. Schnegg, S. Steffens, F. Ruske, D. Amkreutz, K. Lips, and B. Rech, *physica status solidi (RRL) - Rapid Research Letters* **7**, 959 (2013).
- [99] C. Becker, D. Amkreutz, T. Sontheimer, V. Preidel, D. Lockau, J. Haschke, L. Jogschies, C. Klimm, J. Merkel, P. Plocica, S. Steffens, and B. Rech, *Solar Energy Materials and Solar Cells* **119**, 112 (2013).
- [100] J. Haschke, D. Amkreutz, L. Korte, F. Ruske, and B. Rech, *Solar Energy Materials and Solar Cells* **128**, 190 (2014).
- [101] D. Amkreutz, J. Haschke, S. Kuhnappfel, P. Sonntag, and B. Rech, *IEEE Journal of Photovoltaics* **4**, 1496 (2014).
- [102] N. H. Nickel, N. M. Johnson, and W. B. Jackson, *Applied Physics Letters* **62**, 3285 (1993).
- [103] N. M. Johnson, D. Biegelsen, and M. Moyer, *Applied Physics Letters* **40**, 882 (1982).
- [104] S. Steffens, C. Becker, D. Amkreutz, A. Klossek, M. Kittler, Y.-Y. Chen, A. Schnegg, M. Klingsporn, D. Abou-Ras, K. Lips, and B. Rech, *Applied Physics Letters* **105**, 022108 (2014).
- [105] K. Yamamoto, M. Yoshimi, Y. Tawada, Y. Okamoto, A. Nakajima, and S. Igari, *Applied Physics A: Materials Science & Processing* **69**, 179 (1999).

- [106] S. Gall, C. Becker, E. Conrad, P. Dogan, F. Fenske, B. Gorka, K. Lee, B. Rau, F. Ruske, and B. Rech, *Solar Energy Materials and Solar Cells* **93**, 1004 (2009).
- [107] J. Wong, J. L. Huang, B. Eggleston, M. A. Green, O. Kunz, R. Evans, M. Keevers, and R. J. Egan, *Journal of Applied Physics* **107**, 123705 (2010).
- [108] W. Seifert and D. Amkreutz, *Solid State Phenomena* **178-179**, 116 (2011).
- [109] J. Wong, J. Huang, S. Varlamov, M. A. Green, and M. Keevers, *Progress in Photovoltaics: Research Applications* **20**, 915 (2012).
- [110] D. Amkreutz, J. Müller, M. Schmidt, T. Hänel, and T. F. Schulze, *Progress in Photovoltaics: Research and Applications* **19**, 937 (2011).
- [111] W. Jackson and N. Amer, *Physical Review B* **25**, 5559 (1982).
- [112] N. Wyrsh, F. Finger, T. McMahon, and M. Vanecek, *Journal of non-crystalline Solids* **138**, 347 (1991).
- [113] F. Urbach, *Physical Review* **92**, 61 (1953).
- [114] R. Vasudevan, Z. Thanawala, L. Han, T. Buijs, H. Tan, D. Deligiannis, P. Perez-Rodriguez, I. A. Digdaya, W. A. Smith, M. Zeman, and A. H. Smets, *Solar Energy Materials and Solar Cells* **150**, 82 (2016).
- [115] O. Khaselev, *Science* **280**, 425 (1998).
- [116] S. Licht, *Journal of Physical Chemistry B* **105**, 6281 (2001).
- [117] J. Hu, F. Zhu, I. Matulionis, A. Kunrath, T. Deutsch, E. Miller, and A. Madan, 23rd European Photovoltaic Solar Energy Conference (2008).
- [118] F. Zhu, J. Hu, A. Kunrath, I. Matulionis, B. Marsen, B. Cole, E. Miller, and A. Madan, *Solar Hydrogen and Nanotechnology II* **6650**, 66500S (2007).
- [119] F. Zhu, J. Hu, I. Matulionis, T. Deutsch, N. Gaillard, A. Kunrath, E. Miller, and A. Madan, *Philosophical Magazine* **89**, 2723 (2009).
- [120] I. A. Digdaya, L. Han, T. Buijs, M. Zeman, B. Dam, A. H. M. Smets, and W. A. Smith, *Energy Environ. Sci.* **8**, 1585 (2015).
- [121] S. Hu, C. Xiang, S. Haussener, A. D. Berger, and N. S. Lewis, *Energy & Environmental Science* **6**, 2984 (2013).
- [122] A. Stavrides, A. Kunrath, J. Hu, R. Treglio, A. Feldman, B. Marsen, B. Cole, E. Miller, and A. Madan, *Spie* **6340**, 1 (2006).
- [123] L. Han, F. F. Abdi, P. Perez Rodriguez, B. Dam, R. van de Krol, M. Zeman, and A. H. M. Smets, *Physical Chemistry Chemical Physics* **16**, 4220 (2014).

- [124] F. F. Abdi, L. Han, A. H. M. Smets, M. Zeman, B. Dam, and R. van de Krol, *Nature communications* **4**, 2195 (2013).
- [125] M. A. Green, K. Emery, Y. Hishikawa, W. Warta, and E. D. Dunlop, *Progress in Photovoltaics: Research and Applications* **22**, 701 (2014).
- [126] A. Descoeudres, Z. C. Holman, L. Barraud, S. Morel, S. De Wolf, and C. Ballif, *IEEE Journal of Photovoltaics* **3**, 83 (2013).
- [127] R. van de Krol and M. Grätzel, *Photoelectrochemical Hydrogen Production* (2012) p. 59.
- [128] C. Zoski, *Handbook of Electrochemistry* (2007).
- [129] M. A. Green, *Solar Energy Materials and Solar Cells* **92**, 1305 (2008).
- [130] D. Murata, T. Yuguchi, and H. Fujiwara, *Thin Solid Films* **571**, 756 (2013).
- [131] C.-H. Cheng, J.-H. Chang, C.-I. Wu, and G.-R. Lin, *RSC Adv.* **5**, 36262 (2015).
- [132] C.-Y. Wei, C.-H. Lin, H.-T. Hsiao, P.-C. Yang, C.-M. Wang, and Y.-C. Pan, *Materials* **6**, 5440 (2013).
- [133] P. Babal, J. Blanker, R. Vasudevan, A. H. M. Smets, and M. Zeman, *Conference Record of the IEEE Photovoltaic Specialists Conference*, 321 (2012).
- [134] P. D. Veneri, L. V. Mercaldo, and I. Usatii, *Progress in Photovoltaics: Research and Applications* **20**, 148 (2012).
- [135] S. S. Hegedus, F. Kampas, and J. Xi, *Applied Physics Letters* **67**, 813 (1995).
- [136] B. Macco, D. Deligiannis, S. Smit, R. A. C. M. M. van Swaaij, M. Zeman, and W. M. M. Kessels, *Semiconductor Science and Technology* **29**, 122001 (2014).
- [137] B. Demareux, J. P. Seif, S. Smit, B. Macco, W. M. M. E. Kessels, J. Geissbühler, S. De Wolf, and C. Ballif, *IEEE Journal of Photovoltaics* **4**, 1387 (2014).

Acknowledgements

In all probability, the vast majority of the readers of this thesis have flipped to this page before reading a single page of science. I had better make sure that I write this section properly. If you like it maybe you will at least flip to the summary after scanning through to try and find your name in here, but I will not be horribly offended if you don't.

Almost five years have passed since I started my PhD research at the Photovoltaic Materials and Devices group in TU Delft. Though performing all of this work and completing a PhD is a great personal accomplishment, I could not have done this without the help of many others whom I will acknowledge now. My sincerest apologies if I have left you out.

I have to start with the two people who are most responsible for me getting this position. These are my two promotors Professor Miro Zeman and Professor Arno Smets. Miro, thank you for first giving me a chance as an MSc student to do my thesis work in this group and then to continue as a PhD student here. This group, under your leadership, is very collaborative and supportive and provides the necessary atmosphere for all of the work I was able to do in my time here. Arno, you have been a very supportive and positive supervisor. You have a way of casting all my self-doubts and issues aside and can see the best in the work that I was able to do. It was great to share both days of work, nights of social activity and travels around the world with you. I'm also very proud of your ability to play and win in three out of three Delft Ultimate Frisbee City Leagues even when you are on a different team than me.

I would also like to thank the rest of my committee, Dr. Stefaan De Wolf, Dr. Delfina Muñoz, Dr. Takuya Matsui, Professor Ruud Schropp and Professor Arthur Weeber, as well as my reserve member, Professor Peter Palensky. Thanks for giving me some valuable feedback to improve the quality of this thesis. Furthermore I want to thank you for coming out to Delft for my defense.

I also had the pleasure of working with Associate Professor, Dr. René van Swaaij. René, your assistance in matters of semiconductor physics was invaluable during my time here. Your critical nature always pushed me to make sure my work was always very sound before I could present it at PVMD group meetings. Additionally I was able to see the growth and maturation of Assistant Professor, Dr. Olindo Isabella. Olindo, you were still a PhD candidate when I started and now you have both your doctorate and are on your way to a very successful academic career. Thanks for all your help along the way and it was a pleasure to

work with you in developing the PV Systems course to get it to the level where it is today.

I have also had some great officemates throughout my time here in LB 03.380. Dr. Hairen Tan, your work ethic and determination was always an inspiration to me. You provided me with a lot of helpful guidance throughout these past years and I hope your career lasts much longer than the perovskite solar cells you currently work on in Toronto. Dimitris (Dimitrios? Dimi? I can never figure out which ending to use) Deligiannis, you have been a close colleague and friend in our collaborative work to increase performance and understanding of silicon heterojunctions in TU Delft. We shared a lot of good times and helped each other through a lot of frustration. I know for sure that the quality of much of my thesis was greatly improved through your helpful input and assistance. I know you are very close to finishing your own PhD and cannot wait to call you a fellow doctor in the coming months. Nasim Rezaei, you are relatively new to LB 03.380 but are a very welcome addition. You are extremely kind and curious and I thank you for always being there with some fruit or some nuts and getting our peer group to take some breaks and go outside when the weather demands it. I wish you the best in your PhD journey.

I would also like to thank my other PhD and post-doc colleagues in the group. Dr. Pavel Babal, you were my supervisor during my MSc thesis and without the proper guidance there I probably would not have been able to get the PhD position here. Dr. Rudi Santbergen, thank you for being a great colleague and especially for translating my summary and propositions into Dutch. Dr. Jimmy Melskens, thanks for being such a funny and hard-working guy. I enjoyed our collaborations but also our trip together in the US. We should get some more donuts some time. Dr. Klaus Jäger, you were always there to distract me from my work with some surprising thoughtful topic. You were a joy to work with as well and I wish you all the best. Dr. Dong Zhang, your initial work in heterojunctions at our group was fundamental to the success that I was able to achieve here. Dr. Andrea Ingenito, the group has not been the same without your jovial and jokey attitude and no one calls me “The American” anymore. Additionally I would like to thank Dr. Mirjam Theelen, Dr. Guangtao Yang, Dr. Lihao Han, Dr. Doyun Kim, Dr. Karol Jarolimek for being great colleagues as well.

In addition to all these current doctors, there are all the will-be doctors in our group as well. Marinus Fischer and Joke Westra thanks for being there as great colleagues and collaborators! To Martijn van Sebille, Fai Tong Si, Robin Vismara, Paula Perez-Rodriguez, Gianluca Limodio, Yuan Gao and Johan Blanker, thanks for being City League Frisbee teammates, spikeball and coffee break-mates (even if I don’t drink coffee) and most importantly, Game of Thrones post-episode analysts (sorry Paula).

Any experienced researcher knows that lab work cannot be done without the help of skilled and capable technicians. PVMD is extremely blessed in this regard. Martijn Tijssen, Stefaan Heirman, Remko Koorneef, Jan Chris Staalenburg and Kasper Zwetsloot were all instrumental in keeping all of the equipment func-

tioning. Additionally you are all great people and I shared many great conversations with you as we had lunch together or struggled to figure out how to ignite the plasma in AMOR. Additionally I would like to thank all of the technicians in the EKL that helped to keep the clean room in order.

A good research group is also no good without the help of a good secretarial staff. Lucky for the PVMD, we have a fantastic one. Thanks to Diana, Sharmila, Ilona and Ellen for always being there whenever practical issues needed to be solved.

I could not have done this work without my MSc project students, Dorine van der Vlies, Zaid Thanawala and Isabella Poli. I was extremely lucky to get three hard-working and intelligent students and you were all an absolute pleasure to work with. This work is really all of yours and all of your effort that went into doing a lot of the depositions, measurements and analysis in this thesis cannot be appreciated enough. Additionally my System Integration Project students Marc Schouten and Thierry de Vrijer helped me to work through some smaller problems throughout my PhD and I thank you as well.

Furthermore, in terms of scientific contribution, I would like to thank Tobias Sontheimer and Bernd Rech from the Helmholtz Centrum in Berlin for giving the polysilicon solar cell samples used in Chapter 6. Your samples were very useful for this analysis and contributed to the conference contribution at EUPVSEC.

Thanks to all my ultimate teammates and friends throughout my career here. Everyone who has played with Force Elektro, PUF, Dutch Mixed, UFO, Cambo Cakes and the Undutchables have helped to keep me sane throughout my time as a PhD. Thanks to all of you for countless battles on the field and parties off the field. I especially want to thank my teammate and friend, Lutz Müräu. Whether we were playing together, training together or spending countless nights organizing Rising High together, it has always been a blast to be your teammate and close friend throughout my time here in Delft.

Speaking of close friends, I cannot write my acknowledgements without Damien Rigden. You're my best friend even though we don't get to see each other as much as we'd like. You offer great support just by being you and being awesome.

I don't have the space to write about each and every other friend that helped to support me in my time here. Whether you were a housemate at the old library, a fellow diner at Wednesdays in Wolbodo or just someone that shared a meal or a drink with me, you were an important part of my success in writing this thesis.

I'll move now from friends to family. To Frank, Carla, Margaux and Floris, thanks for being so kind to me these past 4 years and letting me enjoy so many good times with your family. You have all been a great support structure for me while my family has been an ocean away.

I must also acknowledge my own family. Dad, you pushed me to excel as a kid and it is now all paying off with this degree. Your support through the last 30 years has been of great importance and I am very thankful for all of your help even when things have been tough for you. Mom, you have always kept me grounded and never let me forget how awesome life can be. You also always

reminded me and encouraged me to enjoy life and never take it too seriously. Your compassion and willingness to help others is always a great inspiration and I only hope I can manage to make the world a better place a fraction as much as you have and continue to do. Kumar, my dear brother, you may have gotten the title of "Doctor" before I did but I did catch up eventually, even if you think I'm just a fake doctor. You are a great brother and a great person, I wish you all the best and thank you for all the support you have given me throughout this time. To my extended family in Colombia and India thanks for being such an amazing global network of support and love for me throughout my life, especially to my aunt Claudia who made the trip over from Colombia for my defense.

Finally Ingeborg, my loving partner. We have been together throughout almost my entire PhD career and I surely could not have finished this thing without you. Thanks firstly for the great cover design for this book but the thanks extend way beyond that. You spent endless nights listening to me complain about deposition equipment, deal with impostor syndrome and help me out through all the tough struggles I had. Of course, we had plenty of good times in there as well. I love you a lot and owe a lot of my success to your love and support throughout these years.

It has been a very tough, but rewarding and overall very positive experience. Thanks to everyone I mentioned here, and everyone that I forgot and left out. I am definitely glad that I embarked on this challenge, am proud of myself that I finished it and I am excited to see what the future brings!

Summary

Silicon Heterojunction (SHJ) solar cells are currently the most efficient silicon based solar cells in the world. The SHJ structure is based on high quality crystalline silicon (c-Si) which is passivated with intrinsic amorphous silicon (a-Si:H). The emitter and back surface field of the solar cell are made of doped a-Si:H layers. This thesis explores the interface between a-Si:H and c-Si using minority carrier lifetime measurements. Specifically this thesis studies the light and annealing induced effects on the passivation quality of a-Si:H. Furthermore, this thesis explores how SHJ solar cells can be used for water splitting applications in order to better solve the energy storage problem inherent in solar energy. To these ends, the following research questions are asked:

1. What is the nature of the metastable properties of a-Si:H passivation of c-Si?
 - a) How is the a-Si:H/c-Si interface affected by annealing?
 - b) How is the a-Si:H/c-Si interface affected by light soaking?
 - c) How does adding doped layers affect these metastable properties?
2. Can Fourier Transform of Photocurrent Spectroscopy (FPTS) be used to better understand the a-Si:H/c-Si interface?
3. How can novel applications using SHJ solar cells be used to aid in water-splitting applications?

This thesis is structured in eight distinct chapters. Chapter 1 serves as an introduction to the thesis and gives the background concepts necessary to understand the work. This is followed by Chapter 2 which gives the methodology used in the different experiments presented throughout the thesis. These two chapters are then followed by the bulk work of the thesis.

Chapter 3 explains how to apply current models of injection dependent minority carrier lifetimes to properly execute in-situ annealing experiments on the a-Si:H/c-Si interface. Here it is shown how the temperature dependent parameters of silicon must be taken into account in order to accurately extract the defect and charge density from minority carrier lifetime measurements at elevated annealing temperatures. This finding can be used to more accurately determine annealing kinetics of these parameters.

Chapter 4 then examines the light induced effects on the a-Si:H/c-Si interface. This chapter shows that, in some cases, light soaking initially reduces the minority carrier lifetime of silicon heterostructures. However, after long exposures, the lifetime can recover or even increase past the initial as deposited lifetime. This increase in lifetime is linked to interface charging and, in the case of n-type wafers, the microstructure of the passivation a-Si:H plays a large role in the light-induced kinetics of the minority carrier lifetime of silicon heterostructures. Structures where the passivation layer has a higher void density tend to have a greater increase in lifetime while structures passivated with a more dense material tend to be dominated by light induced degradation. Furthermore, in the case of p-type wafers, the cleaning procedure also plays a large role in these kinetics and can reverse the kinetics from pure light induced degradation to pure light induced improvement of minority carrier lifetime from the as deposited state.

In Chapter 5, doped a-Si:H layers are added to the a-Si:H/c-Si samples to examine their effects on the light induced kinetics of the passivation quality. Two important findings are made in this chapter. Firstly, doped layers do, in fact, affect the light-induced kinetics of the minority carrier lifetime. Secondly, the side being light soaked has a dominating effect on the light soaking kinetics.

Chapter 6 then examines the feasibility of using FTPS to study defects in SHJ solar cells. This chapter also includes some work done on poly-Si solar cells on glass as it was discovered that FTPS is not suitable for interface defect studies of SHJ structures. Furthermore, this chapter shows the limitations of using FTPS to study solar cell defects and determines some artifacts that must be carefully considered to appropriately use this method.

Chapter 7 is the final bulk chapter of the thesis. It deviates from the fundamental questions and moves to applications of a novel SHJ/thin-film silicon hybrid cell for water-splitting. It is shown here that this hybrid cell made of a nanocrystalline top cell and a SHJ bottom cell is an ideal support structure for an amorphous silicon carbide photocathode.

Finally, Chapter 8 outlines the main conclusions of this work. This chapter summarizes the insights found throughout the thesis that help to answer the research questions. Furthermore, the chapter gives some recommendations for further work on these topics to increase understanding of the nature of these light-induced and annealing effects on the a-Si:H/c-Si interface.

Samenvatting

Dutch translation by Dr. Rudi Santbergen

De silicium heterojunctie (SHJ) zonnecel is tegenwoordig het efficiëntste type silicium zonnecel ter wereld. De SHJ structuur is gebaseerd op kristallijn silicium (c-Si) van hoge kwaliteit, gepassiveerd met intrinsiek amorf silicium (a-Si:H). De 'emitter' en het 'back surface field' van deze zonnecel zijn gemaakt van lagen gedoteerd a-Si:H. Dit proefschrift bestudeert de a-Si:H/c-Si interface door middel van metingen aan de levensduur van minderheidsladingsdragers. Dit proefschrift bestudeert in het bijzonder de effecten van licht en verwarming op passiveringskwaliteit van de a-Si:H laag. Verder onderzoekt dit proefschrift hoe SHJ zonnecellen gebruikt kunnen worden voor het ontleden van water, met als doel het probleem van energieopslag, inherent aan het gebruik van zonne-energie, aan te pakken. Hiervoor zijn de volgende onderzoeksvragen geformuleerd:

1. Wat is de aard van de metastabiliteit die optreedt in het c-Si passiverende a-Si:H?
 - a) Hoe wordt de a-Si:H/c-Si interface beïnvloed door verwarming?
 - b) Hoe wordt de a-Si:H/c-Si interface beïnvloed door licht?
 - c) Hoe beïnvloedt de toevoeging van gedoteerde lagen deze metastabiele eigenschappen?
2. Kan de meettechniek 'Fourier transform photocurrent spectroscopy' (FTPS) gebruikt worden om de a Si:H/c-Si interface beter te begrijpen?
3. Kunnen nieuwe typen op SHJ gebaseerde zonnecellen gebruikt worden voor de ontleding van water?

Dit proefschrift bestaat uit acht hoofdstukken. Hoofdstuk 1 dient als inleiding tot het proefschrift en geeft de nodige achtergrondinformatie. In Hoofdstuk 2 worden de experimentele methodes uitgelegd die in dit proefschrift worden gebruikt.

Hoofdstuk 3 beschrijft hoe de huidige modellen voor de levensduur van minderheidsladingsdragers gebruikt moeten worden om de resultaten te interpreteren

van experimenten waarin de invloed van verwarming op het a-Si:H/c-Si interface wordt onderzocht. Om nauwkeurig de defect- en ladingsdichtheid uit levensduurmetingen bij verhoogde temperaturen te verkrijgen moet namelijk rekening gehouden worden met de temperatuur afhankelijkheid van de eigenschappen van silicium. Deze bevinding is belangrijk om de door verwarming veroorzaakte verandering van deze dichtheden nauwkeurig te bepalen.

Hoofdstuk 4 onderzoekt vervolgens de effecten van licht op het a-Si:H/c-Si interface. Dit hoofdstuk laat zien dat, in sommige gevallen, licht in eerste instantie de levensduur van minderheidsladingsdragers vermindert. Echter, na langere blootstelling kan de levensduur herstellen of zelfs groter worden dan de initiële levensduur na depositie. Deze toename in levensduur is gerelateerd aan het opladen van het interface. In het geval van n-type c-Si wafers speelt ook de microstructuur van het passiverende a-Si:H een belangrijke rol. Het gebruik van a-Si:H met meer 'voids' leidt tot een grotere toename in de levensduur terwijl structuren gepassiveerd met een dichter a-Si:H voornamelijk degradatie laten zien. In het geval van p-type c-Si wafers speelt ook de reinigingsprocedure een belangrijke rol. Het kan er namelijk voor zorgen dat in plaats van een door licht geïnduceerde degradatie juist een verbetering van de levensduur optreedt.

In Hoofdstuk 5 worden gedoteerde a-Si:H lagen toegevoegd aan de a-Si:H/c-Si samples om te onderzoeken of ze effect hebben op de hierboven beschreven door licht geïnduceerde veranderingen in de passiveringskwaliteit. Dit hoofdstuk beschrijft twee belangrijke ontdekkingen. Ten eerste, hebben gedoteerde lagen wel degelijk invloed op door licht geïnduceerde verandering in levensduur. Ten tweede, is het effect van de gedoteerde laag aan de belichte zijde dominant.

Hoofdstuk 6 onderzoekt vervolgens de geschiktheid van FTPS metingen voor het bestuderen van interfacedefecten in SHJ zonnecellen. Omdat FTPS niet geschikt is gebleken voor SHJ structuren bevat dit hoofdstuk ook de resultaten van poly-Si zonnecellen op glas. Verder laat dit hoofdstuk de beperkingen van FTPS metingen zien en identificeert het de artefacten waarmee rekening mee moet worden gehouden bij het gebruik van deze methode.

Hoofdstuk 7 wijkt af van de fundamentele vragen en gaat in op praktische toepassingen van nieuwe hybride zonnecellen waarin SHJ en dunne-film silicium zonnecellen gecombineerd worden voor de ontleding van water. Een hybride cel, waarin een SHJ cel gecombineerd wordt met een nanokristallijn silicium cel, blijkt een ideale basis te vormen voor een fotokathode van amorf siliciumcarbide.

Hoofdstuk 8 geeft ten slotte de conclusies van dit werk. De in dit proefschrift gevonden inzichten worden gebruikt om de onderzoeksvragen te beantwoorden. Verder geeft dit hoofdstuk aanbevelingen voor vervolgonderzoek dat kan leiden tot een nog beter begrip van de effecten van licht en verwarming op het a-Si:H/c-Si interface.

List of Publications

This Thesis

Published

- Chapter 7: **R. Vasudevan**, Z. Thanawala, L. Han, T. Buijs, H. Tan, D. Deligiannis, P. Perez-Rodriguez, I. A. Digdaya, W. A. Smith, M. Zeman, and A. H. M. Smets, "*A thin-film silicon/silicon hetero-junction hybrid solar cell for photoelectrochemical water-reduction applications*", Solar Energy Materials and Solar Cells 150, 82 (2016).

Submitted for Publication

- Chapter 3: Submitted for publication (2016) - **R. Vasudevan**, I. Poli, D. Deligiannis, M. Zeman, A. H. M. Smets "*Temperature effects on the silicon hetero-junction lifetime model based on the amphoteric nature of dangling bonds*".
- Chapter 4 and 5: Submitted to the IEEE: Journal of Photovoltaics as a contribution at 43rd IEEE PVSC - **R. Vasudevan**, I. Poli, D. Deligiannis, M. Zeman, A. H. M. Smets "*Light-Induced Changes to the a-Si:H/c-Si heterointerface*".

Other Publications

- P. Babal, J. Blanker, **R. Vasudevan**, A. H. M. Smets, and M. Zeman, "*Microstructure analysis of n-doped $\mu\text{c-SiOx:H}$ reflector layers and their implementation in stable a-Si:H pin junctions*", Conference Record of the IEEE Photovoltaic Specialists Conference, 321 (2012).
- H. Tan, E. Psomadaki, O. Isabella, M. Fischer, P. Babal, **R. Vasudevan**, M. Zeman, and A. H. M. Smets, "*Micro-textures for efficient light trapping and improved electrical performance in thin-film nanocrystalline silicon solar cells*", Applied Physics Letters 103, 173905 (2013).
- Z. Remes, **R. Vasudevan**, K. Jarolimek, A. H. M. Smets, and M. Zeman, "*The optical spectra of a-Si:H and a-SiC:H thin films measured by the absolute Photothermal Deflection Spectroscopy (PDS)*", Solid State Phenomena 213, 19 (2014).

- J. Melskens, M. Schouten, R. Santbergen, M. Fischer, **R. Vasudevan**, D. J. van der Vlies, R. J. V. Quax, S. G. M. Heirman, K. Jäger, V. Demontis, M. Zeman, and A. H. M. Smets, *"In situ manipulation of the sub gap states in hydrogenated amorphous silicon monitored by advanced application of Fourier transform photocurrent spectroscopy"*, Solar Energy Materials and Solar Cells 129, 70 (2014).
- M. Fischer, H. Tan, J. Melskens, **R. Vasudevan**, M. Zeman, and A. H. M. Smets, *"High pressure processing of hydrogenated amorphous silicon solar cells: Relation between nanostructure and high open-circuit voltage"*, Applied Physics Letters 106, 043905 (2015).
- M. van Seville, **R. Vasudevan**, R. J. Lancee, R. A. C. M. M. van Swaaij, and M. Zeman, *"Optical characterization and density of states determination of silicon nanocrystals embedded in amorphous silicon based matrix"*, Journal of Physics D: Applied Physics 48, 325302 (2015).
- D. Deligiannis, **R. Vasudevan**, A. H. M. Smets, R. A. C. M. M. van Swaaij, and M. Zeman, *"Surface passivation of c-Si for silicon heterojunction solar cells using high-pressure hydrogen diluted plasmas"*, AIP Advances 5, 097165 (2015).
- D. Deligiannis, V. Mariolas, **R. Vasudevan**, C. C. G. Visser, R. A. C. M. M. van Swaaij, M. Zeman, *"Understanding the thickness-dependent effective lifetime of crystalline silicon passivated with a thin layer of intrinsic hydrogenated amorphous silicon using a nanometer-accurate wet-etching method"*, Journal of Applied Physics 119 (23), 235307, (2016).

Conference/Workshop Contributions

- A. H. M. Smets, **R. Vasudevan**, P. Babal, J. Melskens, M. Fischer, M. Zeman, *"Progress in understanding of a-Si:H solar cells by a-Si:H nanostructure engineering"*, Oral at PVSEC, 2011, Fukuoka, Japan.
- **R. Vasudevan**, M. Schouten, A. H. M. Smets, M. Zeman, *"The study of silicon heterojunction interface defects using multiple exposure quasi-steady state minority carrier lifetime measurements"*, Oral at MRS Spring Meeting, 2013, San Francisco, California.
- A. H. M. Smets, M. Fischer, **R. Vasudevan**, J. Melskens, M. Zeman, *"Revealing the origin of the Staebler-Wronski effect: progress in systematic and detailed experimental studies"*, Oral at MRS Spring Meeting, 2013, San Francisco, California.
- **R. Vasudevan**, M. Schouten, D. Zhang, M. Zeman, A. H. M. Smets *"Exploration of Metastability of a-Si:H/c-Si Surface Passivation"*, Poster at SiliconPV, 2014, Den Bosch, The Netherlands.

- M. van Seville, **R. Vasudevan**, R. J. Lancee, R. A. C. M. M. van Swaaij, M. Zeman, "*Optical characterization of embedded silicon quantum dots*", Poster at MRS Fall Meeting, 2014, Boston, MA.
- **R. Vasudevan**, D. van der Vlies, T. Sontheimer, J. Melskens, M. Fischer, M. Zeman, A. H. M. Smets, "*Feasibility study of Fourier transform photocurrent spectroscopy on various silicon based solar cells*", Poster at EUPVSEC, 2014, Amsterdam, The Netherlands.
- **R. Vasudevan**, Z. Thanawala, L. Han, H. Tan, M. Zeman, A. H. M. Smets, "*A thin film nc-Si:H/silicon wafer heterojunction tandem solar cell for silicon-based photoelectrochemical water splitting*", Poster at WCPEC, 2014, Kyoto, Japan.
- **R. Vasudevan**, Z. Thanawala, T. Buijs, D. Deligiannis, B. Dam, M. Zeman, I. Digdaya, L. Han, P. Perez-Rodriguez, W. Smith, A. H. M. Smets, "*Hybrid PEC-PV photocathode for water splitting based on silicon wafer heterojunctions and TF Si junctions*", Oral at MRS 2015 Spring Meeting, 2015, San Francisco, California.
- D. Deligiannis, **R. Vasudevan**, M. Fischer, A. H. M. Smets, R. A. C. M. M. van Swaaij, M. Zeman, "*On the surface passivation of c-Si using high pressure hydrogen diluted plasmas*", Oral at MRS 2015 Spring Meeting, 2015, San Francisco, California.
- P. Perez-Rodriguez, I. Digdaya, H. Tan, **R. Vasudevan**, W. Smith, M. Zeman, A. H. M. Smets, "*Thin-film silicon based devices for cost-effective solar water splitting*", Oral at e-MRS, 2015, Lille, France.
- **R. Vasudevan**, Z. Thanawala, T. Buijs, B. Dam, M. Zeman, I. Digdaya, L. Han, P. Perez-Rodriguez, W. Smith, A. H. M. Smets, "*Monolithic PEC-PV devices based on earth-abundant materials*", Oral at NWO workshop: "*Research Challenges in Harvesting and Converting Solar Energy*", 2015, Eindhoven, The Netherlands.
- P. Perez-Rodriguez, I. Digdaya, A. M. Raventos, M. Falkenberg, **R. Vasudevan**, M. Zeman, W. Smith, A. H. M. Smets, "*Towards 10% Solar-to-hydrogen Efficiencies Using Earth-abundant Materials*", Oral at EUPVSEC, 2015, Hamburg, Germany.
- M. Fischer, M. Schouten, S. Eijt, H. Schut, A. Schnegg, K. Lipps, A. Baldansuren, T. Nagai, T. Matsui, M. Zeman, **R. Vasudevan**, J. Melskens, A. H. M. Smets, "*Studying the nature of defects in various silicon materials used in photovoltaic applications*", Oral THz to Soft X-Ray Workshop at Helmholtz, 2015, Berlin, Germany.
- H. Tan, J. Blanker, P. Perez-Rodriguez, **R. Vasudevan**, B. Kniknie, Z. Vroon, A. Furlan, R. Janssen, M. Zeman, A. H. M. Smets, "*Hybrid multi-junction PV*"

devices based on thin-film a-Si:H, nc-Si:H, CIGS, organic PV and c-Si Heterojunctions", Oral at MRS Spring Meeting, 2016, Phoenix, Arizona.

- **R. Vasudevan**, I. Poli, D. Deligiannis, M. Zeman, A. H. M. Smets, "*Overview of the metastable properties of the a-Si:H/c-Si interface*", Oral at IEEE PVSC, 2016, Portland, Oregon.
- P. Perez-Rodriguez, I. Digdaya, A. M. Raventos, M. Falkenberg, **R. Vasudevan**, M. Zeman, W. Smith, A. H. M. Smets, "*Solar Fuel Production by Using PV/PEC Junctions Based on Earth-abundant Materials*", Oral at IEEE PVSC, 2016, Portland, Oregon.

Curriculum Vitae

Education

<i>PhD</i> Delft University of Technology	Delft, The Netherlands 2011-2016
<i>MSc - Sustainable Energy Technologies</i> Delft University of Technology	Delft, The Netherlands 2009-2011
<i>BSc - Electrical and Computer Engineering</i> Worcester Polytechnic Institute	Worcester, MA, USA 2004-2008

Work Experience

<i>Solar Energy Intern</i> Kamworks Solar	Sre Ampil, Cambodia 2010
<i>Junior Electrical Engineer</i> Granite Power Technologies	Manchester, NH 2009

Major Projects

<i>PhD Dissertation: Interface Defects and Advanced Engineering of Silicon Heterojunction Solar Cells</i> Delft University of Technology	2016
<i>MSc Thesis: Characterization of n-type Silicon Oxide for Use in Thin Film Solar Cells</i> Delft University of Technology	2011
<i>MSc Internship: Solar Battery Charging in Rural Cambodia</i> Kamworks Solar	2010

BSc Thesis: Class D Audio Amplifier
 Worcester Polytechnic Institute 2008

Computer Literacy at the Bangkok Refugee Center
 Bangkok Refugee Center 2007

Supervision

Isabella Poli - MSc Thesis 2015
Metastability Study of Silicon Heterojunction Solar Cells

Zaid Thanawala - MSc Thesis 2014
Water Splitting Applications Using a nc-Si:H/SHJ Tandem Device

Thierry de Vrijer - System Integration Project 2014
Defect Measurements in Photovoltaic Materials: A Comparison Study of FTPS and PDS

Dorine van der Vlies - MSc Thesis 2013
A Feasibility Study on the use of FTPS to Study Defects in Various Silicon Based Solar Cells

Marc Schouten - System Integration Project 2011
Testing the Kinetics of a-Si:H/c-Si(100) Interfaces Using Carrier Lifetime Measurements

Course Development and Teaching

Photovoltaic Systems - Developed and lectured 2014 & 2015

Photovoltaic Technologies - Lectured 2015

Photovoltaic Lab Course - Developed and supervised 2013 & 2014